Measurement of the Cross Section for the Elastic Photoproduction of the J/ψ Meson at HERA

Molly Anderson

1998

A thesis submitted to the University of Manchester for the degree of
Doctor of Philosophy in the Department of Physics and Astronomy
in the Faculty of Science.

Contents

Abstract

This thesis presents results on diffractive J/ψ photoproduction at the H1 experiment at HERA, using the decay channel $\mathrm{J}/\psi \longrightarrow \mu^+\mu^-$. The data sample was taken in 1995 and corresponds to an integrated luminosity of $4.9\,\mathrm{pb}^{-1}$. The γp cross section for elastic J/ψ production is found to increase steeply with centre-of-mass energy which is best described using perturbative QCD calculations developed by Ryskin. The γp cross section for proton-dissociative J/ψ production is also measured and shows a similar energy dependence to the elastic process. The t dependence of the cross sections is studied and is found to be exponential in accordance with a diffractive production mechanism. However, within the experimental errors on the slope parameters for each process, shrinkage is not observed. The decay angular distribution for the diffractive J/ψ sample is measured and found to be compatible with the assumption of s-channel helicity conservation made by both the soft and hard models of J/ψ production.

No portion of the work referred to in this thesis has been submitted in support of an application for another degree or qualification of this or any other university or other institute of learning.

Chapter 1

Introduction

The study of high-energy lepton-proton collisions provides information about the structure of the proton and the nature of the force which binds it together. Historically, deep-inelastic scattering experiments of this kind have played a crucial role in the development and the experimental justification of the Quark Parton Model and Quantum Chromodynamics, which describe hadrons and their strong interactions. At HERA collisions occur between positrons and protons with a centre-of-mass energy of approximately 300 GeV, a factor of 10 larger than previous fixed target experiments. This opens a previously inaccessible kinematic domain which allows the structure of the proton to be probed using deep-inelastic scattering down to distances of about 10^{-18} m, providing a more accurate test of Quantum Chromodynamics. There is another group of events at HERA called photoproduction where the incoming positron emits an almost real photon which interacts with the proton. This category of events dominates the ep cross section.

In photoproduction J/ψ mesons are produced elastically by diffractive processes which describe the γp interaction as taking place via the exchange of a colourless object. Similar processes have been observed in hadron-hadron collisions and are described using Regge theory. Applications of this model of soft-hadronic interactions to diffractive events at HERA have been successful in describing the energy dependence of the total cross section and the production of the light vector mesons providing the colourless exchange is dominated at high energies by the pomeron, an object with the quantum numbers of the vacuum. However, despite these successes the pomeron has not yet been described in terms of Quantum Chromodynamics.

The study of elastic J/ψ production at HERA promises to provide information about the nature of the pomeron. Soft models have been extended to describe the production of this heavier vector meson; however these at present seem unable to describe the energy dependence of its cross section. The large mass of the charm quark, however, provides a hard scale allowing alternative calculations of the elastic J/ψ cross section to be made using perturbative QCD. These calculations are strongly dependent on the gluon distribution of the proton. The elastic production of the J/ψ meson thus lies in a region where both soft and hard models have been developed, perhaps making it possible to dispense with the traditional delineation.

A general description of *ep* interactions at HERA is given in chapter 2 before the production mechanisms and theoretical models of the J/ψ meson are discussed in detail. A description of the H1 detector at HERA follows in Chapter 3. The selection of a sample of elastic J/ψ candidates is discussed in chapter 4 before the measurement of the cross section is presented in chapter 5. Chapter 6 goes on to interpret these results in the context of the available theoretical predictions.

Chapter 2

HERA Physics

2.1 Introduction

HERA stands in a long line of experiments which use leptons, which are themselves thought to be structure-less, to probe the substructure of protons and neutrons. Where HERA is innovative, however, is in its achievement of centre-of-mass energies an order of magnitude larger than its predecessors. This is possible because of the colliding nature of the experiment where high momentum beams of positrons and protons take part in head on collisions. It is the first case of an $e^{\pm}p$[1] collider; previously experiments were of the fixed target kind where high energy beams of leptons were incident on stationary nucleon targets.

Deep-inelastic scattering (DIS), where the positron penetrates inside the proton, makes it possible to study the constituent parts of the nucleon. At HERA's high energies structure can be probed to scales ten times smaller than previously possible, making a more accurate test of the theory of strong interactions, namely Quantum Chromodynamics (QCD), possible. To give context to the analysis described in this thesis, the models of proton structure which have come about with the help of DIS are briefly reviewed at the start of this chapter. Generally, this theory is dealt with in increasing complexity in [1], [2] and [3], while topics specific to HERA are discussed in [4]. The theory more directly relevant to this thesis, however, includes that of photoproduction and vector meson production. These areas are covered in more depth in the second part of the chapter.

---

[1] Since June 1994 HERA has used positron beams, however the use of 'positron' or the generic 'e' applies equally to electrons except where stated otherwise.

2.2 Deep-inelastic Scattering

The proton and neutron ceased to be unique with the discovery of the pion in 1947 and a number of other strongly interacting particles in the years thereafter. The patterns between these particles were eventually expressed in 1964 in terms of an SU(3) symmetry, which seemed to be justified when the Ω^-, which was predicted by the model, was discovered three years later. This mathematical classification hinted at the existence of a hadronic substructure which was first formalised, also in 1964, in the quark models of Gell-Mann [5] and Zweig. These hypothesised that three types or flavours of spin $\frac{1}{2}$ particles called the up (u), down (d) and strange (s) quarks were the building blocks of all the hadrons.

This model was not proposed by Gell-Mann and Zweig as a physical reality. However, DIS experiments in the late 1960s suggested that the lepton probes were indeed scattering off pointlike constituents (partons). These partons were later identified with the postulated quarks. Since then, lepton-nucleon experiments have played an essential part in understanding this substructure and in elucidating the nature of the strong force that binds it together.

The fourth quark flavour, called charm (c), was predicted by Glashow, Iliopoulos and Maiani, and its existence was confirmed with the discovery of the J/ψ [6] [7] and ψ' [8] mesons at SLAC and Brookhaven in 1974. Later, in 1977, the heavier quark flavour, bottom (b), was identified with the discovery of the Υ at FNAL [9] [10]. This discovery was wholly unexpected and in order to preserve symmetry a sixth flavour called top (t) was then predicted. The discovery of the top quark took many years; however, in 1995, experiments at the Tevatron collider finally confirmed its existence [11] [12].

2.2.1 Kinematics

At HERA 27.5 GeV positrons are used to probe protons with energies of 820 GeV. Where DIS occurs the process can be represented diagrammatically as shown in figure 2.1, where the particles are labelled with their defining four-momenta. As can be seen, the positron and proton interact via the exchange of an electroweak boson: in the case of the neutral current process (NC), $ep \longrightarrow eY$, the mediating particle is a photon or Z^0, while for the charged current process (CC), $ep \longrightarrow \bar{\nu}Y$, a W^+ is exchanged.

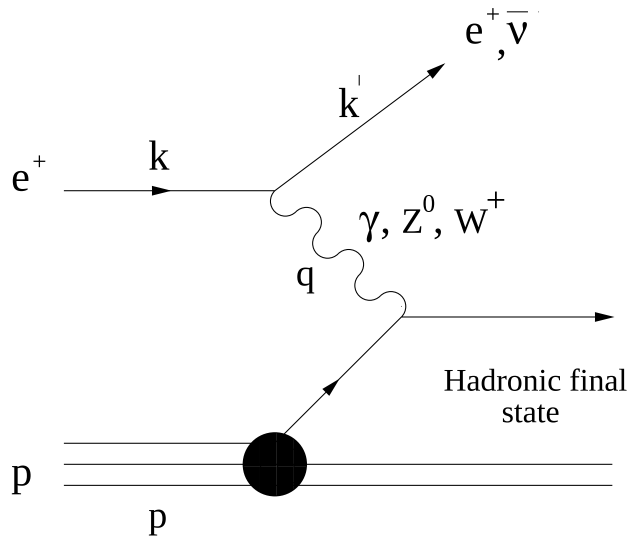

Figure 2.1: Diagram showing the DIS process for ep interactions. The four-momenta used to describe the kinematics of the process are defined.

Conventionally the kinematics of the DIS process are described by the two Lorentz invariant quantities:

$$Q^2 = -q^2 = -(k - k')^2 \tag{2.1}$$

$$x = \frac{Q^2}{2p \cdot q}. \tag{2.2}$$

The first variable, Q^2, represents the virtuality of the exchange boson and also determines the distance scale, $\lambda \sim 1/\sqrt{Q^2}$, to which the proton can be probed. The second quantity, x, often called the Bjorken scaling variable, can be interpreted in terms of the Quark Parton Model (QPM) which is discussed later. In this case x represents the fraction of the proton's momentum carried by the struck quark as measured in a frame where the proton's momentum is infinite. Another scaling variable, y, also proves useful in the study of ep interactions. This is defined as:

$$y = \frac{q \cdot p}{k \cdot p} \tag{2.3}$$

and can be interpreted as the fraction of the positron's energy which is transferred to the boson, measured in the proton rest frame. The quantities Q^2, x and y, as defined above, are all related via the simple equation:

$$Q^2 = xys, \tag{2.4}$$

where the positron and proton masses have been neglected. The extra variable s introduced here is defined as the square of the centre-of-mass energy of the ep system so that:

$$s = (k + p)^2. \tag{2.5}$$

At HERA the centre of mass energies achieved are around $\sqrt{s} = 300\,\mathrm{GeV}$. Finally, a variable important to this analysis is W, which represents the centre of mass energy of the boson-proton system. It can be related to the Q^2 and x variables already defined and is given by:

$$W^2 = (p + q)^2 \simeq Q^2 \left(\frac{1 - x}{x} \right). \tag{2.6}$$

Since these kinematic quantities are all interrelated, once two are known the others can be evaluated. The reconstruction of the kinematics of the event is possible in DIS events due to the identification and the measurement of the scattered positron. Providing the angle, θ and the energy, E', of the scattered positron are known then Q^2 and y are given by:

$$Q^2 = 4EE' \cos^2 \left(\frac{\theta}{2} \right) \tag{2.7}$$

$$y = 1 - \frac{E'}{E} \sin^2 \left(\frac{\theta}{2} \right), \tag{2.8}$$

where E is the beam energy of the incident positrons. The reconstruction of these quantities enable x and then W to be determined from equations 2.2 and 2.6.

The exchange of the electroweak boson, with a mass M, introduces a propagator term to the scattering amplitude of the form:

$$\frac{1}{Q^2 + M^2}. \tag{2.9}$$

This means that the mass-less photon is favoured as an exchange particle at low Q^2 and the heavier Z^0 and W^+ only contribute significantly when Q^2 is of the order of their masses. For the most part the Z^0 and W^+ only make small contributions to the total cross section when measured in the kinematic domain of HERA.

2.2.2 Proton Structure

The differential cross section for the NC DIS process can be expressed in terms of the structure functions, $F_1(x, Q^2)$, $F_2(x, Q^2)$ and $F_3(x, Q^2)$, so that:

$$\frac{d^2\sigma_{NC}}{dxdQ^2} = \frac{4\pi\alpha_{em}^2}{xQ^4}\left[xy^2F_1(x,Q^2) + (1-y)F_2(x,Q^2) + \left(y - \frac{y^2}{2}\right)xF_3(x,Q^2)\right] \tag{2.10}$$

The final term, involving $F_3(x, Q^2)$, remains negligible however, until Q^2 is of the order of the Z^0 mass. The remaining structure functions $F_1(x, Q^2)$ and $F_2(x, Q^2)$ are related by the Callan-Gross relation [13] as a consequence of the spin $\frac{1}{2}$ nature of the partons in the proton. This states that:

$$2xF_1 = F_2, \tag{2.11}$$

so that the determination of $F_2(x, Q^2)$ is the essential factor in the understanding and modelling of the proton's internal structure. Due to this, F_2 has been extensively measured and the results from some of these analyses are shown in figure 2.2 [14] as a function of x and Q^2. The features of these plots require explanations from the Quark Parton Model and QCD.

The Quark Parton Model [15] [16] assumes that the quarks inside the proton are pointlike. With this restriction it can be shown that, at fixed values of x, $F_2(x, Q^2)$ remains constant as a function of Q^2. This phenomenon, called scale invariance [17], was seen in the early DIS experiments, so that the point-like nature of the quarks

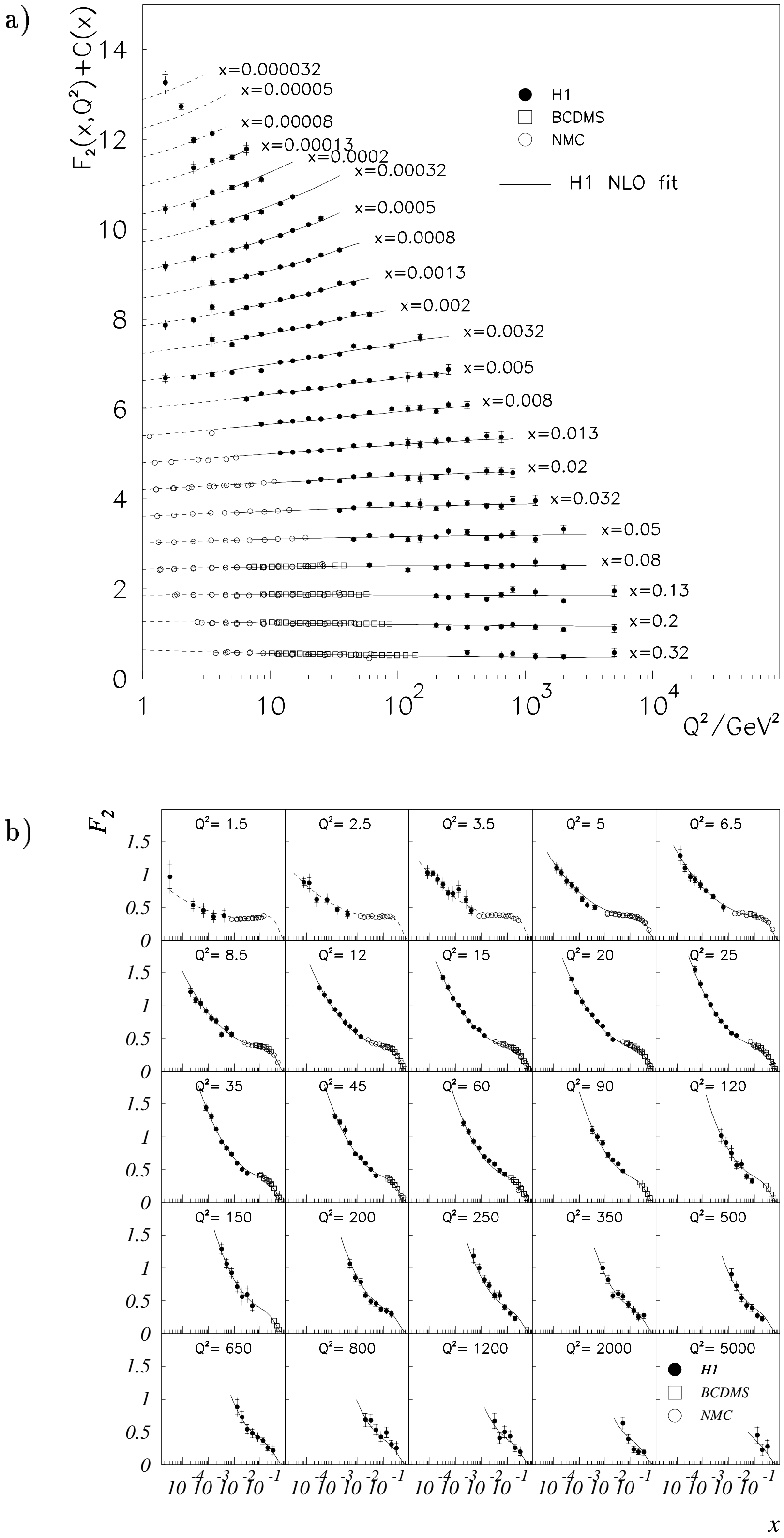

Figure 2.2: Plots showing the proton structure function, $F_2(x,Q^2)$, as a function of a) Q^2 and b) x. [14] The data is from H1 and the fixed target experiments: BCDMS and NMC. The fit shown is a NLO QCD fit.

was assumed to be true. There was also experimental evidence for the derived Callan-Gross relation, lending support to the idea that the quarks were spin $\frac{1}{2}$ particles. Therefore, the DIS process can be treated within the QPM as the elastic scattering of a highly virtual photon off a free point-like object inside the proton. However, free quarks are never observed in isolation due to a phenomenon called colour confinement. This means that after the photon-quark scattering a process called hadronisation occurs where the struck quark and the proton remnant form the bound quark units that make up the observed final state. The scattering and hadronisation are considered to be independent processes, so that DIS can be regarded in two stages.

The Quark Parton Model described above has several serious flaws that require a more detailed understanding of the proton's structure. Firstly, the measurement of $F_2(x, Q^2)$ over large regions of x, as shown in figure 2.2, demonstrates that the scale invariance is approximate and only holds in the region where $x \approx 0.1$. At lower values $F_2(x, Q^2)$ is seen to increase with Q^2 while at higher values it decreases. This behaviour is known as the scaling violation. Secondly, when the momentum distributions of the quarks in the proton are summed the total only accounts for approximately half of the proton's overall momentum. These factors can be accounted for in the QCD model which states that the strong force binding the quarks together inside the proton is carried by a neutral vector boson called the gluon. In this model the proton is made up of the three valence quarks which radiate gluons, which in turn can produce the quark-antiquark pairs which are called the 'sea' quarks.

Since the photon can couple to quarks and not gluons the quantity F_2 is a measurement of the number of quarks in the proton. However, within the QCD model the number of sea quarks is related to the gluon content of the proton so that the rise of F_2 at low x which is indicative of an increase of quarks in the proton is in fact driven by an increase in the number of gluons. The lower momentum sea quarks make increasingly significant contributions to $F_2(x, Q^2)$ at higher Q^2, when smaller distances are probed. As x tends towards low values, where the valence quarks carry less of the proton's momentum and the sea quarks are more prominent, $F_2(x, Q^2)$ is expected to rise. Conversely, when x is large and the momentum of the proton is held mostly by the valence quarks, $F_2(x, Q^2)$ is expected to fall. This is indeed seen in figure 2.2. In a more quantitative sense the equations of Dokshitzer, Gribov, Lipatov, Alterelli and Parisi (DGLAP) [18] [19] [20], which are based on the QCD model, describe the evolution of F_2 as a function of Q^2 very accurately over a very wide range of Q^2.

The coupling constant, α_s, of the strong force runs in the opposite direction to that of the electromagnetic force, α_{em}, due to the fact that the gluons, like quarks, carry the colour charge and can couple to themselves. The consequence of this is that at low Q^2 α_s is very large which means that the quarks are very strongly interacting. As Q^2 increases α_s falls off rapidly so that in the limit $Q^2 \rightarrow \infty$ the quarks are considered to be non-interacting or 'asymptotically free'. It is this that accounts for the success of the Quark Parton Model in this kinematic domain. When $\alpha_s \ll 1$ perturbation theory can be used to predict the cross section for a particular process. This is so when, for example, the Q^2 of the mediating boson is known to be sufficiently large or when the final state contains a lepton pair with a large invariant mass. These types of conditions are referred to as a 'hard scale' without which predictions can only be made using phenomenological methods. The behaviour of α_s also explains the fact that quarks are never seen in isolation since the energy required to separate the quark from the proton is far higher than the energy required to create a bound quark-antiquark state. This phenomenon is referred to as confinement and explains the colourless nature of any observed final state.

2.3 Photoproduction

As has been indicated, the dominant contribution to the NC *ep* cross section at HERA are events where the positron and proton interact via the exchange of a virtual photon. However, the term photoproduction is reserved for the category of events where this photon is almost real so that the positron is scattered through small angles and $Q^2 \sim 0$. The rate for this type of event gets increasingly large as $Q^2 \rightarrow 0$ due to the $1/\mathrm{Q}^4$ term in equation 2.10. The Q^2 boundary between DIS and photoproduction events is not a physical one, however, leaving it open for a multitude of definitions. At H1 photoproduction is usually referred to as an event whose scattered positron is not detected in the main body of the detector. In most cases this means that the scattered positron, which is required to have polar angles of greater than 179°, remains undetected, although a small number are detected in the electron tagger, which is situated close to the beam-pipe in the negative z direction. Applying this criterion to this analysis gives a sample of events with a range of $Q^2 < 1.2\,\mathrm{GeV}^2$.

The photoproduction process in an *ep* collision can be divided using the single photon approximation into two subprocesses: the radiation of the almost-real photon by the positron $\mathrm{e} \rightarrow \mathrm{e}\gamma$ and the physics process of the photon interacting with the proton $\gamma p \rightarrow \mathrm{Y}$. The former case can be regarded as an independent factor in the calculation of the γp cross section and is estimated using the Weizsäcker-Williams approximation (see section 5.8).

Experimentally, photoproduction events can be categorised into two classes in terms of the transverse momentum, p_t, of their final states. The smaller class is where there is a sufficiently large p_t in the final state to indicate a 'hard' subprocess, thereby justifying the use of perturbative QCD in calculations. The alternative is where the final state has a low p_t confining the event to the 'soft' category where perturbative QCD calculations can not be used. To model the behaviour of these events phenomenological models are used. Again, the boundary between these two classes is somewhat loose, however as a rough guide a $p_t > 1$ GeV should be expected for a hard interaction while a soft process would only have a few hundred MeV associated with it. HERA's kinematic range straddles both of these cases so that the study of the transition region between hard and soft processes is possible.

The hard process can be further categorised into 'direct' and 'resolved' processes, examples of which are represented by the diagrams in figure 2.3. In the direct process the photon acts as a point-like particle which couples directly to a quark in the proton and is effectively absorbed during the hard subprocess. An example of this type of process is boson-gluon-fusion (BGF), which is sensitive to the gluon distribution in the proton. BGF happens to be one of the mechanisms by which the J/ψ meson is produced and hence is discussed further in section 2.4.1. It is also possible for the photon to contribute only a fraction of its momentum to the hard photon-proton interaction. This is referred to as the resolved process where a photon remnant is apparent in the final state, though often with a low transverse momentum. In this case the photon is believed not to be point-like but to exhibit some kind of hadronic structure, making the resolved process an important area of study. The photon structure function has been measured for real and virtual photons by H1 [21] [22] and for photons with small virtualities by Zeus [23].

2.3.1 Vector Meson Dominance

Modelling the hadronic nature of the photon is of course important to the study of the resolved process but in fact it also proves useful in the description of the soft category of interactions where QCD can not be used. The point-like photon can display a hadronic structure via the process $\gamma \rightarrow q\bar{q}$ so that the photon-proton interaction can in many ways be likened to that of a hadron-hadron collision. On this basis the Vector-Meson-Dominance Model (VMD) describes the photon in terms

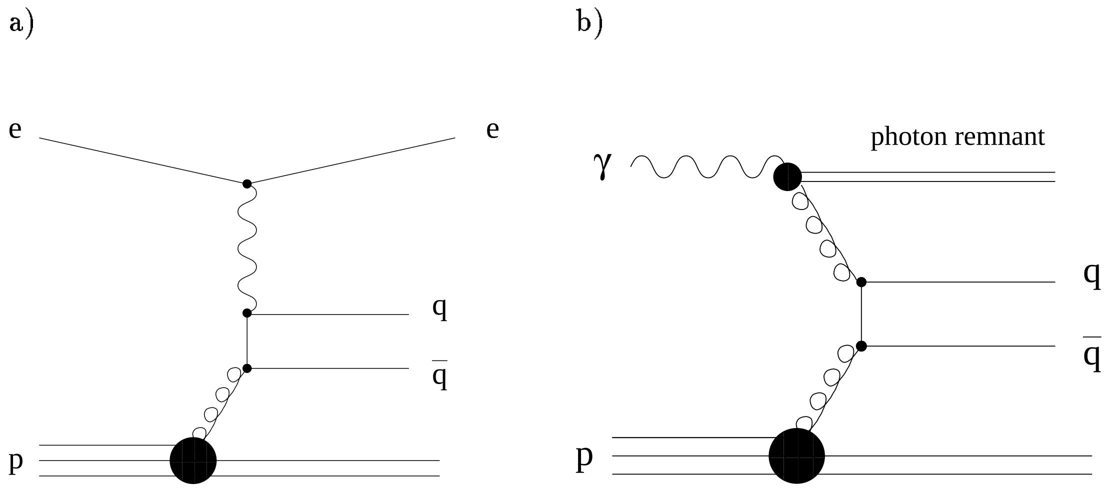

Figure 2.3: Diagram demonstrating the difference between direct and resolved processes. (a) shows the Boson-Gluon-Fusion (BGF) process where the photon behaves as a point-like object. (b) shows an example of a resolved process where only a fraction of the photon's momentum contributes to the hard process, the remaining fraction producing the photon remnant.

of a superposition of the bare photon component and a hadronic component. The largest contribution to the hadronic component comes from the lightest bound quark states of the ρ, ω and ϕ vector mesons which necessarily share the same quantum numbers as the photon. These are taken into account in the simplest version of the VMD [24] where each meson contributes according to its mass and its effective coupling to the photon. The generalised VMD [25] adds to the simpler model by including contributions from the heavier vector mesons (ρ', J/ψ , ψ', Υ) while the extended version of the VMD [26] goes even further and includes a spectrum of unbound quark states with the appropriate quantum numbers.

2.3.2 Regge Theory

A phenomenological method which successfully explained the hadron-hadron scattering cross sections was introduced by Regge in 1959 [27]. This theory models the strong interaction between hadrons as being mediated by a series of colourless objects called 'reggeons', which result in there being no exchange of the colour charge between the incident particles. This was used to explain a group of events which displayed a large angular (rapidity) gap between the remnants of each of the hadrons.

Similar events are also observed in DIS and photoproduction at HERA where a gap, free of hadrons, is seen between the proton remnant and the current region. These events which are thought, at HERA, to be due to the exchange of a colourless object called the pomeron, are referred to as diffraction. Treating the photon as a hadronic state described by VMD, models based on Regge theory have been used to describe soft diffractive processes where perturbative QCD is not applicable. By studying diffractive photoproduction this model can be experimentally tested giving information about the nature of the exchange particle. In diffractive DIS, where there is a hard scale, it is possible to go further and actually probe its partonic structure.

In 1935 Yukawa [28] predicted the existence of the π^0 meson as a way of explaining the finite range of the strong force in terms of the exchange of a massive particle. Using the uncertainty principle which relates the range of a force to the mass of the exchange particle he managed to estimate the mass of the π^0 before its discovery. Now however it is understood that the π^0 is only the lightest of the possible exchange states. The heavier the meson exchanged the shorter the range of influence so that when considering high energy interactions between nucleons all the contributions to the strong force need to be considered. Obviously this is extremely complicated given the large number of known mesons and this is the problem addressed by Regge theory. A full description of how the theory was formulated is contained in [29] and [30].

The key to the solution was recognising that the meson resonances followed a pattern which can be seen when their spin, α, is plotted against the square of their masses, M^2. Mesons which share the same quantum numbers other than that of spin are found to sit on approximately straight lines called Regge trajectories which describe the exchange. Observed resonances sit at values of $\mathrm{M}^2 > 0$ so that t, the four momentum squared of the exchange defined by:

$$t = (p - p')^2, \tag{2.12}$$

is positive. Conversely, the virtual mesons which have values of $\mathrm{M}^2 < 0$ have negative values of t. In this thesis the use of t now refers to the positive value $|t|$. The relationship between the spin of mesons and t can now be described using the equation for a straight line so that:

$$\alpha(t) = \alpha(0) + \alpha' t, \tag{2.13}$$

where $\alpha(0)$ and α' represent the intercept and gradient of the trajectory.

Unfortunately, all the known meson trajectories give values of $\alpha(0)$ <0.6, which fail to model the data obtained from HERA. If the exchange in strong interactions occurs purely by the exchange of mesons then the total and elastic cross sections are expected to decrease as a function of the centre of mass energy of the interaction. This does indeed occur in low energy experiments where $\sqrt{s}$ <10 GeV but at HERA's high energies an increase of the cross sections is seen. To reconcile this with Regge theory a new trajectory representing the pomeron, $I\!P$, is introduced. The pomeron has the quantum numbers of the vacuum and dominates the exchange at high energies so that at HERA the differential cross section, at fixed t, of soft diffractive processes is found to be:

$$\frac{d\sigma}{dt} \propto \left(\frac{W^2}{W_0^2}\right)^{2\alpha_{I\!P}(t)-2} . \tag{2.14}$$

where $\alpha_{I\!P}$ represents the pomeron trajectory and W=$W_{\gamma p}$, measured relative to the arbitrary value of $W_{\gamma p} = W_0$. The cross sections of soft diffractive processes are found to be enhanced at low values of t. This strong forward peaking is described well by an exponential function so that the variation of the differential cross section as a function of t and at fixed W can be expressed as:

$$\frac{d\sigma}{dt} \propto e^{-b_0 t} \tag{2.15}$$

The constant b_0 can be related, via the optical theorem, to the radii squared of the two objects participating in the elastic scatter. Combining these two relationships gives the general expression of the cross section:

$$\frac{d\sigma}{dt} \propto \left(\frac{W^2}{W_0^2}\right)^{2\alpha_{I\!P}(0)-2} e^{-bt} \tag{2.16}$$

where b is referred to as the slope parameter and is defined as:

$$b = b_0 + 4\alpha'_{I\!P} \ln\left(\frac{W}{W_0}\right) . \tag{2.17}$$

Equation 2.16 shows that the essential parameters modelling the behaviour of the cross section of soft diffractive processes are the pomeron intercept, $\alpha_{I\!P}(0)$, and the slope parameter, b. Measurements made of the energy dependence of the differential cross section can give experimental information on the nature of the pomeron. Likewise, a test of Regge theory can be made by determining the value of b from experiment. Equation 2.17 shows that b has a $W_{\gamma p}$ dependence which, providing $\alpha'_{I\!P}$ is greater than zero, causes the forward peak of the distribution relating the differential cross section to t to narrow as the energy increases. This effect is called 'shrinkage' and has been observed in hadron-hadron scattering [31].

Regge theory can also predict the energy dependence of the total cross section. Using the optical theorem the imaginary part of the of the forward (t=0) scattering amplitude can be related to the total cross section. The real part is assumed to be zero for soft diffractive events. Thus, for a general elastic collision

$$\sigma_{tot}(AB) \sim \left(\frac{s}{s_0}\right)^{\alpha(0)-1} \tag{2.18}$$

where s is the centre-of-mass energy squared and α represents the trajectory intercept of the exchange. Donnachie and Landshoff [32] found that it was possible to achieve good fits to the total cross section data from pp, πp and γp experiments using a single function for α. This fit is marked in figure 2.4 [33] which shows the HERA data along with low energy results. The function takes into account contributions from meson and pomeron exchange. The meson contribution, which is referred to as a reggeon, dominates at low energies due to its larger coupling to the hadrons. However, this coupling reduces with energy so that at high energies the pomeron term is most significant. From this fitting of the data, universal values for the reggeon and pomeron intercepts have been found so that $\alpha_{I\!R}(0)$=0.55 and $\alpha_{I\!P}(0)$=1.080. These can be used in the predictions for elastic scattering.

Regge theory has been found to be successful in describing soft diffractive processes in hadron-hadron scattering and in photoproduction. The introduction of the soft Donnachie-Landshoff pomeron has allowed the total cross sections of a variety of experiments to be understood using a single parameterisation and the diffractive production of the light vector mesons at HERA is also well described using this model. However, the same parameterisation seems unable to describe the diffractive processes which contain a hard scale, such as DIS and the diffractive production of the J/ψ meson. These demonstrate much steeper energy dependences than those predicted by Regge theory and a soft pomeron. In these cases models have been developed using perturbative QCD to describe diffraction in terms of a hard subprocess. Some of these models are discussed in relation to the production of the J/ψ meson in the next section.

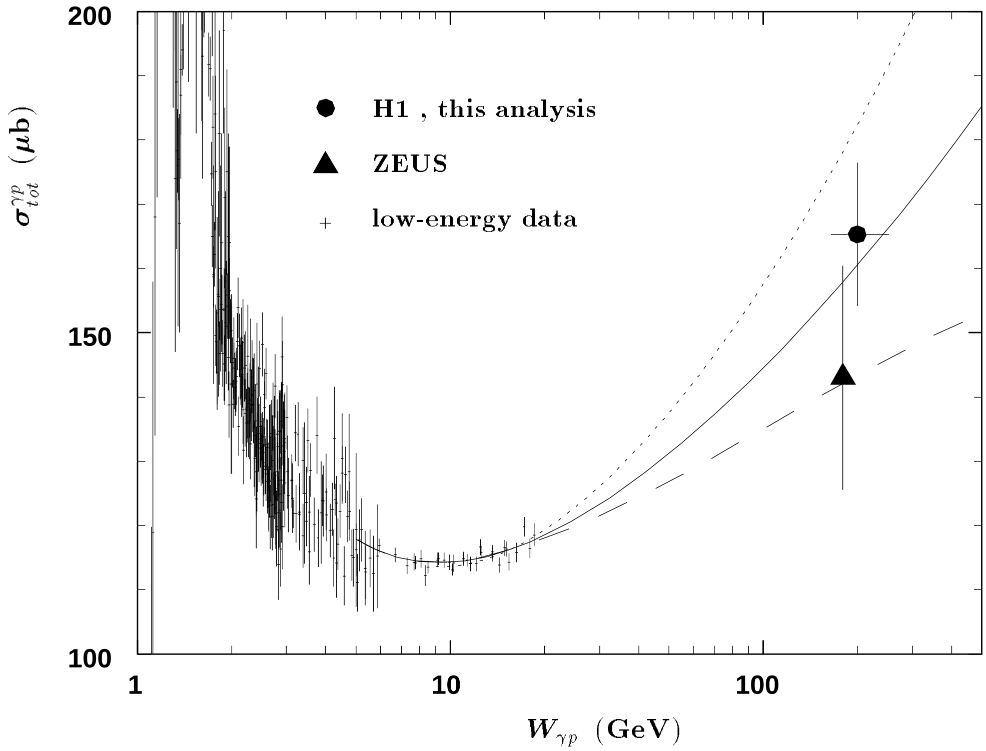

Figure 2.4: Figure showing the total cross section from a variety of experiments as a function of $W_{\gamma p}$. The solid line shows the Donnachie and Landshoff fit described in the text. Figure is taken from [33].

2.4 The J/ψ Meson

The discovery of the J/ψ meson at SLAC and Brookhaven in 1974 was interpreted as a bound state of a new and heavier quark called charm (c) and its antiparticle ($\bar{c}$). It was also suggested at the time that these charmed mesons carried a new quantum number called charm which was conserved, like strangeness, in strong and electromagnetic interactions. This turned out to be accurate as in the years following a whole spectrum of bound charmed states were identified which fell neatly into this scheme. These mesons are generically called charmonium and a list of those that have been identified to date, along with their quantum numbers and masses is included in table 2.1. These particles are also described as 'hidden charm' states since the net charm of the system is zero. Apart from charmonium there is another category of mesons where only one of the constituent quarks is of the charm variety. These mesons, for example $D^0(c\bar{u})$, are referred to as 'open charm' due to their possessing net charm.

Name	J^{PC}	Mass (MeV)
η_c(1S)	0^{-+}	2.98
J/ψ (1S)	1^{--}	3.10
χ_{c0}(1P)	0^{++}	3.42
χ_{c1}(1P)	1^{++}	3.51
h$_c$(1P)[2]	$?^{??}$	~3.5
χ_{c2}(1P)	2^{++}	3.56
η_c(2S)[2]	$?^{?+}$	3.59
ψ(2S)[3]	1^{--}	3.69
ψ(3770)	1^{--}	3.77
ψ(4040)	1^{--}	4.04
ψ(4160)	1^{--}	4.16
ψ(4160)	1^{--}	4.16
ψ(4415)	1^{--}	4.42

Table 2.1: A list of known charmonium states. The quantum numbers J^{PC} refer respectively to the orbital angular momentum, the parity and the C-parity (=$(-1)^{L+S}$) of the state. Data taken from [34].

The fact that the ψ mesons share the same quantum numbers as the photon means that they can be produced directly in e^+e^- and ep interactions where the mediating particle is the virtual photon. This makes it a convenient system in which to study hidden charm. The heaviness of the charm mass ($\approx \frac{M(J/\psi)}{2} \approx 1.5\,\mathrm{GeV}$) allows the combined object to be treated as a non-relativistic system. In this way the potential between the c and $\bar{c}$ quarks can be approximated with a simple Coulomb-like potential at short range and a confining potential proportional to r at longer distances. This means that the function describing the potential as a function of distance r can be written as:

$$V(r) = \frac{4\alpha_s}{3r} + ar, \tag{2.19}$$

where the $\frac{4}{3}$ is the colour factor associated with the strong coupling, α_s, and a is a constant. This simple model is successful in describing the spin, orbital angular momentum and total angular momentum states of the charmonium spectrum. The mass of the charm quark also makes it possible to apply perturbative QCD to the production of the J/ψ meson even in photoproduction. Since it then sits in

---

[2] The discovery of this state has not been confirmed.

[3] This state is also referred to as ψ'

the transition region between the definitively hard and soft processes, the study of J/ψ production should throw light on the pomeron in this ambiguous region.

A noteworthy characteristic of the J/ψ resonance is that it is very narrow. This is now understood as being due to Zweig suppression and in fact applies to all the charmonium states with masses below 3.73 MeV. This energy cut-off is significant due to its being twice the mass of the lightest charmed mesons called the D-mesons. If a bound charmed state lies below this energy cut-off it can only decay strongly to non-charmed mesons due to the restriction imposed by energy conservation. When colour and parity are conserved the coupling between the charmed J/ψ and its uncharmed hadronic decay can only be achieved with a minimum of three gluons as shown in figure 2.5(a). This process is heavily suppressed allowing the electromagnetic decay of the J/ψ to a lepton pair to take a larger proportion of the branching ratio. This suppression of the strong decay also applies to the ψ' resonance which lies above the J/ψ . The next meson in the spectrum is the $\psi(3770)$ meson with a mass of 3.77 Mev; this is permitted to decay to charmed mesons as shown in figure 2.5(b) and thus displays a broader resonance more in keeping with a hadronic decay. These broader resonances are more difficult to identify experimentally making the higher mass states less well measured.

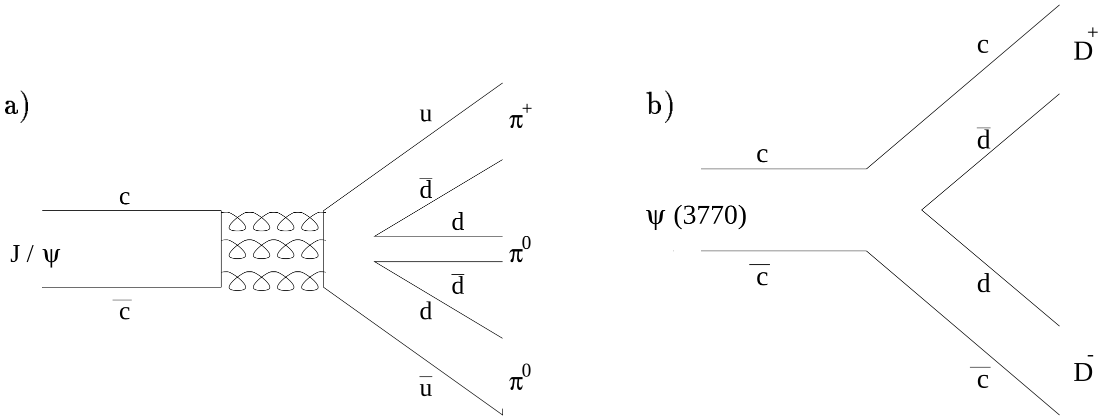

Figure 2.5: Diagrams demonstrating Zweig suppression in the decay of charmonium via the strong interaction. (a) shows how the J/ψ is forced to decay to non-charm hadrons via three gluons. This decay is suppressed making the electromagnetic decay to lepton pairs more significant than for higher charmonium states. (b) shows how the $\psi(3770)$ state is heavy enough to decay to a pair of D mesons so that the suppression isn't apparent.

It is possible for the ψ mesons to be produced in both inelastic and elastic collisions at HERA and these are discussed in general in [35]. Where they are produced in-elastically colour charge is transferred between the proton and the final charm state so that the proton breaks up leaving a hadronic final state along with the decay products of the meson. Alternatively, they can be produced elastically through the so called diffractive process where the proton remains intact or at most dissociates into fragments with low transverse momenta. In this case the final state consists only of the decay products of the meson. When discussing the elasticity of a process it is useful to introduce the scaling variable z which is defined as:

$$z = \frac{p \cdot p_\psi}{p \cdot q}, \tag{2.20}$$

where p and q represent the four-momenta of the proton and photon as shown in figure 2.1 and p_ψ is the four-momentum of the produced meson. In the rest frame of the proton $z{=}\frac{E_\psi}{E_\gamma}$ so that it runs between $0{<}\,z\,{<}1$ and at the extreme where the meson retains all the photon energy $z{\approx}1$ and the process is described as elastic.

2.4.1 Inelastic Production

The predominant in-elastic ($z \lesssim 0.9$) mechanism for the photoproduction of J/ψ mesons is BGF. This process, described diagrammatically in figure 2.3(a), involves the photon taking part in a hard interaction with a gluon in the proton to form a $c\bar{c}$ pair. The mass of the charm quark provides a hard scale so that this hard interaction, which is sensitive to the gluon content of the proton, can be calculated using perturbative QCD. The formation of the J/ψ meson from the $c\bar{c}$ pair is considered to be a separate process which takes place non-perturbatively.

In the colour-singlet (CS) model [36], shown in figure 2.6, a gluon is also produced in the hard interaction so that the $c\bar{c}$ pair is in a colourless state like the J/ψ into which it will be formed. Alternatively, it is proposed that the $c\bar{c}$ pair can be produced via the colour-octet model [37] where it retains its colour at the hard interaction stage and only sheds it by the emission of soft (non-perturbative) gluons before the formation of the J/ψ meson. The colour-octet model has been used to try and explain the excess rate of heavy flavour production at the Tevatron $p\bar{p}$ collider [38]; however, as yet, HERA has seen no evidence of a similar excess in their data [39]. The theoretical next-to-leading-order predictions arising from the colour-singlet model have been compared to low energy data from EMC and to HERA data and good agreement has been found providing a steep gluon density in the proton is used at low x [40] [41]. The measurement of the gluon distribution in the proton is very sensitive to the model of inelastic production used, so that any significant contribution from the colour-octet process needs to be recognised and understood.

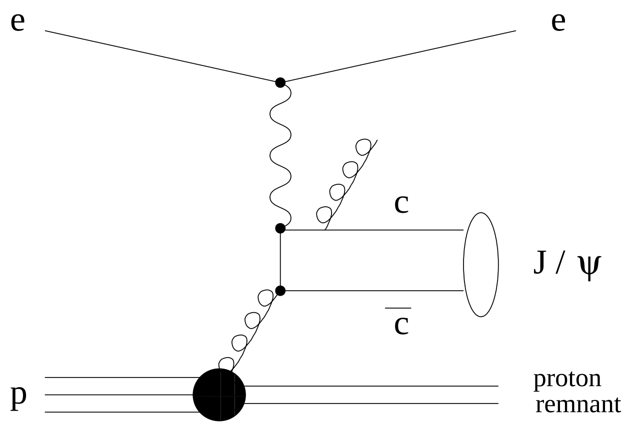

Figure 2.6: Diagram showing the colour-singlet mechanism for J/ψ production.

The photoproduction of the J/ψ meson can also occur in resolved processes where a parton from the photon couples with a parton from the proton. One example of this is gluon-gluon fusion where the the colour singlet process would look like:

$$\gamma p \rightarrow g_\gamma + g_p \rightarrow c\bar{c}(^3S_1) + g \rightarrow J/\psi + g \tag{2.21}$$

These contributions are found to be small at HERA only contributing significantly to the region z <0.4. Indirect mechanisms where the J/ψ is the decay product of a higher mass charmonium state or a B-meson are also possible but these contributions are considered to be small.

2.4.2 Elastic Production

The use of the term elastic at HERA is not an accurate one. Strictly, an elastic process is one where the rest mass of the final state is equal to that of the initial state and this is clearly not so for the exclusive reaction $\gamma p \longrightarrow J/\psi + p$. However, despite this, it is conventional to refer to this process as elastic since the required momentum transfer from the proton is considered negligible compared to the high centre-of-mass energies available at HERA. The elastic process has values of the elasticity variable z=1. There is another category of events which are not elastic but which have values of z close to one. Like the elastic process no colour is transferred from the proton to the charm final state and though the proton breaks up, its fragments have low transverse momenta. These cases are described as proton-dissociative and these together with the elastic process lie in the 'quasi-elastic' region where $z > 0.95$.

Elastic and proton-dissociative J/ψ production are generally described using phenomological models of soft-diffractive processes. Donnachie and Landshoff [42] have developed predictions for the exclusive production of vector mesons using Regge theory which was originally designed to model soft-hadronic interactions. However, by exploiting the hadronic behaviour of the photon described by VMD, the elastic process can be treated as a hadron-hadron interaction where the photon fluctuates into an off-shell J/ψ which is put on-shell by a small momentum transfer from the proton. In this way the HERA process $\gamma + p \longrightarrow J/\psi + p$ can be related to the truly elastic process $J/\psi + p \longrightarrow J/\psi + p$ which are found to share the same energy dependences of their cross sections. In the Donnachie-Landshoff model the interaction between the virtual J/ψ and the proton is mediated by the soft pomeron, which is conjectured to be two or more non-perturbative gluons, or possibly a glueball [43]. This diffractive mechanism is shown in figure 2.7 for the elastic and proton-dissociative processes.

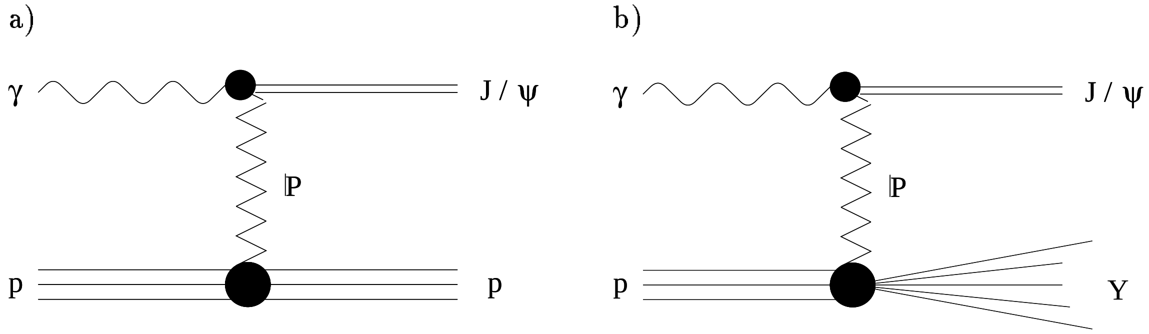

Figure 2.7: Diagrams showing the diffractive production mechanism for quasi-elastic J/ψ production. (a) shows the elastic process and (b) shows the proton-dissociative process.

Equation 2.16 shows how the cross section of an elastic process is related to $W_{\gamma p}$ within the constraints of Regge theory. Using the value of the pomeron intercept, extracted by Donnachie and Landshoff by fitting the total cross sections of γp and hadron-hadron experiments, the rise of the cross section as a function of $W_{\gamma p}$ can be evaluated. In this way the relationship is found to be:

$$\left.\frac{d\sigma_{el}}{dt}\right|_{t=0} \propto W_{\gamma p}^{4\epsilon} \tag{2.22}$$

where $\epsilon = \alpha_{I\!P}(t) - 1$. Assuming that shrinkage exists, so that $\alpha'_{I\!P} > 0$, the Donnachie-Landshoff parameterisation predicts a slow rise of the elastic J/ψ cross section so that $\sigma_{el} \propto W_{\gamma p}^{0.22}$. Where no shrinkage exists and $\alpha'_{I\!P}=0$ equation 2.22 reduces to $\sigma_{el} \propto W_{\gamma p}^{0.32}$ so that a slightly steeper rise is expected.

The t dependence of the differential cross section, as can be seen from equation 2.16, is assumed to be an exponential function, where the parameter b describes the slope. In the photoproduction region, where $Q^2 \approx 0$, t can be approximated to $-p_t^2(J/\psi)$ the negative transverse momentum squared of the J/ψ meson. This approximation is used to measure b in order to check whether the phenomenon of shrinkage, which is inherent to Regge based models, is observed.

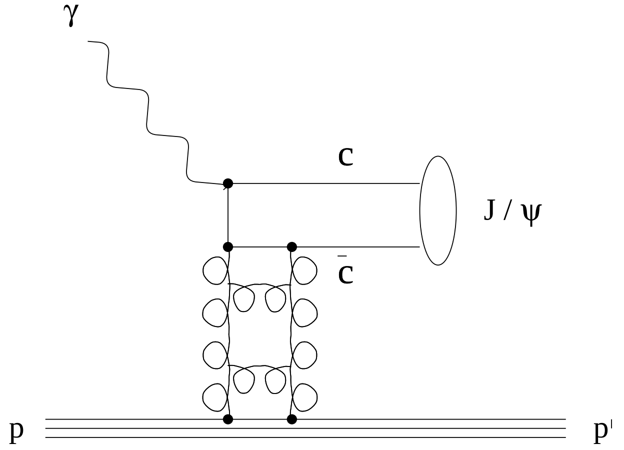

Figure 2.8: Diagram showing a QCD mechanism for the elastic production of J/ψ mesons. Here the exchange between the charm system and the proton occurs via a gluon ladder.

Lately, attempts have been made to describe the elastic production of the J/ψ in terms of perturbative QCD. This is thought to be possible due to the hard scale provided by the mass of the charm quark. A model by Ryskin [44] replaces the soft pomeron by a hard version which is constructed from gluons. In the simplest form the exchange particle can be formed from two gluons with higher orders creating more complicated structures such as the gluon ladder shown in figure 2.8. The model assumes that the elastic process can be factorised into three separate parts: the transition $\gamma \rightarrow c\bar{c}$; the scattering of the $c\bar{c}$ on the proton via a colourless exchange and then finally the formation of the J/ψ meson from the $c\bar{c}$ pair. The scattering of the quark pair off the proton takes place over a much shorter time-scale than the other two parts of the process. Ryskin has shown that the cross section of the process depends on the squared of the gluon distribution in the proton. The GRV [45] and MRSA′ [46] distributions, which show a gluon density increasing towards low values of x and have been found to describe the F_2 measurements at HERA, are used to model the energy dependence of the elastic J/ψ cross section. The use of these distributions, to differing degrees, results in a steeper rise in the J/ψ cross section than that predicted by soft pomeron exchange.

The nature of the pomeron in diffractive interactions is of great interest at HERA. The light vector mesons are well described by the soft pomeron, whereas high Q^2 interactions appear to be described by the hard BFKL pomeron which is developed using QCD. The transition between the hard and soft models is not yet understood and it is not clear whether the models should be used separately or whether they should be mixed, perhaps as a function of Q^2 [43]. The elastic production of J/ψ mesons at HERA promises to provide information on the pomeron in this transition region and distinguish between the hard and soft models that have been developed to describe its behaviour.

Chapter 3

HERA and the H1 Detector

3.1 Introduction

The HERA machine started producing data in 1992 and is the first and only *ep* collider that has been built to date. In 1995 it produced collisions between 27.5 GeV positrons and 820 GeV protons thereby accessing a centre-of-mass energy of 300 GeV - a factor of 10 larger than previous fixed target experiments. The electrons and protons are accelerated and kept in separate storage rings located side by side in a 6.3 km long tunnel. The positron and proton 'beams' each consist of 174 bunches of particles which are timed to pass through each other at two locations where the storage rings merge together. This is referred to as a 'bunch crossing' and these occur at 96 ns intervals. In addition to the colliding bunches there are 15 positron and 6 proton pilot bunches. These are non-colliding and are used to study and estimate the backgrounds produced when beam particles interact either with residual gas in the beam-pipe (beam gas) or the beam-pipe itself (beam-wall).

There are four experiments located around the HERA storage rings: H1(North), Zeus(South), HERMES(East) and HERA-B(West). H1 and Zeus are built around the two interaction points and are designed as general-purpose detectors to study all aspects of *ep* scattering. In contrast HERMES and HERA-B are dedicated experiments. HERMES [47] [48] only uses HERA's positron beam which is longitudinally polarised before it enters the experiment where it collides with a fixed, polarised gas target. It is designed to measure the spin distributions of the quarks in the nucleons and since taking data in 1995 has produced preliminary results for spin structure functions of the nucleon. HERA-B on the other hand plans to only use HERA's proton beam. This experiment is at present under construction; however, it will consist of wire targets being introduced to the beam-pipe in order to investigate CP violation in the B system.

The general-purpose objective of the H1 detector meant that its design needed to satisfy wide ranging physics specifications. To this end the detector has been constructed to detect as many of the products from the *ep* collision as possible using a mixture of tracking and calorimetry. In fact the hermeticity is almost complete apart from the space occupied by the beam-pipe. An asymmetric layout of the detector is necessary due to the large asymmetry in the beam energies which results in collision products being Lorentz boosted in the laboratory frame along the proton direction. Thus, the detector components concentrated in the forward region need to be able to cope with large track multiplicites and high momentum measurements. Good hermetic calorimetry over the whole detector is a another requirement of the design. This is necessary for the study of energy flow, particularly charged current events which are identified by a neutrino inferred from missing transverse energy. In the same way the tracking systems are built with specified resolutions to enable the study of high density jet events. Lepton identification and measurement is important for the study of the heavy quark resonances and new exotic particles as well as in locating the scattered positron. In the case of electrons and positrons calorimetry is used in combination with tracking systems; for the more penetrating muons a muon system is also employed.

Rejection of background interactions is also an essential feature of the H1 detector. An *ep* collision is only expected to happen once every 10^3 bunch crossings and these events have to be distinguished from the high backgrounds produced by synchrotron radiation conversions, cosmics and beam-gas and wall interactions. It is necessary to be selective about which events are recorded otherwise the data from the detector components would be too vast to store and the dead time that this storing would impose on the detector would mean that real physics events would be missed. H1 uses a multi-level triggering system which takes quick decisions on-line using information from the sub-detectors. One example is the use of the reconstructed event vertex to reject a substantial fraction of the background.

A diagram of the H1 detector is shown in figure 3.1 and described in detail in [49]. The main section of the detector includes the tracking system $\boxed{2}\,\boxed{3}$; the calorimetry $\boxed{4}$ $\boxed{5}$ $\boxed{12}$ $\boxed{13}$; the super-conducting solenoid $\boxed{6}$ and lastly the muon system $\boxed{9}\,\boxed{10}$. Not shown in the diagram are the proton and electron taggers and the photon detector. What follows in the remaining sections of this chapter is a general description of these sub-components.

$\boxed{1}$	Beam pipe and beam magnets
$\boxed{2}$	Central tracking detector
$\boxed{3}$	Forward tracking detector
$\boxed{4}$	Electromagnetic calorimeter
$\boxed{5}$	Hadronic calorimeter
$\boxed{6}$	Solenoid
$\boxed{7}$	Compensating magnet
$\boxed{8}$	Helium supply for $\boxed{7}$
$\boxed{9}$	Muon chambers
$\boxed{10}$	Instrumented iron return yoke
$\boxed{11}$	Forward muon toroid
$\boxed{12}$	SpaCal
$\boxed{13}$	Plug calorimeter
$\boxed{14}$	Concrete shielding
$\boxed{15}$	Liquid argon cryostat

Figure 3.1: Diagram showing the components of the H1 detector.

A Cartesian coordinate system has been defined to describe the detector and is indicated on the diagram. Its origin lies at the nominal interaction point; the positive z direction lies along the direction of the proton beam and the positive y direction points vertically upwards. Thus, the corresponding spherical coordinate system gives the polar angle, θ=0 along the proton direction and θ=180° in the electron direction. Further, $\theta < 90^\circ$ and $\theta > 90^\circ$ are referred to as the 'forward' and 'backward' regions respectively.

3.2 Tracking

The tracking system is situated at the core of the H1 detector surrounding the interaction region. Its purpose is to reconstruct the paths of charged particles passing through the detector and to determine their charge and momentum. This is achieved using a combination of drift chambers and multi-wire proportional chambers (MWPCs) [50]. All the tracking detectors are situated inside the 1.15 T magnetic field provided by the super-conducting solenoid. The drift chambers are used to plot particle trajectories and analysis of the curvature of the track in the magnetic field gives measurements of the particle's momentum and charge. Particle identification is aided by measurements of the specific energy loss dE/dx [50] and potentially by transition radiators. The proportional chambers are used primarily to provide track triggering information because of their fast response times. The tracking system as a whole is designed to provide a momentum measurement for a charged track with a precision given by $\frac{\sigma_p}{p^2} \approx 3 \times 10^{-3}\,\mathrm{GeV}^{-1}$, and a polar angle measurement such that, $\sigma_\theta \approx 1\,\mathrm{mrad}$.

The tracking system, shown pictorially in figure 3.2, is made up of 3 separate sections: the forward tracking detector (FTD) which covers the angular region $5^\circ < \theta < 25^\circ$; the central tracking detector (CTD) which covers the region $15^\circ < \theta < 165^\circ$ and lastly the Backward Drift Chambers (BDC) which extends from $157^\circ < \theta < 177^\circ$. Where particles pass through more than one of these detectors, links between track segments are made to reconstruct the track through the whole of the system.

The Central Tracker

A radial view of the CTD is shown in figure 3.3. Its major feature is two large, concentric jet chambers, CJC1 and CJC2 which have drift cells tilted at 30° to the

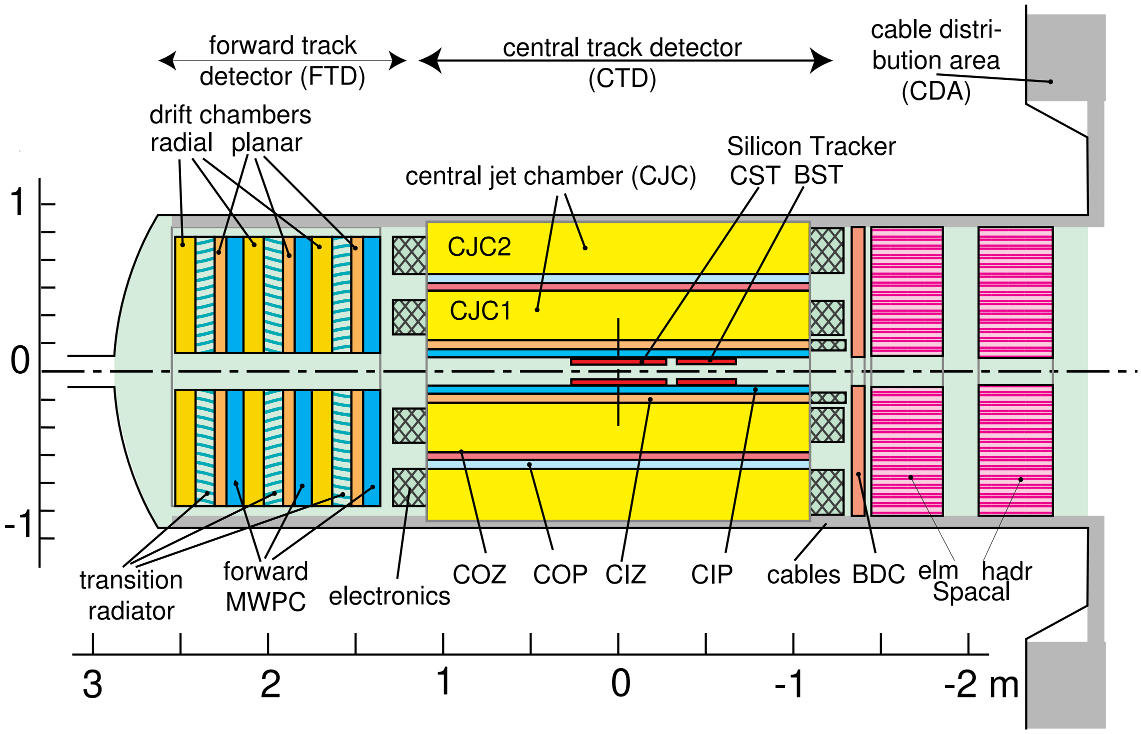

Figure 3.2: Diagram showing the tracking system of the H1 detector.

radial direction so that tracks of all momenta are sampled several times by both chambers. The tilt also ensures that the drift direction for high momenta tracks is never far from being perpendicular to the track direction. CJC1 has 30 cells with 24 wires each; CJC2 has 60 cells with 32 wires each and the sense wires of both are strung parallel to the z-axis of the H1 detector. These chambers provide a spatial resolution of $170\,\mu$m in the $r - \phi$ plane and any drift ambiguities, due to the uncertainty as to which side of the wire the track passed, are resolved by combining information from a number of cells. Both ends of each sense wire are read out to allow a z-coordinate to be determined using a method of charge division, the resolution of which is ~ 2 cm. This is complemented by the more accurate measurement from the z-chambers (CIZ and COZ) which has a resolution of $\sim 300\,\mu$m. The CIZ and COZ are located inside and outside of CJC1 respectively. They are made up of 16 cells and 24 cells, each of which has four sense wires which are strung azimuthally so that the drift direction is roughly along the z-axis.

The proportional chambers, CIP and COP, line the inside of the CIZ and the outside of the COZ respectively. These can establish quickly, though crudely, the position and direction of a particle track. This information is useful for triggering on tracks

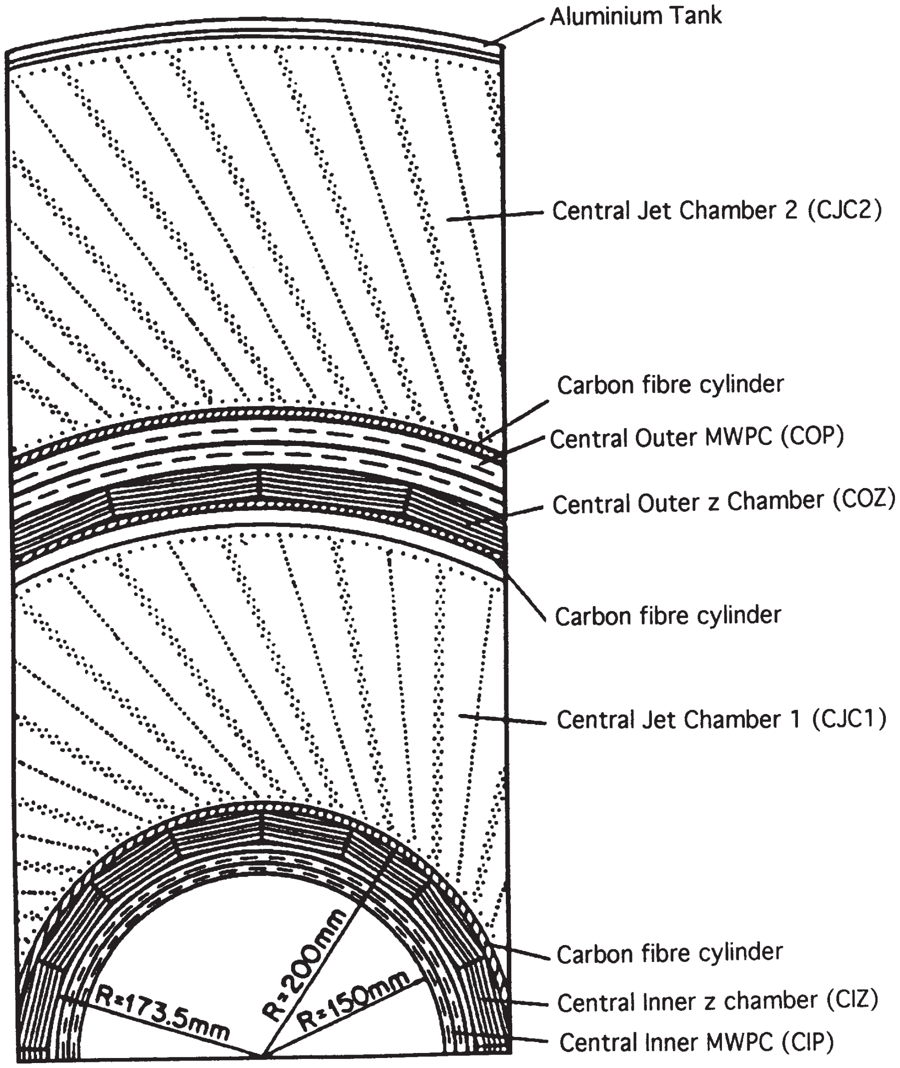

Figure 3.3: Diagram showing the central tracking system of the H1 detector.

pointing to the nominal vertex. This is an important aspect of the level 1 trigger (see section 3.7) which has to distinguish between ep interactions and backgrounds. The detectors are made up of 2 concentric layers of chambers whose signals are read out from cathode pads. The CIP has 480 wires in each of its layers while the COP has 1574 wires in one layer and 1615 wires in the other. All the sense wires are strung parallel to the z-axis.

The Forward Tracker

The FTD consists of 3 similar 'super-modules', each of which comprises, in order of increasing z, planar drift chambers, a MWPC, a transition radiator and a radial drift chamber.

In each module there are 3 layers of planar drift chambers each of which has 32 cells which are 4 wires deep in z. The sense wires in a layer are strung parallel to each other in the r-ϕ plane, and the 3 layers are offset relative to each other by 60° . The sense wires are only read out from one end, so the information from the 3 layers is combined to give the θ coordinate of the incident track. The purpose of the MWPC planes is the same as those in the central region; they provide a quick signal to the level 1 trigger for background removal. The signal is read out from the cathode pads which lie between two planes of wires. The pads are ring shaped and are positioned so that they run concentric to the beam pipe, their circumference increasing from the centre of the plane, out to the edge. Each pad covers an azimuthal angle of 22.5° or 45° and are 18 mm thick at the centre of the plane rising to 37 mm at the outer edge.

The particle identification in the forward tracking region is provided by the transition radiators. In particular, they help separate $e^{\pm}$ signals from those of pions. They are made up of 400 closely spaced polypropylene films with layers of gas in between. When a charged particle crosses the foil boundaries low angled photons (X-rays) are produced which are detected as increased charge in the signals of the radial drift chambers. The intensity of the X-rays is dependent on the Lorentz factor, γ=Energy/Mass, of the charged particle so that particles of different masses can be differentiated.

Lastly, the radial drift chambers in each module are designed to provide an accurate ϕ measurement to complement the θ coordinate obtained from the planar chambers. To achieve this the sense wires are strung radially. A layer has 48 segments in ϕ each of which contains 12 sense wires separated by 10 mm in z. The wires are read out from both ends so a crude measurement of the θ coordinate can also be made. The potential is provided by wires between the sense wires and strips on the walls of the chamber to provide a uniform drift field. The gas mix in the chamber contains xenon which is suitable for detecting the X-rays produced in the transition radiators.

The Backward Drift Chambers

Above an angle of 155° tracks are not adequately reconstructed in the CTD. However, accurate track reconstruction in the backward direction is important for the identification and momentum measurement of the scattered positron. Extending the detector coverage to very low angles allows the low x and low Q^2 kinematic domain to be investigated. Hermetic coverage is also useful for energy flow measurements. To these ends the BDC was installed during the shutdown in 1994/1995. It is designed to determine the scattering angle of the electron to an accuracy of 5 mrad and to identify the track's position on entry to the SpaCal calorimeter, which is positioned behind the BDC, with a resolution of 1 mm [51]. These drift chambers also provide fast signals for the level 1 trigger.

The BDC consists of 5 octagonal chamber planes, each of which is rotated by 18° in ϕ relative to the one in front. Each plane contains two layers of sense wires which are shifted slightly relative to each other to resolve any drift ambiguities.

3.3 Calorimetry

The calorimetry at H1 is designed to provide identification and energy measurements of the scattered positron and other charged and neutral particles in the final state. The H1 calorimetry is made up of the Liquid Argon Calorimeter (LAr) which has almost hermetic coverage over the angular range of $4^\circ < \theta < 154^\circ$; the SpaCal which covers the range $155^\circ < \theta < 174^\circ$; and the plug calorimeter which is designed to fill the gap between the LAr and the beam-pipe in the forward region. These all lie within the super-conducting coil to minimise the amounts of dead material between the interaction point and the calorimeters. Lastly, the tail-catcher (TC) surrounds all these components and acts as both a return yoke for the magnet and a final layer of instrumentation for very penetrating particles. A diagram of the calorimetry at H1 is shown in figure 3.4.

All the detector components use the same principles [50], though the choice of materials and the technical details are specific to each case. This is necessary because of the different showering mechanisms of electrons (or photons) and hadrons and because of the different design criteria imposed on each of the components.

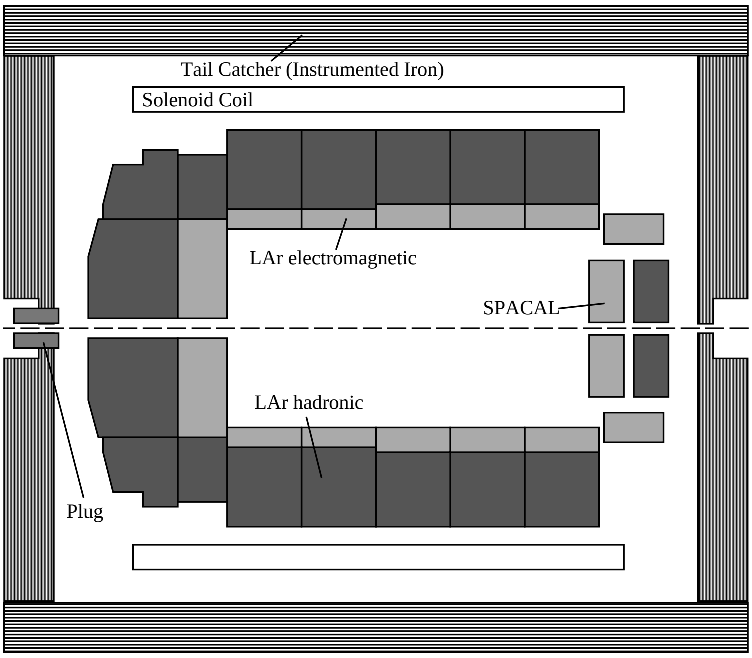

Figure 3.4: Diagram showing the calorimetry components of the H1 detector.

The calorimetry measures the energy of incident particles by summing the energy of the particle showers they induce in the detecting material. A signal is read out from sensitive layers, placed at intervals through the detecting material, which sample the particle showers. Electrons and photons lose their energy in the showering material through Bremsstrahlung and pair-production processes which create a particle avalanche which is characterised by the radiation length, X_0. In contrast, hadrons interact in-elastically with the nucleons of the absorbing material and produce lower energy secondary hadrons and nuclear fragments. Here the characteristic length of the shower is λ_i, the nuclear interaction length, which tends to be much larger than X_0. For hadronic showers corrections of $\sim 30\%$ [2] have to be made to allow for some of the incident particle's energy being dissipated via nuclear processes which are 'unseen' by the sampling layers. The energy resolution of both electromagnetic and hadronic calorimeters is limited by the statistical fluctuation in the numbers of particles produced in the shower so that $\frac{\sigma_E}{E} \propto E^{-\frac{1}{2}}$, where E is the energy of the incident particle. Other terms occur due to noise, calibration uncertainties, non-uniformity and shower non-containment.

The Liquid Argon Calorimeter

The LAr system [52] is the largest of the calorimeters and covers the majority of the solid angle at H1. It is the principal detector used in the detection of the scattered positron in high Q^2 events and in the identification and measurement of leptonic and hadronic final states. It is divided into two sections - the inner electromagnetic section (EMC) and the outer hadronic part (HAC) - though these are both housed in the same liquid argon cryostat. Liquid argon was chosen as the absorbing material for the calorimeter because of its high atomic density, chemical stability, ease of calibration and its homogeneity of response. Inside the cryostat the calorimeter is structured into 8 self-supporting wheels along the z direction, each of which is split into octants. Within each octant the EMC and HAC are segmented into cells where the number of cells is a compromise between minimising the number of cracks and maximising the granularity.

The EMC is constructed from layers of lead 2.4 mm thick separated by gaps of 2.35 mm filled with liquid argon. The depth of this section is between 20-30 X_0, the larger depth being in the forward region where particles with higher average energies are expected. The energy resolution for electrons is given by $\frac{\sigma_E}{E} = \frac{11.5\%}{\sqrt{E}} \oplus 1\%$, where E is the energy of the incident particle in GeV [53]. The calibration uncertainty was determined in test beams at CERN and is about 3% [53].

The HAC surrounds the EMC apart from in the very backward region. Its sampling layers are made from 19 mm thicknesses of stainless steel between which are two liquid argon gaps of 2.4 mm. The depth of this part of the LAr calorimeter ranges from 5-8 λ, substantially deeper than the electromagnetic section in order to contain the larger hadronic showers. The energy resolution was determined using pions and is somewhat poorer than that of the EMC with $\frac{\sigma_E}{E} = \frac{50\%}{\sqrt{E}} \oplus 2\%$ [54]. The precision of the calibration in this case is about 6 %.

The Spaghetti Calorimeter

The SpaCal [51] lies between the LAr calorimeter and the beam-pipe in the backward region and was installed during the 1994/1995 shutdown, along with the BDC. It has both an electromagnetic section, which is designed to detect the scattered positron in events with $1 < Q^2 < 100\,\mathrm{GeV}^2$, and a hadronic section. It also provides time of flight information which is important for differentiating between *ep* collisions and proton beam induced backgrounds.

The SpaCal is a lead/scintillating fibre calorimeter [50]. The electromagnetic part sits nearest to the interaction point and consists of 64 cells arranged in 4 'super-modules'. Each cell has a square face with dimensions $40.5 \times 40.5\,\mathrm{mm}^2$ and is made up of 0.5 mm diameter fibres embedded into layers of lead so that the ratio of the lead-to-fibre volume is 2.27:1. The depth of the section is $27\,X_0$ and this is sufficient to contain a 30 GeV shower without using the hadronic part of the SpaCal which sits behind. The response of the electromagnetic section is found to be linear over the energy range 10-60 GeV and has an energy resolution of $\frac{\sigma_E}{E} = \frac{7.1\%}{\sqrt{E}} \oplus 1.1\%$, and a spatial resolution of $\sigma_{xy} = \frac{4.4\,mm}{\sqrt{E}} \oplus 1\,\mathrm{mm}$ [55].

The hadronic section has the dual purpose of measuring any leakage from the electromagnetic section and measuring hadronic activity in the backward region. The main section is made of 128 cells, each with a cross section of $119.3 \times 119.3\,\mathrm{mm}^2$. The organisation of the cells is similar to that of the electromagnetic section, though here, the cells contain fibres with a 1 mm diameter so that the lead-to-fibre ratio is 3.4:1. The total depth of the electromagnetic plus hadronic sections is $2.02\,\lambda_i$. The gap between the iron yoke and the beam-pipe is filled with the backward plug which consists of 12 extra modules which are fitted close ($\approx 55\,\mathrm{mm}$) to the beam-pipe. This extends the coverage of the SpaCal down to $\theta = 178.7^\circ$, which lies in the Q^2 transition region between DIS and photoproduction events. The combined response of both sections of the SpaCal gives an energy resolution for hadrons of 29% and the probability of a pion being mistaken for an electron is $\sim \frac{1}{300}$ [56].

Time of Flight (ToF) measurements are a very useful way of reducing beam-gas and beam-wall backgrounds. These travel along with the proton beam entering the SpaCal from the backward direction. Particles from these interactions will reach the SpaCal $\sim \frac{z}{c}$ before the bunch crossing time, where z is the distance between the interaction point and the ToF measurement. These can be separated from particles coming from *ep* collisions which will be measured $\sim \frac{z}{c}$ after the bunch crossing. The timing resolution of the SpaCal is 0.4 ns [55] which is sufficient to resolve real collisions from proton backgrounds. ToF information is used by the Level 1 trigger (see section 3.7) to reject background events on-line.

The Plug Calorimeter

The purpose of the plug is to detect hadronic energy at low polar angles. It is designed to fill the gap between the LAr calorimeter and the beam-pipe in the forward direction. It consists of nine layers of copper interspersed with layers of silicon to sample the induced particle showers. Its energy resolution is limited by its poor containment and coarse sampling and is given by $\frac{\sigma_E}{E} \sim \frac{150\%}{\sqrt{E}}$.

The Tail-Catcher

The tail-catcher is, in this instance, designed to measure any hadronic energy leakage from the LAr calorimeter or the SpaCal and hence improve their resolution for particles with high energies. It is part of the iron return yoke which is instrumented with 16 layers of limited streamer tubes (LST) [50]. The first 11 layers are also fitted with readout pads which range in size from $28 \times 28\,\mathrm{cm}^2$ in the endcaps to $50 \times 50\,\mathrm{cm}^2$ in the barrel. The energy from the first five layers and the last six layers are summed together so effectively the TC is segmented into two longitudinally. The depth of the TC is $4.5\,\lambda_i$ and it gives an energy measurement with a precision of $\frac{\sigma_E}{E} \approx \frac{100\%}{\sqrt{E}}$.

3.4 Muon Detection

Muons are highly penetrating particles so the muon detectors at H1 are located furthest away from the interaction region. The muon system consists of the instrumented iron and the forward muon detector, which sits beyond the iron in the forward direction.

The Instrumented Iron

The instrumentation in the iron return yoke is principally used for the detection of muons though it is also used to contain showers from the LAr calorimeter (see section 3.3). The iron covers the angular region $6^\circ < \theta < 172^\circ$ and is segmented with 10 layers of LSTs. There are additional layers positioned before and after the iron making up a total of 16 instrumented layers. These are used to detect and reconstruct muon tracks with energies greater than $1.2\,\mathrm{GeV}$. An approximate momentum measurement for these muons can be made using the field in the return yoke, however, it is preferable to link the iron track to a track in the tracking system where the momentum measurement is more reliable.

Incident muons are detected by way of the ionisation they induce in the gas of the

LSTs. The tubes consist of a gas-tight box, with a cross-section of 1 cm^2, with a single wire running along its length. The wires are held at a ground potential and a high voltage is applied to the sides of the box. Five layers of tubes have cathode strips attached perpendicular to the wires and the remaining eleven layers are equipped with cathode pads. Signals are read out from the wires and the cathode pads or strips. The wires give a resolution of 3-4 mm in the coordinate perpendicular to the wire; the strips give a second coordinate with an accuracy of 10-15 mm and the pads give a two-dimensional point with a resolution of 10 cm. The readout of the pads is part of the LAr system though the information is used in the muon system to resolve any ambiguities. The LSTs are orientated along the z direction in the barrel and along the x direction in the endcaps.

The Forward Muon Detector

The Lorentz boost in the proton direction means that in general muons produced with low polar angles have higher momenta than those travelling backwards. Due to this the forward muon detector which covers the angular region $3^\circ < \theta < 17^\circ$ is designed to provide muon track reconstruction and momentum measurements to complement those from the iron. A diagram of the FMD [57] is shown in figure 3.5.

It is constructed from three double layers of drift cells on either side of a toroid magnet. Since the FMD sits outside the super-conducting solenoid it requires its own field to make momentum measurements. The toroid provides a field which decreases with radius so that at 65 cm the strength is 1.75 T and at 290 cm it is 1.5 T. The drift cell design is very simple in that they consist of 12 cm wide boxes with a single sense wire running down its length which varies between 34 cm and 241 cm long, depending on where on the plane they are located. On each side of the toroid there are two layers with drift cells orientated azimuthally around the beam-pipe. These determine an accurate polar coordinate for track segments in front of and behind the toroid. Between these is a layer with its drift cells arranged radially to measure the ϕ-coordinate of the track segment. The position coordinates can be determined with an accuracy of $\sim 250\,\mu$m. In each case a coarse measurement of the other coordinate is possible using the method of charge division. The momentum of the track is obtained by measuring the change in direction of the pre- and post-toroid track segments due to the magnetic field.

The FMD can measure the momentum of muons in its angular acceptance providing they are greater than 5 GeV and less than 100 GeV. The lower limit is set by the amount of material the muons have to penetrate to reach the detector and the effect of Coulomb scattering in the toroid on the momentum resolution of the muons. The upper limit comes from the deterioration in momentum resolution due to the finite spatial resolution of the drift chambers and misalignment effects.

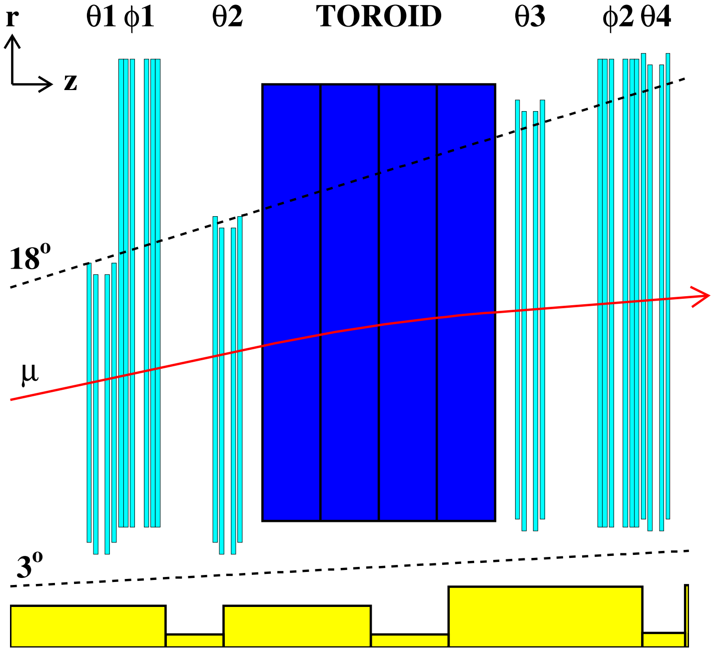

Figure 3.5: Diagram of the FMD

3.5 The Luminosity System

The luminosity measurement is made by detecting the final state positron and photon in the Bethe-Heitler process $ep \longrightarrow ep\gamma$, for which the cross section is well determined. The electron tagger (ET) is positioned at $z \approx -33\,\mathrm{m}$ and the photon detector (PD) further down the beam line at $z \approx -100\,\mathrm{m}$. The ET also serves to detect the scattered positron in photoproduction events where $Q^2 < 0.01\,\mathrm{GeV}^2$.

Positrons travelling at low angles relative to the beam are deflected by the steering magnets through a window in the beam-pipe. There they hit the ET which is positioned very close to the beam-pipe. In contrast, the photons, moving collinearly with the positron beam, continue on a straight path leaving the beam-pipe and hitting the PD. The positron and photon are said to come from the same interaction if they are in coincidence when they hit the detectors. The layout of the luminosity system is shown in figure 3.6.

The ET and PD are Cerenkov calorimeters [50] which are made from arrays of crystals 20 cm ($\approx 22\,X_0$) long. The ET contains 49 crystals and has the dimensions $154 \times 154\,\mathrm{mm}^2$ while the PD is made of 25 crystals and is $100 \times 100\,\mathrm{mm}^2$. The energy resolution for these detectors is given by $\frac{\sigma_E}{E} \approx \frac{10\%}{\sqrt{E}} \oplus 1\%$ and they achieve a position measurement with an accuracy of 0.3-1.2 mm in the $x - y$ plane.

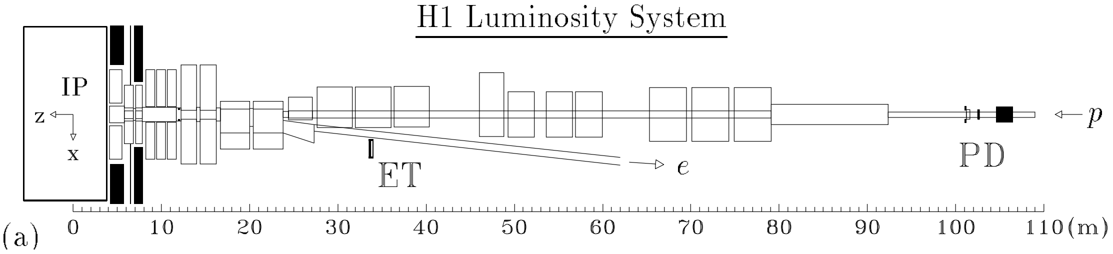

Figure 3.6: Diagram of the luminosity system

The main source of background for the luminosity measurement is Bremsstrahlung from the residual gas in the beam-pipe. This is expected to account for $\sim 10\%$ of the observed rate in the ET and PD. Other backgrounds like synchrotron radiation and proton beam-halo are minimised by the detector design. The PD is protected from proton beam-halo coming from behind by a 2 m ($2\,X_0$) block of lead and by a lead filter ($2\,X_0$) and there is a water Cerenkov counter in front which protects the detector from synchrotron radiation. The water Cerenkov also acts as a veto on out of time photon showers, some of which are due to the Bremsstrahlung background. The remaining backgrounds are estimated using the electron pilot bunches. Another factor important to the measurement of the luminosity is the acceptance of the two detectors which is very sensitive to the crossing angle of the positron and proton beams.

A relative luminosity measurement which can be produced on-line can be achieved with an accuracy of $\sim$2%. However, off-line, a more accurate calculation of the absolute luminosity is produced for analysis. This takes into account the contributions from proton satellite bunches, energy leakage from the detectors and the statistical subtraction of background so that there is an experimental error of $\sim 1.1\,\%$ [58] on the measurement.

3.6 Other Scintillators

The Proton Remnant Tagger

The Proton Remnant Tagger (PRT) is located in the very forward direction, at $z = 26\,\mathrm{m}$. It covers the area around and between the beam-pipes in order to detect low angled particles from the proton remnant. Is made up of seven sections made of double-layers of scintillator [50] and each is connected to its own readout channel. A channel only registers a signal if both layers have 'fired' and if this activity is timed to have come from an *ep* collision.

The Veto Walls

These double layered scintillating walls are used along with the ToF measurements in the SpaCal to reduce proton beam induced backgrounds. They are located between the incoming proton beam and the interaction point at $z = -6.5\,\mathrm{m}$ and $z = -8.1\,\mathrm{m}$. The first covers an area of $1\,\mathrm{m}$ around the beam-pipe and has a time resolution of $\sim 3\,\mathrm{ns}$; the second extends out to the radius of the LAr Calorimeter and has the poorer time resolution of $\sim 8\,\mathrm{ns}$. This information is sent along with the ToF measurements and vertex recognition decisions to the level 1 trigger (see section 3.7).

3.7 Triggering and Reconstruction

The number of background interactions at HERA far outweighs *ep* collisions. Further, it takes ~ 24 bunch crossings for the trigger to make a decision as to whether an *ep* collision has occurred during a bunch crossing. To avoid the otherwise inevitable dead-times of 95% (i.e. that the detector is inactive for 95% of the time), H1 uses a pipe-lined, multi-level trigger system. There are 5 levels to the system, though only levels 1, 4 and 5 were used during 1995.

After each bunch crossing, information from 9 trigger systems, which are associated with the main components of the detector, is sent to to the central trigger. This information is stored temporarily until the central trigger has had time ($\approx 2.5\,\mu$s) to process it and send an 'L1Keep' signal to the sub-detectors. Meanwhile, other bunch crossings are being analysed and stored in the pipe-line memory. Since it takes 24 bunch crossings for the L1keep signal to be sent, information from at least the last 24 bunch crossings has to be stored in this temporary memory at any one time. It also means that all the trigger information from a bunch crossing must be synchronised because the detector components are processing many events at a time.

The central trigger takes 1-2 bunch crossings to combine all the trigger information from the subsystems and compare it to predefined subtriggers. The L1keep signal is simply the logical OR of these definitions. Some of the subtriggers are used to select physics samples, others are used to monitor backgrounds and the subtrigger elements which are based on information from the sub-detectors. Prescales are applied if the rates of particular subtriggers are too high. This entails only accepting a fraction of events that satisfy the subtrigger definitions to limit the number of events being accepted. The general principle is that the prescales of physics subtriggers are kept as low as possible, while high prescales are applied to those designed for monitoring. The level 1 (L1) trigger, due to the pipe-line system, is dead-time free.

If the central trigger sends out a positive L1keep signal the event is deemed 'interesting' and the data taking stops so that all the 270 000 electronic channels at H1 can be read out. Part of the output is more detailed trigger information which can be used to further select events. Level 2 and level 3 of the triggering system can produce decisions to abort or continue the readout process, based on more complicated analysis of the L1 information, in $20\,\mu$s and $800\,\mu$s respectively. However, these levels are not active at present. The total readout process takes 1-2 ms during which H1 remains inactive. All the information from the detector for the read out events is stored temporarily and fed into level 4 (L4).

The design rate of the acquisition system was set at 50 Hz in order to maintain low dead-times. This then sets a challenge in the definition of the physics subtriggers, which need to select events from a background rate of ~ 10 kHz. On average the system runs at a rate of 30-40 Hz with a dead-time of 10-15% [59].

Semi-permanent logging of an event only occurs if it passes the L4 criteria. A simple reconstruction of the event is done on-line by fast parallel processors, and on the basis of this a L4 decision is taken. This should not affect data taking since the information is stored separately. At this stage most of the remaining background is removed as well as events which passed at L1 due to trigger noise. About 1% of these events are retained deliberately to study the L4 selection cuts. Apart from these about 30% of the L1 events are kept by L4 and this amounts to an output rate of 5-10 Hz.

The events surviving this stage are stored on disk until they can be fully reconstructed off-line by the program H1REC and are subsequently stored permanently on Production Output Tapes (POT). At a later time level 5 (L5) is implemented. This reduces the data further and organises it into a convenient format for analysis, the output of which is stored on Data Summary Tapes (DST). A discussion of L5, with regards to this analysis, follows in section 4.2.1.

Chapter 4

Event Selection

4.1 Introduction

In chapter 2 the possible production mechanisms for the elastic photoproduction of J/ψ mesons were discussed and these give strong predictions on how the cross section, $\sigma(ep \longrightarrow eJ/\psi\, p)$, is expected to rise as a function of $W_{\gamma p}$. The following two chapters present a measurement of this cross section made using data taken in 1995 and using the decay channel $\mathrm{J}/\psi \longrightarrow \mu^+\mu^-$. In order to study the dependence of the cross section on $W_{\gamma p}$, it is evaluated in four bins which cover the range $30\,\mathrm{GeV} < W_{\gamma p} < 150\,\mathrm{GeV}$. In each bin the cross section is defined as the number of events that are produced per unit of integrated luminosity, therefore, the selection of a clean sample of J/ψ events from the data is an essential part of its evaluation. However, this sample does not take into account the various inefficiencies of the H1 experiment and, therefore, has to be combined with the overall likelihood (acceptance) of an event being triggered, reconstructed and selected for the data sample. This acceptance is determined from Monte-Carlo (MC) event files where the response of the H1 detector has been simulated and the output processed by the same L5 selection as used for the data.

As described in section 3.7, the raw data is compressed and organised into a convenient form for physics analysis at L5 of the triggering and reconstruction chain. It is at this stage that the events are classified for specific analysis types. For this measurement the class CSEMU was used which is designed to select those events which, with the information available at L5, look like the decay $\mathrm{J}/\psi \longrightarrow \mu^+\mu^-$, or an open charm event where there is a leptonic final state. The classification criteria of this event class are more fully detailed in section 4.2. The remainder of this chapter is left to describe the selection of a clean sample of J/ψ candidates from this event class.

The possible decay modes of the J/ψ meson are shown in table 4.1, which indicates that the majority of the time a J/ψ will decay into one of a multitude of possible hadronic states. The types of these hadrons are restricted, by the conservation of energy, to those which contain only the lighter (u,d,s) quarks. More importantly for this analysis, however, is the muonic channel which has a clean and distinctive signature and which, at high luminosities, provides a significant sample of events. At H1 an elastic J/ψ event can be easily recognised in this decay mode in that only the two final state muons are expected to be seen in the main section of the detector. Constructing an invariant mass spectrum of all such muon pairs leads to a clear resonance at the J/ψ mass. The scattered positron and the proton of the event are generally lost down the beam-pipe or else leave energy deposits at low angles to their incident direction. This lack of information about the positron means that it is hard to reconstruct the kinematic quantities associated with the event and this question is addressed in section 4.3.

Decay Channel	Branching Ratio(%)
$J/\psi \longrightarrow$ hadrons	87.7 ± 0.5
$J/\psi \longrightarrow e^+e^-$	6.02 ± 0.19
J/$\psi \longrightarrow \mu^+\mu^-$	6.01 ± 0.19

Table 4.1: Various decay channels of the J/ψ and their branching ratios. Values are taken from [34].

It is clear now that the successful selection of J/ψ candidates from the data depends largely on how well the muon pair from its decay can be reconstructed. This involves understanding the subtriggers designed to identify these events, the tracking of high momentum, charged tracks and the identification of muons in the LAr calorimeter and the instrumented iron. These areas are addressed in sections 4.5, 4.6 and 4.7 respectively. The generation and simulation of the MC event files is introduced in section 4.4. These are used to predict how many of the events produced in real interactions will actually be recorded in the data. This estimation can only be meaningful if the MC can be shown to model the real data well. To this end, individual efficiencies for the trigger elements, the track reconstruction and the muon identification are calculated separately from both MC and the redundancy of information in the data to ensure that there is consistency between the two. The MC needs to be tuned to account for any discrepancies and a systematic error is applied to the acceptance calculation to reflect the uncertainty on these checks.

Finally the extraction of a sample of J/ψ candidates is described in section 4.8. The control plots and the kinematic acceptance for these events are shown along with a discussion of the possible background contributions.

4.2 The Data Sample

4.2.1 Level 5 Classification

CSEMU is one out of a total of 31 physics classes and is designed specifically to contain events which satisfy at least one of the following criteria:

- one muon identified in the FMD or the iron.
- at least two muons identified in the FMD, LAr calorimeter or the iron.
- one muon identified as above and one electron.
- one muon and no more than 5 tracks.
- one muon or electron and exactly two tracks.

The tracks can be located in either the forward or central tracking detectors or, where the particle passes through both, the hits in both regions can be fitted by a single combined track. These forward, central or combined tracks have to be considered sufficiently well reconstructed and must originate from near the interaction region before the event can pass the CSEMU classification. The cuts that have to be satisfied for each type of track are listed in table 4.2, where p is the momentum of the track, z_0 is the the coordinate of the track extrapolated back to the z-axis and |DCA| is the distance of closest approach of the track to the nominal vertex measured radially from the z axis. The χ^2 variables refer to the quality of the track's fit to the vertex and to the fit of the track to the hits in the chambers. The starting radius and the radial length of the track are termed r_{start} and r_{length} respectively and lastly, n_{hit} refers to the number of measured points used to reconstruct the track.

Muons in an event are identified using any combination of the the LAr calorimeter, the FMD and the instrumented iron. In the calorimeter the muons leave characteristic clusters, whereas in the latter detectors tracks have to be reconstructed from

Parameter	Central	Combined	Forward
p	≥ 0.8 GeV	≥ 0.8 GeV	≥ 0.8 GeV
$\lvert\mathrm{DCA}\rvert$	≤ 2 cm	≤ 2 cm	≤ 2 cm
$\lvert\mathrm{z}_0\rvert$	< 40 cm	< 50 cm	< 50 cm
χ^2_{vertex}	< 20	< 20	< 20
χ^2_{track}	-	< 10	-
r_{start}	< 30 cm	-	-
r_{length}	> 15 cm	-	-
n_{hit}	≥ 10	≥ 12	≥ 12

Table 4.2: Inner track cuts for the CSEMU event class. The explanations of the parameters are in the text.

drift chambers and streamer tubes. The quality of these outer tracks have to satisfy the criteria listed in table 4.3. The ρ variables give the largest allowable difference in the vertex along the x and y axes calculated from the inner and outer track. L_{start} and n_{layer} define the first layer and the minimum number of hit layers necessary to reconstruct a good track in the iron, while $\Delta\,\phi$ is the difference in angle between the portion of the track reconstructed in the pre-toroid layers and the portion in post-toroid layers of the FMD. If the clusters or outer tracks are of sufficient quality the classification code tries to establish links between these and the accepted tracks from the inner region. The quality of this link is categorised by good=3, medium=2 and poor=1 for the calorimeter and by a χ^2 probability for the FMD and the iron. To satisfy the CSEMU cuts a muon would have to have a cluster quality 2 or 3, or a link probability larger than 0.01% in the FMD or the Iron. At this stage the link is accepted providing the inner track has momentum between 0.8 GeV and 20 GeV.

Parameter	FEC	Barrel	BEC	FMD
ρ_x	≤ 100 cm	≤ 100 cm	≤ 100 cm	-
ρ_y	≤ 100 cm	≤ 100 cm	≤ 100 cm	-
$\lvert\mathrm{z}_0\rvert$	-	≤ 100 cm	-	$^{+300}_{-400}$ cm
L_{start}	≤ 5	≤ 5	≤ 8	-
n_{layer}	≥ 6	≥ 2	≥ 3	≥ 4
χ^2_{track}	-	-	-	≤ 20
$\Delta\,\phi$	-	-	-	< 1 rad

Table 4.3: Outer track cuts at L5 for the instrumented iron (forward endcap, barrel and backward endcap) and the FMD. The explanations of the parameters are in the text.

4.2.2 Luminosity

The data used for this analysis was taken over the 1995 running period when HERA was colliding positrons of 27.5 GeV on 820 GeV protons. Of this data, only the 'good' and 'medium' runs, where the essential sub-detectors[1] and parts of the readout[2] were working, are used. With these restrictions the integrated luminosity, corrected for satellite contributions, is $\int \mathcal{L}\, dt = 4893\,\mathrm{nb}^{-1}$.

4.3 The Event Kinematics

In a photoproduction event the incoming positron emits an almost real photon which then interacts with the proton. In this case the positron is scattered through a small angle and at H1 is either lost down the beam-pipe or identified in the electron tagger. For this analysis any event where a scattered positron is identified in the SpaCal or LAr calorimeter is rejected. To reconstruct the kinematical variables y and Q^2, using the general DIS kinematics stated in equations 2.8 and 2.7, it is necessary to know the energy and scattering angle of the positron. As explained, however, this information is not known for photoproduction events at H1. This problem is overcome by using a method first suggested by Jaquet and Blondel [60] which reconstructs y using event variables which can be directly measured. In this case:

$$y_{JB} = \sum \frac{E - p_z}{2E_e}, \tag{4.1}$$

where E and p_z are the energy and the z-component of the momentum of a particle in the event and E_e is the positron beam energy. The summation includes all the particles in the event apart from the scattered positron. The variables Q^2 and $W_{\gamma p}$ can then be written in terms of y_{JB} so that,

$$Q^2 = \frac{\left(\sum p_x\right)^2 + \left(\sum p_y\right)^2}{1 - y_{JB}} \tag{4.2}$$

---

[1] Essential sub-detectors: central and forward Trackers, the LAr calorimeter, the forward muon detector, the SPACAL, the instrumented iron, the time of flight scintillators, the veto counters, the luminosity system, the plug calorimeter and the proton remnant tagger.

[2] Essential readout branches: the central trigger, the LAr trigger, the Calorimeter ADC and SPACAL, the forward and central trackers, the forward muon detector, the instrumented iron, the BDC, the luminosity system/forward muon trigger/FPS and the R-ϕ and R-z triggers.

$$W_{\gamma p}^2 \simeq 4 E_e E_p \, y_{JB}, \tag{4.3}$$

where the summations, like before, are over all the particles in the event apart from the scattered positron. The proton beam energy is represented by E_p and p_x and p_y are the x and y components of a particle's momentum. Figure 4.1 shows how well this technique reconstructs the y and the $W_{\gamma p}$ of a MC diffractive J/ψ event. In contrast Q^2 can only be poorly reconstructed due to the limited resolution on measuring a particle's transverse momentum. For this reason no cut is made explicitly on the reconstructed Q^2 of the event, however, by insisting that the scattered positron is not seen in the main detector a limit on Q^2 is indirectly imposed so that $Q^2 < 1.2\,\mathrm{GeV}^2$.

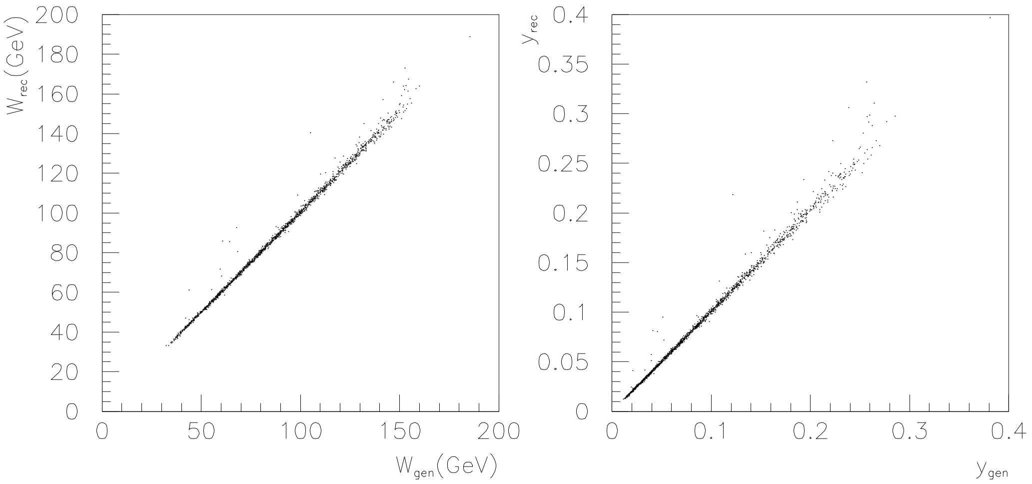

Figure 4.1: Plots showing reconstructed versus generated values for the $W_{\gamma p}$ (left) and y_{JB} (right) of MC diffractive J/ψ events.

The Jaquet-Blondel method can also be used to reconstruct the elasticity variable, z, defined by equation 2.20. The reconstructed quantity is obtained from:

$$z_{rec} = \frac{(E - p_z)_{J/\psi}}{2 \, y_{JB} \, E_e}, \tag{4.4}$$

where $(E - p_z)_{J/\psi}$ is the energy minus the longitudinal momentum of the combined J/ψ object. The generated and reconstructed values of z for the same MC J/ψ events are shown in figure 4.2. From here it can be seen that the spread of the z_{rec} distribution is larger than that of the z_{gen} distribution. This tail into lower values of z is due to the poor resolution on the energy measurement of the proton remnant. However, as with the Q^2 variable, no explicit cut is made on the reconstructed variable instead it is limited to values of $z_{rec} \gtrsim 0.95$ by the requirement that only 2 inner tracks are seen in the event. This restricts the sample to the 'quasi-elastic' domain, mentioned in section 2.4.2, in that it can only include purely elastic events, where z=1, or proton-dissociative events where z is close to 1. Estimating the relative size of the elastic and proton-dissociative contributions is considered in the next chapter.

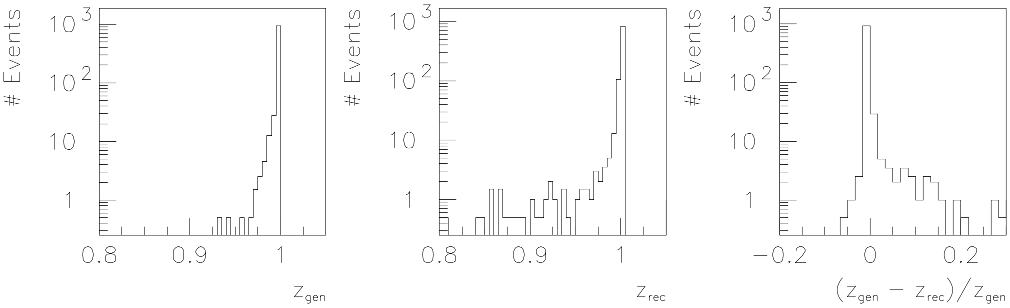

Figure 4.2: Plots showing the generated (left) and the reconstructed (middle) values of the variable z for a MC diffractive J/ψ event. The remaining plot (right) shows the resolution of the reconstruction.

Another useful variable used in this analysis is η_{min} which represents the pseudorapidity of the most backward energy deposit, other than the two decay muons, measured in the LAr calorimeter. It is defined by the equation:

$$\eta_{min} = -\frac{1}{2} \ln \tan \left(\frac{\theta}{2} \right) , \tag{4.5}$$

where θ denotes the polar angle of the most backward energy cluster of greater than 300 MeV. This variable is useful for further restricting the elasticity variable, z, without making explicit cuts.

4.4 Monte-Carlo Simulation

DIFFVM [61] is a Monte-Carlo generator of diffractive processes. The model used regards the photon as a hadronic state which fluctuates into a virtual vector meson and scatters off the proton. The coupling of the photon is described by VMD and the elastic scattering is modelled using the Regge theory of soft hadronic interactions, where the colourless exchange is made by the phenomenological pomeron. This treatment of diffraction is described in detail in chapter 2. It is used at HERA to describe the elastic photoproduction of the light vector mesons ρ, ω and ϕ as well as the heavier charmonium states of J/ψ and ψ'. Elastic, in this context, is defined as events whose elasticity is close to 1 and this model is assumed to be only applicable when $z > 0.9$. Above this, the parameters of the generator allow events from both the truly elastic and the proton-dissociative processes to be produced, which is essential for the isolation of these separate processes in the data sample.

Events are generated according to the following equations:

$$\sigma \propto W_{\gamma p}^{4\epsilon} \tag{4.6}$$

$$\frac{d\sigma}{dt} \propto e^{-bt} \tag{4.7}$$

where ϵ and b are fixed by experimental data from H1 [39]. The quantity ϵ describes the rise of the cross section as a function of $W_{\gamma p}$ and is set so that $\epsilon = 0.225$. The dependence of the cross section on the 4-momentum transfer, t, is modelled with the parameter b, which is considered to be a constant. For the elastic case $b = 4.0$ GeV $^{-2}$, whereas when the proton dissociates a shallower dependence is expected so that $b = 1.6$ GeV $^{-2}$. The cross section for proton-dissociative events is also a function of M_Y, the mass of the proton remnant. Events are generated such that:

$$\frac{d\sigma}{d\,M_Y^2} \propto \left(\frac{1}{M_Y^2}\right)^{\alpha_{I\!P}(0)} \tag{4.8}$$

where the pomeron intercept, $\alpha_{I\!P}(0) = 1.080$, is taken from proton-proton scattering measurements [42]. The decay angles of the muon pair are generated in accordance with those predicted by s-channel helicity conservation.

Event files of 20,000 events were produced for the elastic and proton-dissociative process, where the generated J/ψ decays to a muon pair. The detector response was then simulated using the program H1SIM whose output is identical to that of the real data which means it can then be processed with the same L5 code. The standard of the simulation is tuned by looking at the efficiencies of the subtriggers, the muon identification and the track reconstruction and, where necessary, re-weighting the MC to obtain better agreement with the data. For these efficiency studies a sample of half proton-dissociation and half elastic MC events were used in order to better reflect the data. It should also be noted that the z-vertex distribution simulated for the 1995 is shifted by approximately 5 cm relative to the data. In the same way the generated b parameters can be tuned to better match the t dependence shown by the data. The optimum values, found using a χ^2 fit (see chapter 6), are b=5.7 for the elastic version of the MC and b=0.5 for the proton-dissociation version. These factors have been corrected for in all the results shown in the following sections.

Event files were also generated for the elastic and proton-dissociative production of ψ' mesons where they decay directly or indirectly to muon pairs. This was required to estimate the ψ' contribution to the J/ψ data sample. The parameters ϵ, b and M_Y are the same as those applied to the J/ψ generation.

4.5 Trigger Selection

The purpose of the central trigger (see section 3.7) is to make rapid decisions at the time of an event as to whether it is worthy of more detailed reconstruction. The system is made up of 128 subtrigger definitions which are each designed to select a particular category of events. These definitions are a series of logic statements based on certain types of detector information which are known to be efficient at distinguishing interesting events from a multitude of possible backgrounds. These variables are known as trigger elements and for this analysis are based on information from the trackers and the instrumented iron.

Subtrigger	Definition
54	Topo_BR.AND.DCRPh_Tneg.AND.zVtx_Cls
18	Mu_ECQ.AND.zVtx_Cls.AND.Zvtx_Mu.AND.DCRPh_Thig
19	Mu_Bar.AND.Zvtx_Mu.AND.DCRPh_Thig.AND.DCRPh_Tneg

Table 4.4: The logical definitions of the L1 subtriggers used in this analysis.

Elastic J/ψ events are principally identified using subtrigger 54, which looks at the topology of the event, or by subtriggers 18 and 19 which fire on one of the muons from its decay. The definitions of these subtriggers are listed in table 4.4. What follows in the remainder of this section is a description of each of the trigger elements which make up these definitions and the calculation of their efficiencies in data and MC. The results are summarised in table 4.5. Determining these efficiencies in data, without introducing biases, requires a sample of events selected independently of the relevant trigger element. This is only possible in some cases because the events have been triggered by DIS and electron tagger (etag) subtriggers as well as the J/ψ subtriggers listed above. This problem does not apply in the case of the MC as the subtriggers are simulated after the event generation so as to match the distribution found in real data.

Element	Efficiency (%)	
	Data	MC
Topo_BR	56.1 ± 3.0	52.7 ± 3.2
Mu_Bar	83.3 ± 4.8	78.6 ± 4.4
Mu_FOEC	69.2 ± 9.0	69.2 ± 12.8
Mu_BEC	68.9 ± 3.6	54.2 ± 2.7
zVtx_Mu	94.4 ± 1.6	92.8 ± 0.4
zVtx_Cls	88.8 ± 2.2	91.5 ± 0.5
DCRph_tneg	85.5 ± 2.9	84.3 ± 1.3
DCRph_thig	88.5 ± 2.6	97.8 ± 0.5

Table 4.5: Summary of the efficiencies of the subtrigger elements measured from Data and MC.

4.5.1 The Topological Trigger Element

This trigger element utilises the quick position information from proportional chambers to decide whether there are only two big rays in the event and that these lie back to back in the r-ϕ plane. Here, a big ray is defined as a track which has been reconstructed from 4 pads in the CIP and COP (or FPC) which have fired in coincidence and which all lie in a single ϕ-sector. Further, rays are only considered by the Topo_BR trigger element if they point towards the nominal interaction point.

To study this trigger element a sample of two track events, where no scattered positron was visible in the detector, were selected. The track pairs had an invariant mass of between 2.8 and 3.4 GeV and at least one of them had been identified as a muon in the calorimeter or the instrumented iron. These events were considered to be independent of the Topo_BR trigger element provided they were selected by subtriggers 14, 16, 18, 19 or 22. Since this trigger element considers the topology of the event and not the individual tracks the efficiency is studied as a function of the momentum, θ and ϕ of the negative track. These are shown in figure 4.3 for the regions $p > 1\,\mathrm{GeV}$; $20° < \theta_{both\,tracks} < 160°$ and $35° < \theta_{negative\,track} < 150°$. The efficiency values measured from data and MC are listed in table 4.5 and these agree well within errors.

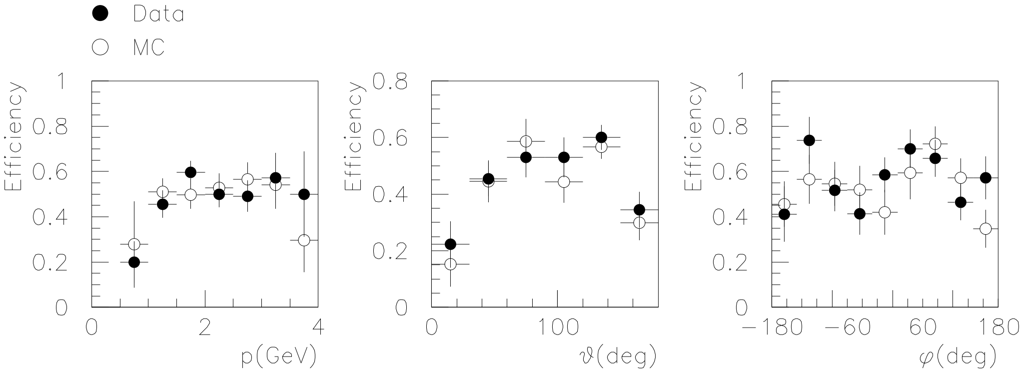

Figure 4.3: The efficiency of the Topo_BR trigger element as a function of momentum, θ and ϕ

4.5.2 The Muon Trigger Elements

Subtriggers 18 and 19 contain the elements Mu_ECQ and Mu_Bar which are based on information derived from the instrumented iron. Mu_Bar is designed to be active when a track is found in the barrel, which covers the angular region $35° < \theta < 125°$. Mu_ECQ, however, is expected to fire when a muon passes through the endcaps and is defined as the logical OR of two other elements, Mu_FOEC and Mu_BEC. For the former to fire, a track must pass through the outer part of the forward endcap, while the latter requires a track segment in any part of the backward endcap. In all cases the track must be made up of hits from at least 3 out of a possible 5 instrumented layers, which should have fired in coincidence and along a straight line.

Independent samples of two track events, where one track was identified as a muon in the instrumented iron, were selected to study these subtrigger elements. To ensure a reasonably pure sample of J/ψ events the invariant mass of the two tracks was restricted to the range $2.8 < M_{\mu^+\mu^-} < 3.4$ GeV and events were rejected where a scattered positron was found in the calorimeter or SpaCal. Finally, the following subtrigger selections were made for the samples:

Mu_Bar	St: 14, 16, 18, 22, 52, 54
Mu_FOEC	St: 19, 22, 52, 54
Mu_BEC	St: 14, 16, 19, 52, 54.

The efficiency of the Mu_Bar element is measured for tracks with transverse momentum $p_t > 1.5$ GeV and in the angular range $35° < \theta < 125°$. Similarly, the Mu_FOEC element was evaluated for tracks with $p > 1$ GeV and angles $20° < \theta < 35°$. The results, calculated using data and MC, agree well and are listed in table 4.5. The large errors on the efficiencies of these two elements simply reflect the poor statistics of the test sample. Finally, the efficiency of the Mu_BEC element was measured using tracks with $p > 1$ GeV and $125° < \theta < 172°$, however, here a 15% discrepancy between the values calculated from data and MC is found. This difference is not well understood but can be compensated for by a small re-weighting of the MC. This correction is included in figure 4.4 which shows graphically the efficiency of the muon trigger elements, Mu_Bar and Mu_ECQ, as a function of θ and momentum.

4.5.3 The Z-Vertex Trigger Elements

The z-vertex trigger is designed to filter out non-ep interactions using track information from the proportional chambers of the central and forward trackers. Any track which has been reconstructed from a pair of hits in the CIP and COP (or FPC), is extrapolated back to the z-axis and this position is entered into the z-vertex histogram for that event. The histogram consists of 16 bins each representing 5.4 cm along the z direction. The vertex position of the event is indicated by a peak or a grouping together of entries in the histogram, whereas spurious tracks in the event, due to other interactions or bad reconstruction, tend to give a flat background. The shape of the histogram depends largely on the type of event being detected, so that for an elastic J/ψ event, with its low multiplicities, no substantial peak is expected, but entries are expected to occupy adjacent bins.

As seen in table 4.4, the z-vertex elements used by this analysis are zVtx_Mu and zVtx_Cls both of which have to be further defined. The element zVtx_Mu is made up from the logical OR of zVtx_small and zVvtx_sig1, where the former is defined

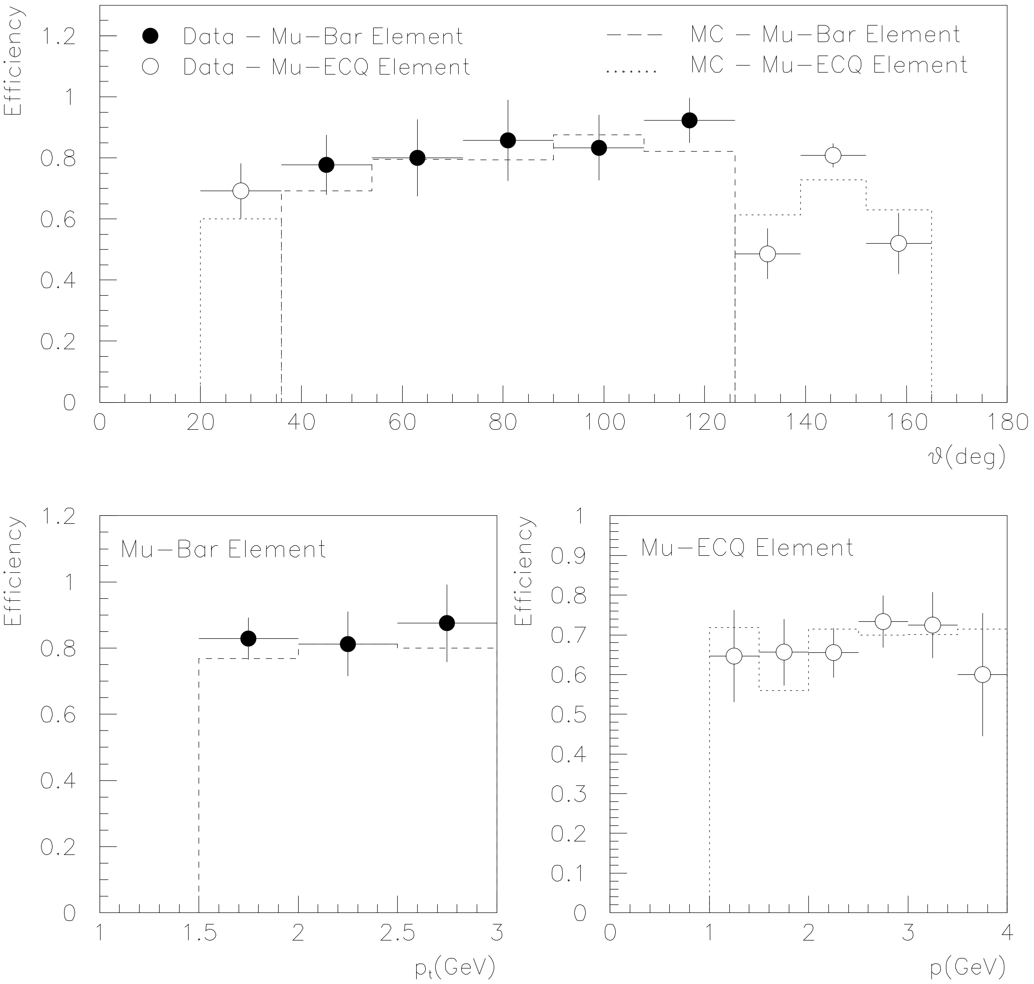

Figure 4.4: The efficiency of the Mu_Bar and Mu_ECQ trigger elements as a function of θ (top) and momentum (bottom). In the case of the backward endcap the MC has been re-weighted upwards by 15% so as to agree with Data.

as having no more than 6 entries in one bin and no more than 3 in any other; and the second is restricted by the requirement that one bin has at least 4 entries in it. The zVtx_Cls element demands that all entries in the histogram lie within 4 neighbouring bins. However, during some periods in 1995 it wasn't working and so the zVtx_small element, described above, was used to replace it. This is taken into account in the following efficiency studies.

Once again two track samples were used, where at least one of the tracks was identified as a muon. However, in this case a tighter invariant mass cut was applied of $2.95 < M_{\mu^+\mu^-} < 3.25$ GeV and tracks were restricted to the angular range of $20° < \theta < 160°$. The data sample was triggered using DIS (0-13) and etag (81-90) subtriggers which are all independent of any of the z-vertex elements or global options. No subtrigger selection was imposed on the MC sample. The results of the study are shown in figure 4.5 where the efficiencies of the two elements are plotted as functions of the transverse momentum of the J/ψ and the θ and ϕ of the negative muon in the event. The values measured from data and MC are found to be consistent with one another and are listed in table 4.5.

4.5.4 The Track Trigger Elements

The DCRph subtrigger elements, like those for the z-vertex, use information from the central jet chambers. The magnetic field in the CJC makes it possible to measure a track's momentum as well as to identify its charge so that this information can be used by the subtriggers to select specific event types. The DCRph_tneg element demands at least one negative track, while the DCRph_thig requires at least one track with a p_t larger than 800 MeV. This makes these elements highly suitable for the triggering of elastic J/ψ events where there should be two oppositely charged, high p_t, tracks from the decay to a muon pair.

The efficiency of these elements was studied using a two track sample where the tracks were oppositely charged and had a momentum, $p > 1$ GeV . At least one of the tracks was identified as a muon in the LAr calorimeter or the instrumented iron. The data sample was selected from the independent DIS and etag subtriggers and was compared to a MC sample where no subtrigger choice was made. The efficiencies in the data and MC were calculated for the range $40° < \theta < 140°$ and are listed in table 4.5. For DCRph_tneg element there is good agreement between the data and MC values, however there is a discrepancy of 9% for the DCRph_thig element. It is not clear what this difference is due to since all the relevant quantities of the event

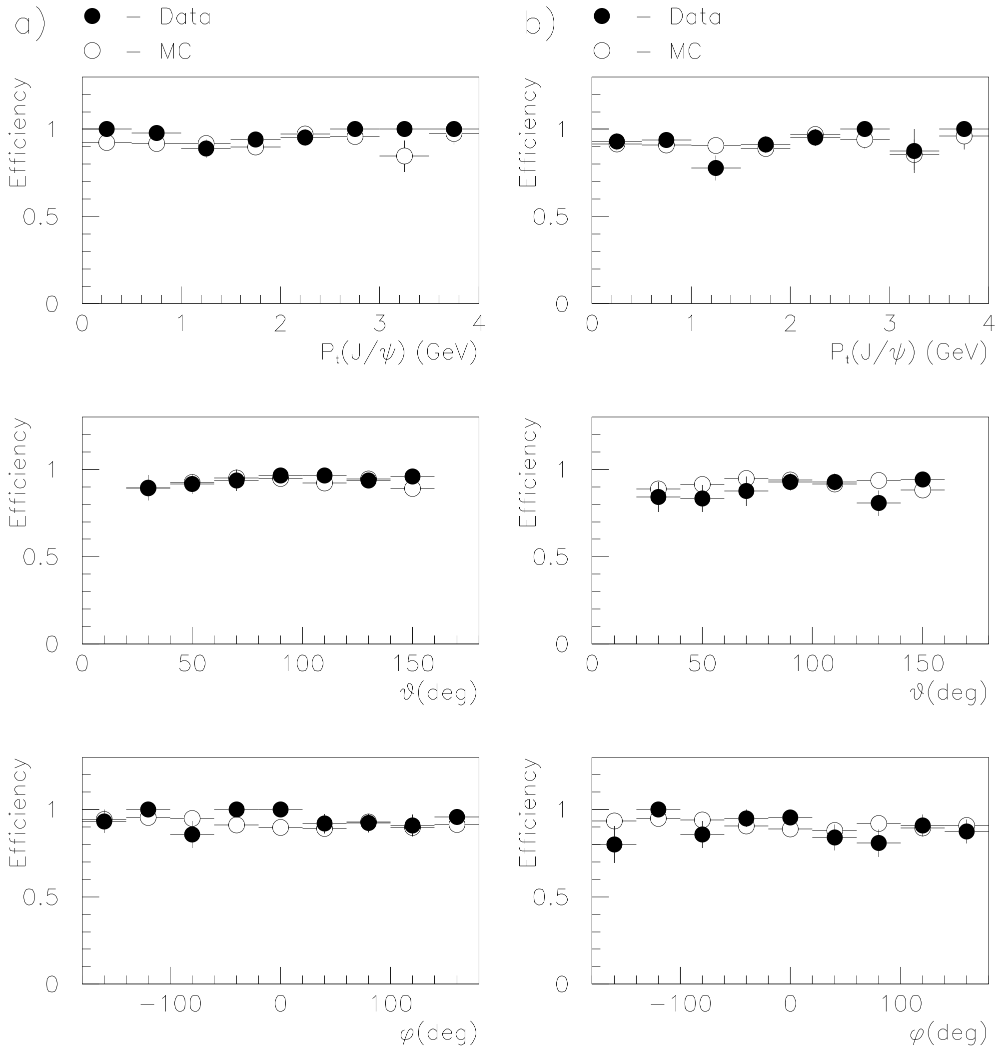

Figure 4.5: a) Shows the efficiency of the zVtx_Mu element as a function of the transverse momentum of the J/ψ (top), and the θ (middle) and ϕ (bottom) of the negative muon in the event. b) Shows the same plots for a combination of the zVtx_Cls element where it was working and its replacement, zVtx_Small, where it wasn't.

seem to be well matched in data and MC. The efficiencies of the DCRph elements are shown graphically in figure 4.6 where the necessary re-weighting of the MC has been included for the high p_t element.

4.6 Track Selection

Events in the physics classification class, CSEMU, can contain a host of tracks and track hypotheses of varying degrees of quality. The track cuts described in this section are designed to pick out the 'good' tracks from these and to reject those of poorer quality. All tracks selected for this analysis have to have a transverse momentum, $p_t > 150\,\mathrm{MeV}$.

Further sets of criteria are applied to tracks reconstructed in the forward and central trackers and to any combined track where a particle has passed through both. These are listed below:

Forward Tracks:

- $6^\circ < \theta < 25^\circ$
- $\mathrm{R}_0 < 10\,\mathrm{cm}$
- $\chi^2_{vertex\,fitted\,track} < 25$
- $\chi^2_{non-vertex\,fitted\,track} < 10$
- primary + secondary chamber segments ≥ 1
- planar + radial chamber segments ≥ 2

Central Tracks

- $20^\circ < \theta < 160^\circ$
- $|\mathrm{DCA}'| < 2\,\mathrm{cm}$
- $\mathrm{R}_{start} < 50\,\mathrm{cm}$
- track length $> 10\,\mathrm{cm}$ if $\theta < 150^\circ$
- track length $> 5\,\mathrm{cm}$ if $\theta > 150^\circ$

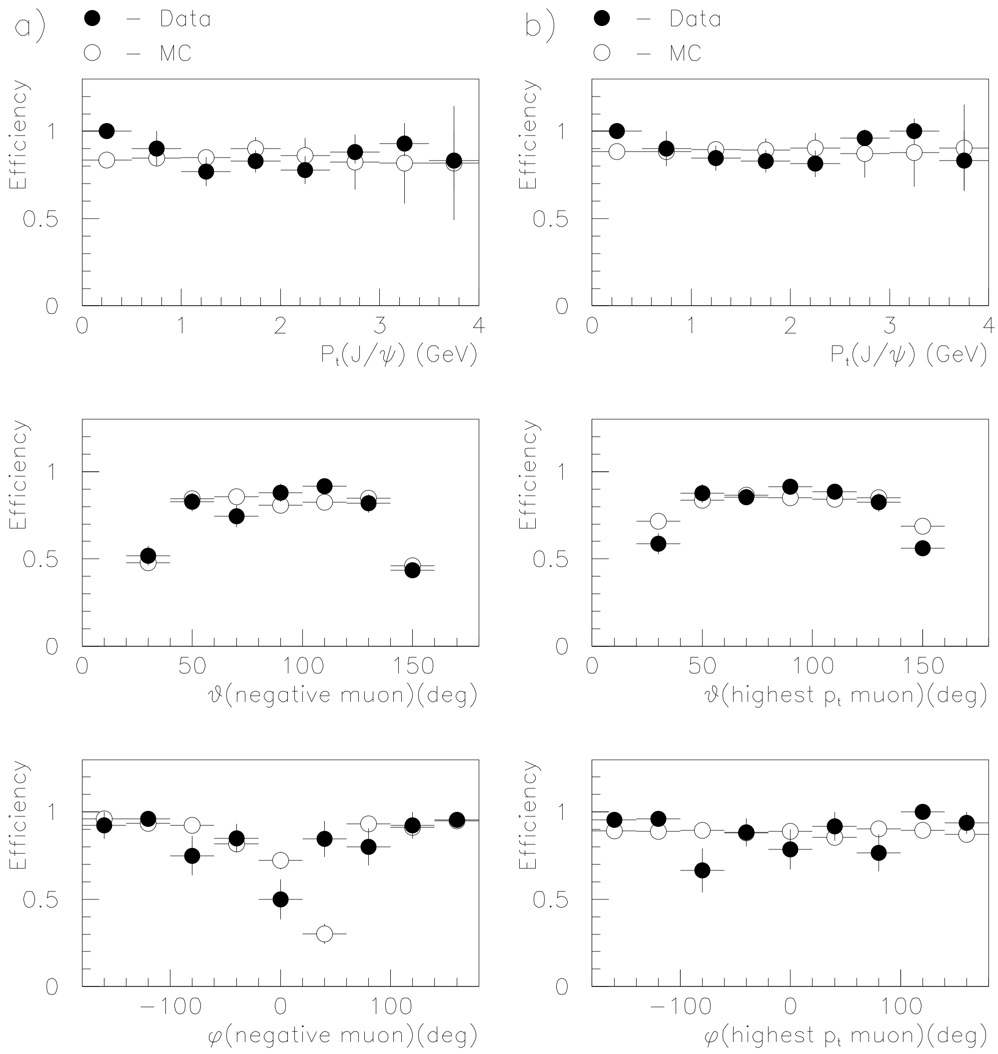

Figure 4.6: a) Shows the efficiency of the DCRph_tneg element as a function of the transverse momentum of the J/ψ (top), and the θ (middle) and ϕ (bottom) of the negative muon in the event. b) Shows the same plots for the DCRph_thig element, except that θ and ϕ are shown for the highest p_t muon and a 9% correction has been added to the MC.

Combined Tracks:

- $|\mathrm{DCA}'| < 5\,\mathrm{cm}$
- $\mathrm{R}_{start} < 50\,\mathrm{cm}$

The θ and p_t cuts restrict tracks to a region where the trackers are well understood and efficient so that they can be simulated accurately. The remaining conditions serve to ensure that the track quality is good and has not come from badly reconstructed hits in the chambers or from secondary or background interactions. R_0 is the radial distance in the xy plane from the vertex to the forward track and the χ^2 variables are a measure of how good the track fit is to the hits in the forward chambers and to the reconstructed vertex. In the central and combined regions, $|\mathrm{DCA}'|$ represents the distance of closest approach of the track to the reconstructed vertex and R_{start} is the radius at the innermost point of the track. Finally, the track length is the difference between the radii at each end of the track. Where more than one track hypothesis remains after these track cuts, the hypothesis with a primary reconstructed vertex takes priority over the others. If, however, the ambiguity is still unresolved then tracks are accepted in the order of combined, central and lastly forward segments.

The efficiency of track reconstruction in the angular range $20^\circ < \theta < 160^\circ$ is well studied and is found to be $97.5 \pm 2.0\%$ for data and $99.5 \pm 0.4\%$ for MC [62].

4.7 Muon Identification

The muons in this analysis are identified by linking a central track to either a cluster of quality 2 or 3 in the LAr calorimeter or a track with a link probability larger than 0.01% in the instrumented iron. The remainder of this section details the measurement of the linking and identification efficiency for these two systems. The LAr calorimeter and the iron are completely independent so that samples of muons identified by one can be used to study the efficiency of the other.

4.7.1 Liquid Argon Calorimeter

To study the efficiency of muon identification in the LAr calorimeter, a two track sample was selected where at least one of the tracks was identified as a muon in the instrumented iron with a link probability larger than 0.01%. The invariant mass of the two tracks was limited to $2.8 < M_{\mu^+\mu^-} < 3.4$ GeV so that they could be considered as muons from a J/ψ decay, despite only one of the muons having been identified. In this case, both tracks in the event can be used, doubling the muon sample and reducing the statistical error on the efficiency measurement. The subtriggers 18, 19, 22 and 54 were used to identify the sample since these are independent of any information derived from the LAr calorimeter.

Angular region θ	Efficiency (%)		Correction (%)
	Data	MC	
20°- 60°	58.7 ± 3.0	80.9 ± 3.3	22.2
60°- 120°	74.7 ± 3.3	85.4 ± 2.3	10.7
120°- 130°	50.0 ± 7.0	66.7 ± 4.5	16.7

Table 4.6: The identification and linking efficiency values for different angular regions of the LAr Calorimeter. The amount the MC needed to be corrected downwards by is shown in the final column.

For 1995 data the efficiency of muon identification calculated from MC is greater than that measured from data. The degree to which it differs varies over the angular range and these percentages are detailed in table 4.6 along with the efficiency values for tracks with $p > 1.5$ GeV .

The possibility that this discrepancy is due to there being a larger misidentification of pions as muons in data was considered by looking at events in the tails of the invariant mass distribution. Events in this region include lower mass muon pairs (see section 4.8.3) as well as any events with mis-identified particles. However, no significant misidentification, within errors, was seen. More likely is that the difference is due to the fact that the calorimeter noise is not correctly modelled in the MC simulation and that the identification and linking is sensitive to this. The efficiency of the muon identification in the LAr calorimeter, as a function of momentum, θ and ϕ, is shown in figure 4.7, where the MC has been re-weighted according to the correction values in table 4.6.

4.7.2 Instrumented Iron

A two track sample with an invariant mass of $2.8 < M_{\mu^+\mu^-} < 3.4$ GeV was selected to calculate the muon identification and linking efficiency in the iron. At least one

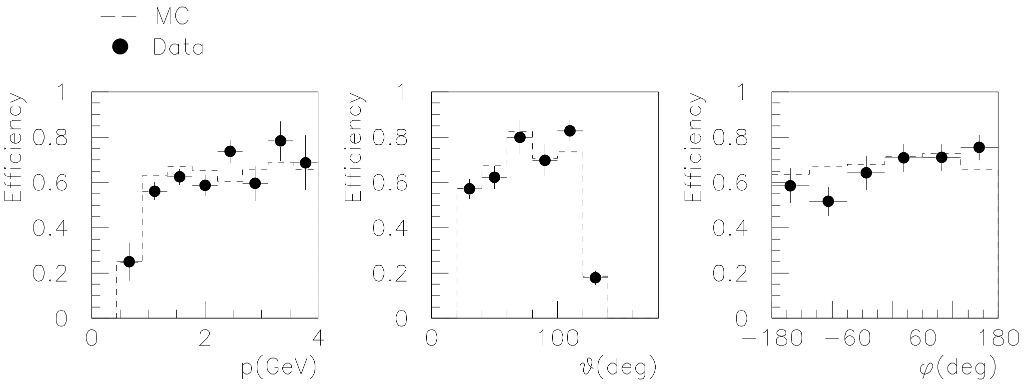

Figure 4.7: The efficiency of muon identification and linking in the LAr calorimeter shown as a function of momentum, θ and ϕ. The MC has been lowered by 10-20% (see text) so as to fit the data.

of the tracks in each event was identified as a muon in the LAr calorimeter with a quality index 2 or 3. A sufficiently large data sample of independent events can be acquired from subtrigger 54 plus the DIS (0-8) and etag (84-85) subtriggers, none of which use information from the iron. No subtrigger selection was applied to the MC, which meant that the transverse momentum and theta distributions of the tracks needed to be corrected before being used in the study. The resulting efficiency for data and MC is shown as a function of momentum, θ and ϕ in figure 4.8 and the calculated values, which agree within errors, are listed in table 4.7.

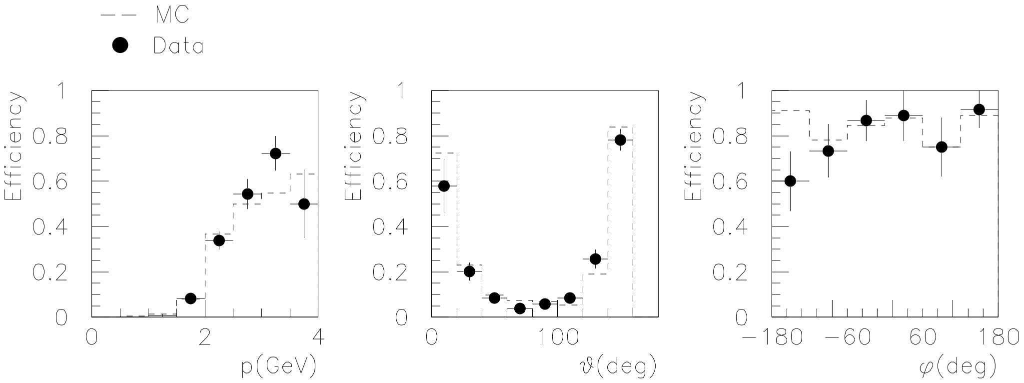

Figure 4.8: The efficiency for muon identification and linking in the instrumented iron shown as a function of momentum, θ and ϕ.

Angular region θ	Efficiency (%)	
	Data	MC
0°- 20°	57.9 ± 11.3	72.4 ± 5.8
20°- 140°	11.2 ± 1.1	11.1 ± 1.2
140°- 160°	78.2 ± 4.7	83.7 ± 3.9

Table 4.7: The identification and linking efficiency values for different angular regions of the instrumented iron.

4.8 The J/ψ Sample

4.8.1 The Two Track Selection

The two track sample is the pre-selection from which the J/ψ candidates are extracted. The sample was selected using criteria which have, in most part, been discussed in the previous sections of this chapter, and are now summarised here in the following list of cuts.

The Two Track Selection Criteria:

- Number of tracks = 2.
- Tracks should be oppositely charged.
- No cosmic tracks (see section 4.8.3).
- Both tracks identified as muons.
- $20^\circ < \theta_{both\,tracks} < 160^\circ$.
- No scattered positron in the LAr Calorimeter or SpaCal with an energy > 8 GeV .
- $-35 <$ reconstructed z-vertex < 35 cm.
- $\eta_{min} < 2.95$.
- Any one of subtriggers 18, 19 and 54 should have fired.
- $p_t(J/\psi)^2 < 1\,\mathrm{GeV}^2$

The angular distribution of the tracks is restricted to the central region of the detector where the behaviour of the inner trackers is well understood. It is also necessary to restrict the p_t^2 of the J/ψ to a region where the t dependence of the data is well defined. Beyond this range the MC can not be sufficiently tuned to provide reliable acceptances.

4.8.2 The J/ψ Candidates

The invariant mass distribution for the data events selected using the two track cuts is shown in figure 4.9, where a peak is clearly visible above a continuous background. The points can be fitted by a Gaussian plus straight line function and the number of J/ψ candidates obtained from the area under the peak. Using this method, the peak has a mean of 3.09 GeV, a width of 549 MeV and the area gives a sample of 294 J/ψ candidates.

Control plots of the important event quantities are shown in figure 4.10 for the J/ψ sample. These compare the MC variables with those from data to show that the simulation is sufficiently accurate. The data sample is taken from the peak of the invariant mass distribution and contains both the truly elastic and the proton dissociative process of J/ψ production. Therefore, a combination of MC events is used, where the ratio of the two processes is based on the final cross-section results detailed in the next chapter. The corrections arising from the efficiency studies have been included and the z-vertex and t distributions in the MC have been re-weighted as explained in section 4.4.

4.8.3 Backgrounds

There are three backgrounds which need to be considered when measuring the elastic J/ψ cross section. These are from cosmic muons, QED muon pair production and ψ' production. The events in the first category are cut out of the sample by the two track selection criteria; however, the second two need to be subtracted afterwards. The contribution from ψ' production is expected to be small, but its significance is enhanced due to the fact that it specifically affects the J/ψ peak. Determining the size of the ψ' contribution is achieved using MC samples and is discussed fully in the next chapter.

Cosmic ray muons are easily recognised because they pass through the detector in a

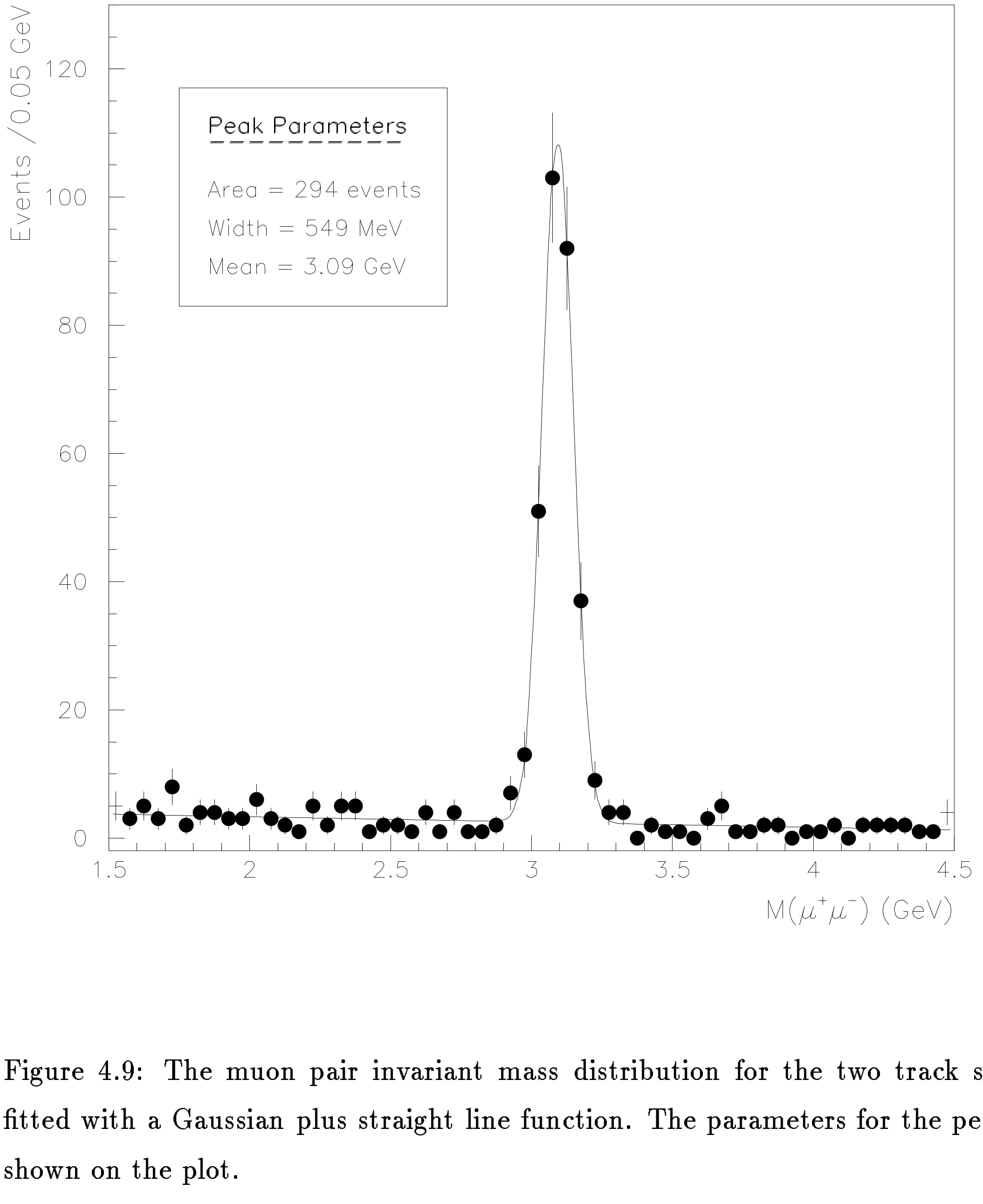

Figure 4.9: The muon pair invariant mass distribution for the two track sample fitted with a Gaussian plus straight line function. The parameters for the peak are shown on the plot.

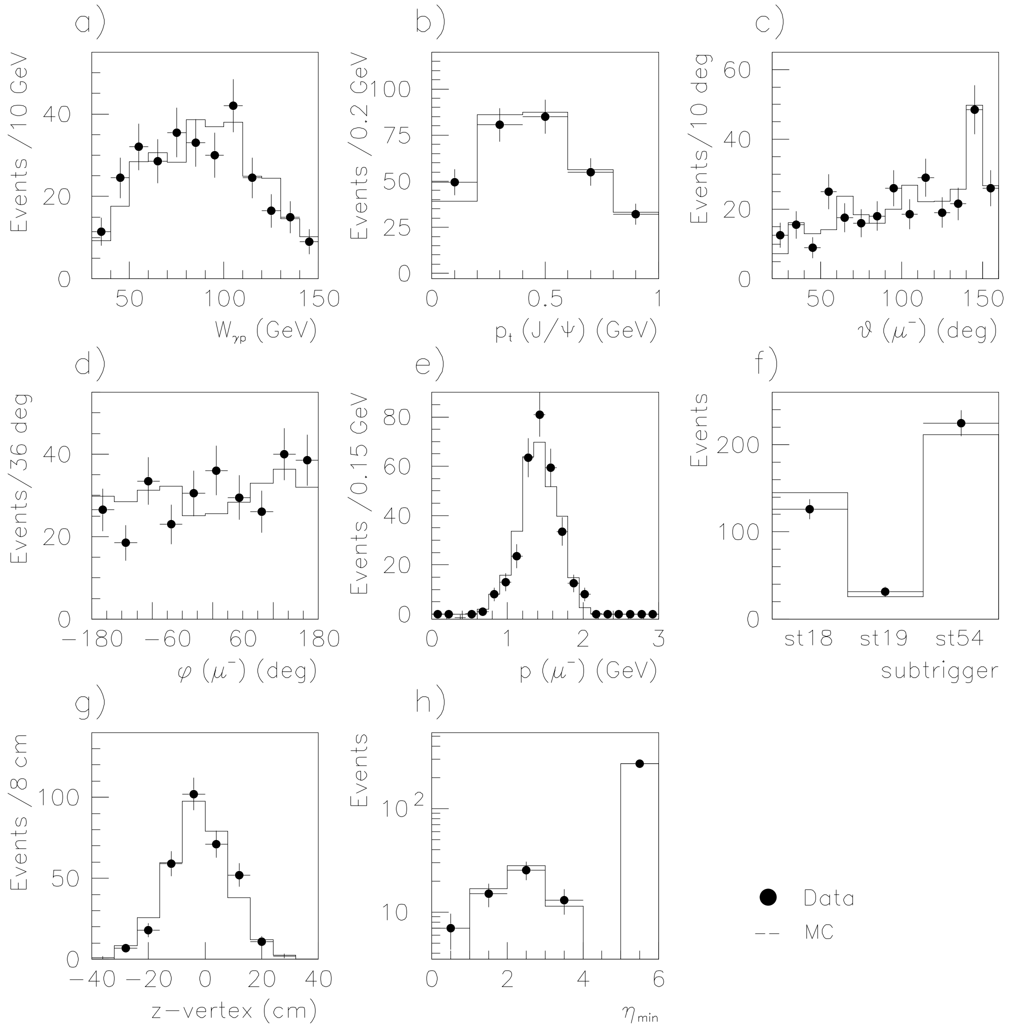

Figure 4.10: Control plots of the important event quantities for the J/ψ sample :

a) Centre-of-mass energy of the photon-proton system.

b) The transverse momentum of the J/ψ .

c) θ of the negative muon in the event.

d) ϕ of the negative muon in the event.

e) Momentum of the negative muon in the event.

f) Subtrigger distribution.

g) z-vertex distribution.

h) η_{min} distribution where the energy threshold is 300 MeV. Events with no energy deposit are binned at η_{min}=5.

straight line creating what looks like two tracks back to back in θ and ϕ. These are generally selected out of the data sample by a special subtrigger; however, where a ray passes close to the nominal vertex it can look like an *ep* event and is not rejected. These remaining events are are identified using position and momentum information from the CJC and then listed in the DCOS bank of the DSTs. Cosmic events are rejected by the two track selection by requiring that there is no entry in this bank. These rejected events do not specifically affect the J/ψ peak since their momenta are distributed over the whole invariant mass range.

The QED background is where photons from the incoming proton and positron fuse to create a muon pair. This process is well understood and is modelled by the LPAIR MC [63]. Again, these events do not specifically affect the peak of the invariant mass distribution, instead they create the continuous background beneath it. The straight line function fits this QED background well and makes it possible to subtract these events from the Gaussian peak.

4.8.4 Kinematic Acceptance

The overall acceptance of the two track sample is calculated using MC, where again a mixture of truly elastic and proton-dissociative events is used to reflect the contents of the data sample. The plots in figure 4.11 show this overall acceptance as a function of the kinematic quantities $W_{\gamma p}$, Q^2 and z. From these and the restriction on $p_t(J/\psi)^2$ in the two track selection, the kinematic range over which the cross section measurement is integrated is defined so that:

- $30 < W_{\gamma p} < 150$ GeV
- $z > 0.95$
- $Q^2 < 1.2\,\mathrm{GeV}^2$
- $p_t(J/\psi)^2 < 1\,\mathrm{GeV}^2$

The kinematic region that the cross section measurement covers is largely constrained by the two track selection cuts described in section 4.8.1. The relationship between the Q^2 and the scattered positron has been previously mentioned as has the restriction imposed on z by the two track requirement. What is new is how $W_{\gamma p}$ is dependent on the angular distribution of the muons in the event. The two

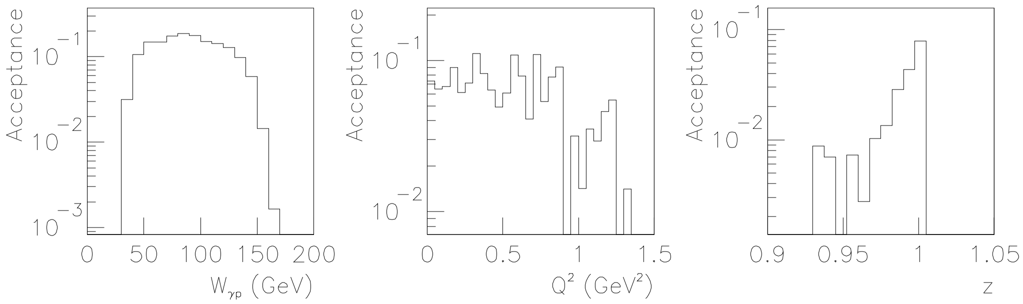

Figure 4.11: The overall acceptance calculated from MC as a function of $W_{\gamma p}$, Q^2 and z

track criteria make an angular cut on the central tracks of 20°< θ <160° and this restricts $W_{\gamma p}$ to the region stated above.

Chapter 5

Measurement of the Elastic J/ψ Cross Section

5.1 Introduction

The cross section, σ_{ep}, for any process occurring when positrons are incident on protons is defined by the equation,

$$\sigma_{ep} = \frac{N}{B\,\mathcal{L}}, \tag{5.1}$$

where N represents the number of data events of the process once the inefficiencies of the detector, the triggering and reconstruction and the selection are taken into account. This quantity is calculated from the data sample of J/ψ candidates described in section 4.8.1 and the acceptances for these events obtained from the elastic and proton-dissociation versions of the MC. In order to test the energy dependence of the J/ψ cross section N is evaluated in four bins of $W_{\gamma p}$. The remaining variables of equation 5.1 are the branching ratio of the decay channel which is denoted as B, and the integrated luminosity of the data $\mathcal{L}$. The branching ratio for the decay channel, J/ψ $\longrightarrow \mu^+\mu^-$, is well measured such that B=6.01%, while the integrated luminosity of the 1995 data sample is $\mathcal{L}$=4893 nb^{-1}.

A sample of 294 J/ψ candidates was extracted from the invariant mass peak in section 4.8.1. Apart from a small contribution from ψ' decays, these events are assumed to be diffractive J/ψ events due to the fact that they all contain only two muons and there are no other energy deposits backwards of 10°. These events can be divided, using information from the forward detectors, into two smaller samples for the separate elastic and proton-dissociative processes, where the forward detectors and the cuts applied to them are defined in section 5.2. The ψ' contribution to these two samples is estimated in section 5.4. The acceptances for the elastic and proton-dissociative processes are calculated using the two versions of the MC which model their different final states. The method and results of this calculation are detailed in section 5.5. However, while the forward detectors are capable of tagging the majority of proton-dissociative events there is still a significant fraction of these which elude the selection and end up contributing to the elastic sample. Likewise, a few true elastic events can be inappropriately tagged and enter the proton-dissociation sample. This migration of events is due to the inefficiency of the cuts applied to the proton remnant, the correction for which is discussed fully in section 5.6.

The ep cross section values can, at this stage, be calculated and these results are listed in table 5.6. What remains in the final sections is a discussion of the contributions to the systematic error and a description of how the ep values can be converted to the γp cross section.

5.2 Tagging the Proton Remnant

The data sample of J/ψ candidates includes both elastic and proton-dissociative events. These differ only in the behaviour of the outgoing proton which remains intact for the elastic case and breaks up into fragments with low transverse momenta in the dissociative case. Therefore, differentiating between the two processes involves studying the energy deposits in the forward direction. Elastic events, where $z{=}1$, should show no extra energy in this region since the intact proton passes straight down the beam-pipe unobserved. However, in the case where the proton dissociates the remnant is likely to deposit energy in the detectors close to the beam pipe. By using the information from the detectors in the forward region it is possible to tag a large proportion of these events making the separation of the elastic and proton-dissociative processes possible.

The term forward detectors is used to describe the combination of the first 10° of the LAr calorimeter; the FMD and the PRT. Their sensitivity to the proton remnant is mostly due to the detection of the secondary particles which originate from interactions between the remnant and the collimators or beam-pipe walls. Each subdetector has a threshold of sensitivity to the proton remnant which is dependent on its distance from the z-vertex of the event. The PRT has the lowest threshold, detecting the values of the remnant mass, $M_Y > 1.2$ GeV, while the FMD and LAr begin being active when M_Y is larger than about 1.3 GeV and 1.5 GeV respectively. This is displayed in figure 5.1 which shows the M_Y distributions for proton dissociative MC events which have been selected by the two track criteria and have activity in the forward region. Together the three detectors cover the pseudo-rapidity range, $1.74 < \eta < 8$, equivalent to an angular range of $0.06° \leq \theta \leq 20°$.

The PRT is made up of six scintillator layers, of which only the first three are used for this analysis to detect activity from the proton remnant. Energy deposited in one of the layers is called a 'hit'. In the same way, activity in the FMD is defined here as pairs of drift chamber hits in the pre-toroid layers. This is designed to reduce the effect of readout noise to acceptable levels. Lastly, in the forward region of the LAr calorimeter, clusters above an energy threshold are identified as being due to the break up of the proton. The selection applied to these forward detector quantities has to be able to distinguish between detector noise and the possibly low levels of activity expected from the proton remnant. In the case of the PRT the noise levels are known to be as small as 5×10^{-3} hits per event [64]. The energy threshold of clusters in the calorimeter is set at 300 MeV so as to be significantly higher than noise levels but low enough to identify the energy deposits from the proton remnant. However, even by selecting pairs of hits in the pre-toroid layers of the FMD there is still an appreciable amount of noise remaining and this is not simulated by the MC.

The size of the FMD noise signal was estimated using random trigger files. These are events that have been randomly selected from *ep* bunch crossings during the 1995 run period and recorded to tape. The distribution of the number of pre-toroid pairs is shown in figure 5.2 from which it can be seen that approximately 14% of events have a noise level of 1 pair. Therefore, this proportion of the elastic events, with one hit in the FMD, would be incorrectly labelled as proton-dissociative due to the readout noise. This can be accounted for by randomly applying a number of noise hits to the MC events according to this distribution and applying a discriminating cut on the combined noise plus generated FMD pairs quantity. This method avoids having to apply a higher cut on the number of FMD pairs, which would lower the detector's discriminating power. The correction is applied in figure 5.3, which shows the distributions of activity in the forward region for data and MC, where the latter consists of an elastic and proton-dissociation event mix determined by the final cross section values. The good agreement between data and MC ensures the reliability of the acceptance calculations for the elastic and proton-dissociative samples.

The cuts applied to the combination of forward detectors are termed the forward

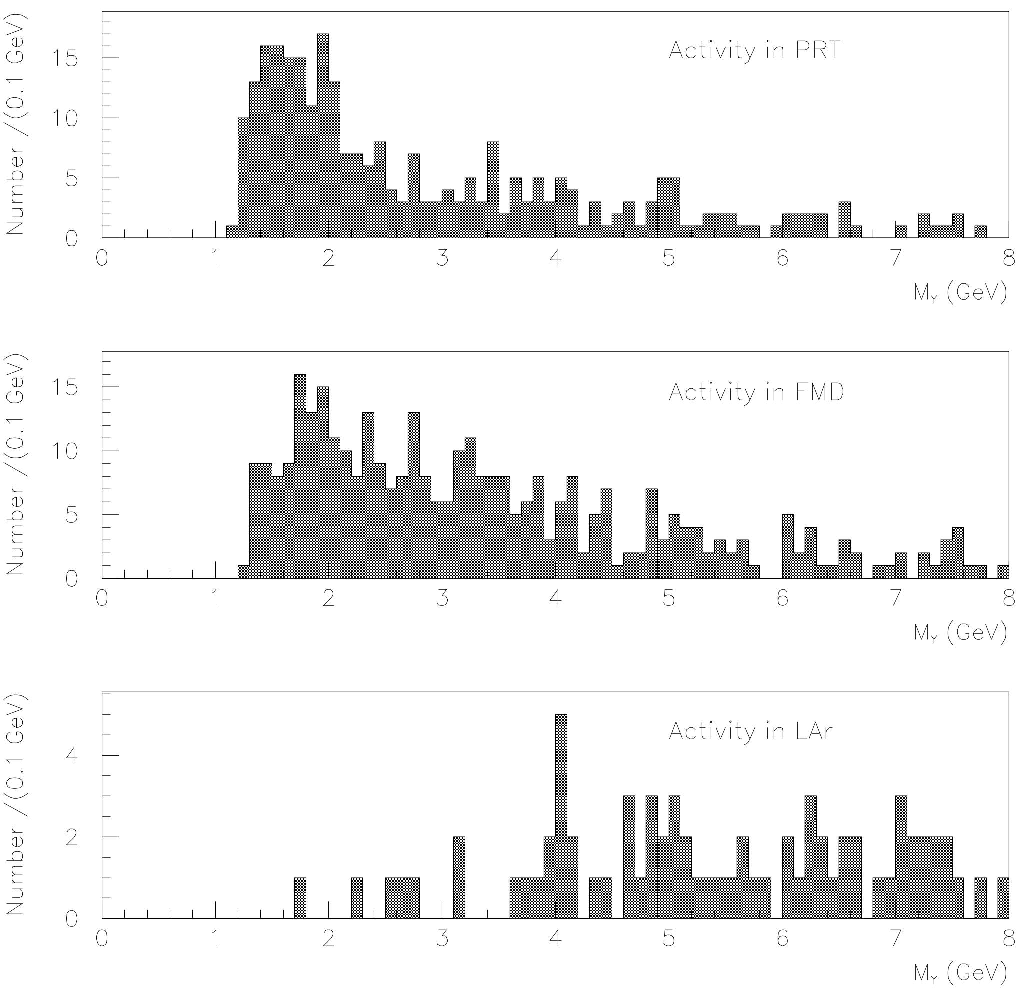

Figure 5.1: The mass of the proton remnant, M_Y, is shown for proton-dissociative MC events which have been selected by the two track criteria and have energy in the PRT (top), the FMD (middle) and the most forward 10° of the LAr (bottom).

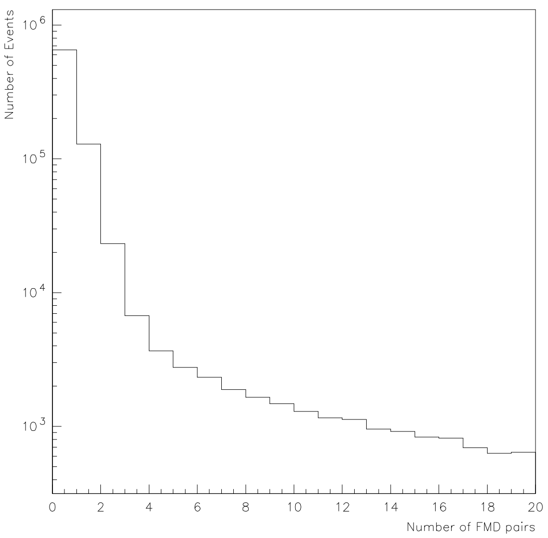

Figure 5.2: Distribution of the number of FMD pre-toroid pairs using 1995 random trigger data. The probability of an event having a number of extra FMD hits can be calculated from this plot and is used to apply a noise correction to the J/ψ MC.

cuts and these are listed below.

The Forward Cuts:

- The number of generated plus noise pairs of hits in the pre-toroid layers of the FMD < 2.
- The number of PRT hits $= 0$.
- No energy deposit >300 MeV in the region θ <10° of the LAr calorimeter ($\eta_{min} > 3.8$).

The use of MC events demonstrates that these cuts reject ~75% of proton-dissociative events from the sample of J/ψ candidates. The remaining quarter either leave no energy deposits or the remnant is not distinguishable from noise in the forward detectors. Likewise, ~10% of elastic events fail the cuts due to extra energy deposits left by detector noise or background processes. This migration of events between the elastic and proton-dissociation samples is estimated in section 5.6.

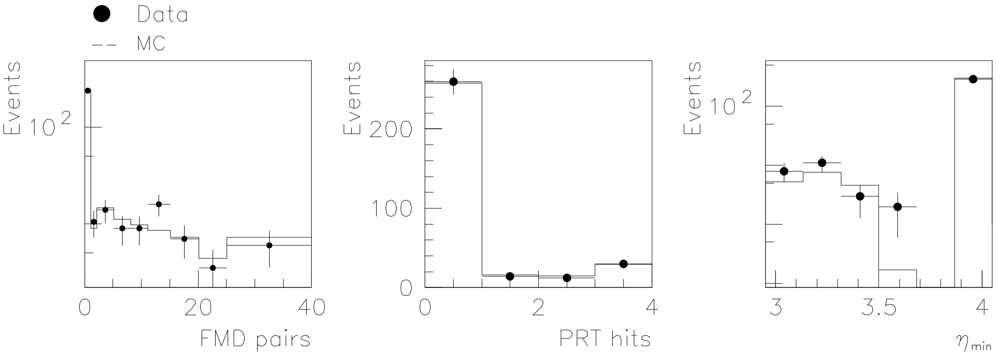

Figure 5.3: The activity in the FMD (left), the PRT (middle) and the the first 10°of the LAr calorimeter (right) due to the proton remnant is shown for data and MC. In the last plot events with no energy deposit are binned at η_{min}=4. A correction has been applied to the MC to account for FMD noise.

5.3 The Data Samples

The forward cuts are used to subdivide the J/ψ sample into two smaller samples. Those events that pass the cuts are predominantly attributed to the elastic process and hence these are called the elastic sample. However, there is still a number of proton-dissociative events that remain in this sample. Conversely, those events that fail the forward cuts originate mostly from the process where the proton fragments so these are referred to as the proton-dissociation sample. This contains a small number of elastic events. The migration of each process into the opposite sample is due to the inefficiency of the forward cuts and this is taken into account in section 5.6. A pictorial description of the separation of the elastic and proton-dissociative processes is shown in figure 5.4

The invariant mass is plotted for events in the two-track sample which pass and fail the forward cuts and each is fitted, as before (see section 4.8), with a Gaussian plus straight line function. The fits for both categories, in each of the four $W_{\gamma p}$ bins, are shown in figure 5.5. The size of the elastic and proton-dissociative samples, denoted N_{el} and N_{pd}, are extracted from the peak parameters with an uncertainty defined by the accuracy of the fit. These values are listed in table 5.4. Control plots, comparing data and MC for the important event quantities, are shown for the elastic and proton-dissociation samples in figures 5.6 and 5.7 respectively. A combination of elastic and proton-dissociative MC events is used, where the ratio of the two processes is based on the final cross section results. This takes into account the small migration of data events between the two samples. Corrections arising from the efficiency studies detailed in the previous chapter have been included and the z-vertex and t distributions have been re-weighted as explained in section 4.4.

Both of the elastic and proton-dissociative samples have small contributions from ψ' decays which it is necessary at this stage to estimate and subtract. This is discussed in the following section.

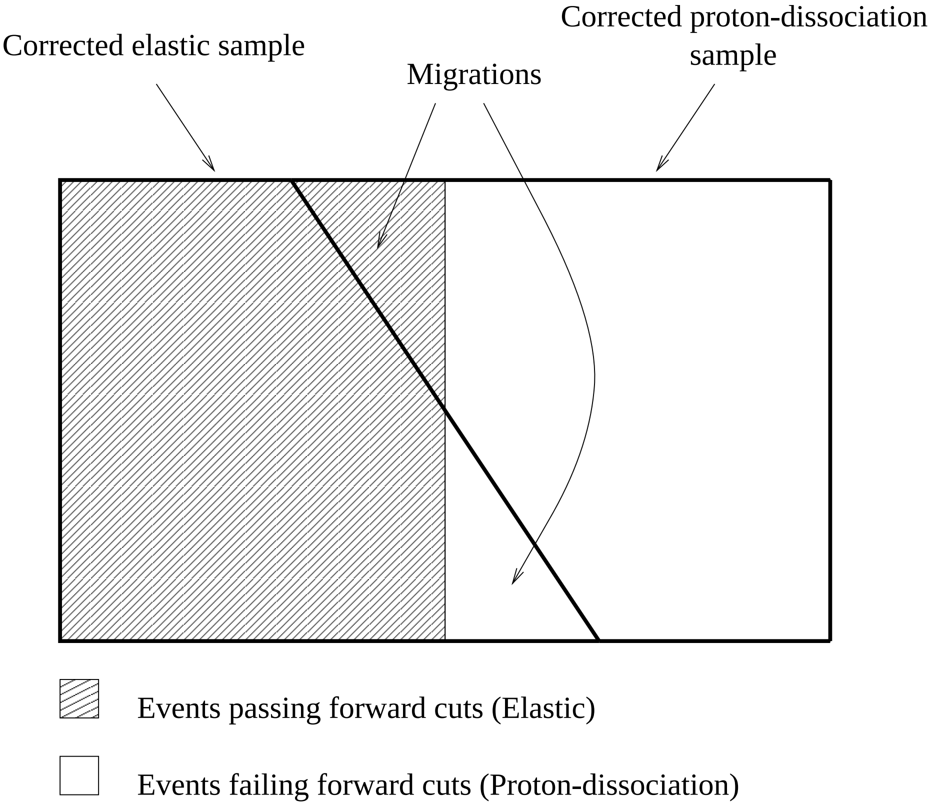

Figure 5.4: A pictorial representation of the separation of elastic and proton-dissociation events using the forward detectors. The migration of events between the elastic and proton-dissociation samples is due to the inefficiency of the forward cuts. This needs to be estimated separately using MC events.

5.4 ψ' Background

The relevant decay modes of the ψ' meson are listed in table 5.1 along with their branching ratios. Each of these contains a muon pair in the final state which makes

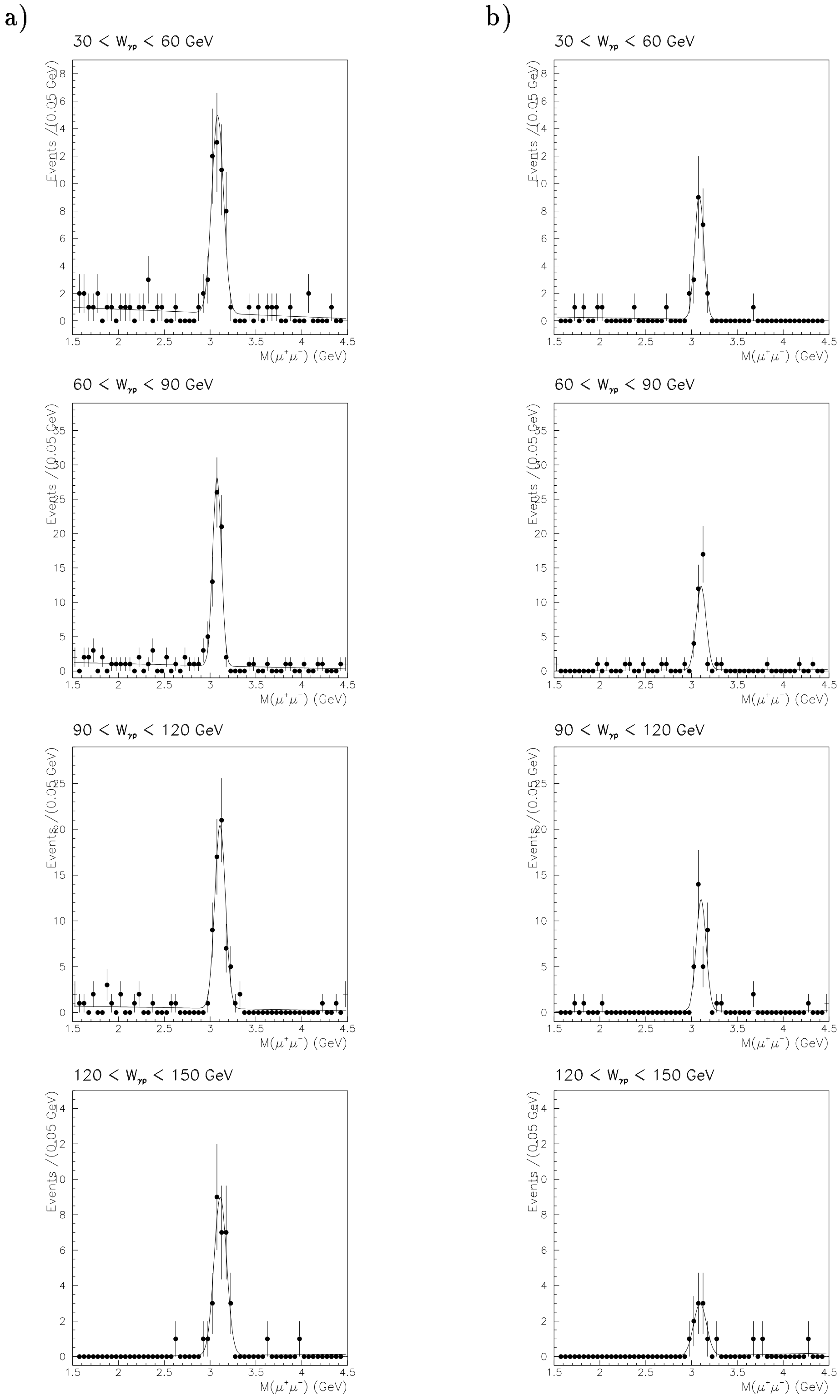

Figure 5.5: Data events that pass the two track criteria are split into two categories for each bin in $W_{\gamma p}$. a) shows those events that also pass the forward cuts and b) those that fail. The line shows the Gaussian plus straight line fit to the points. The number of elastic and proton-dissociation events, N_{el} and N_{pd}, are extracted from the area of the Gaussian.

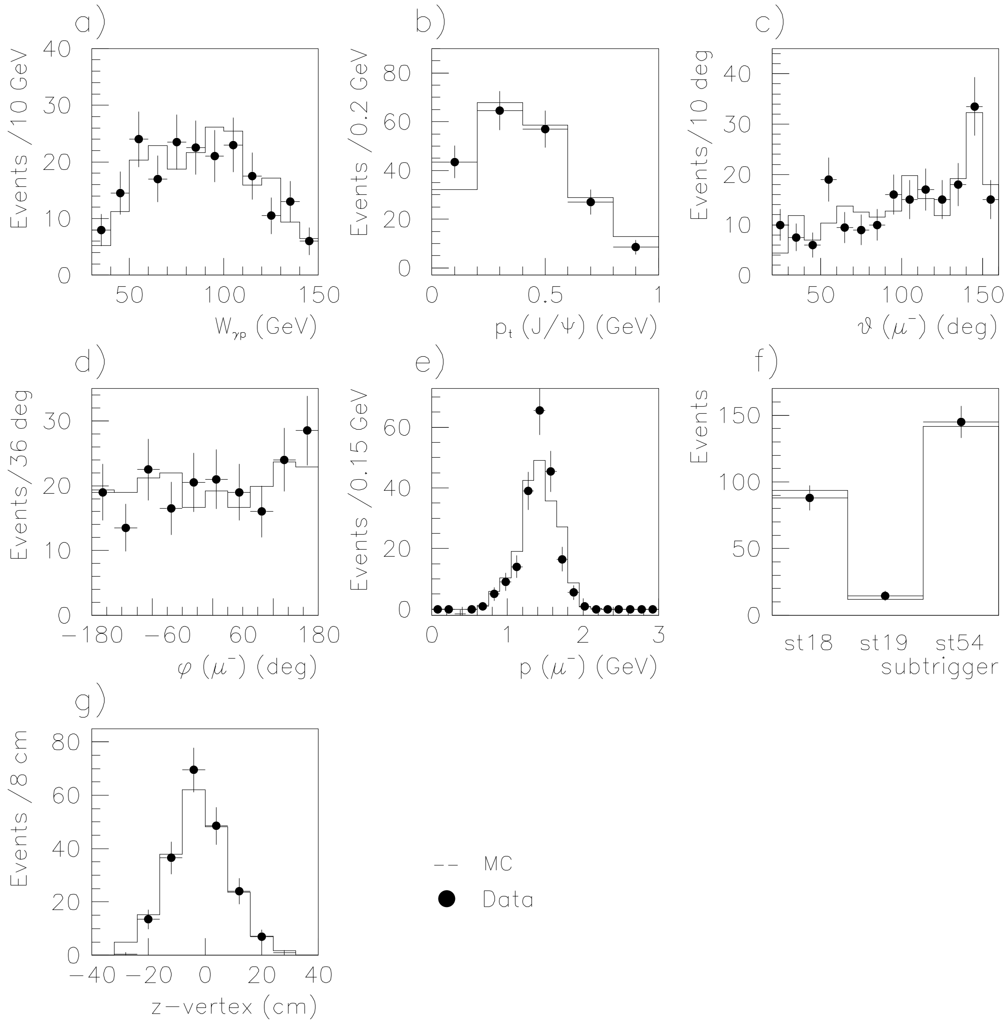

Figure 5.6: Control plots of the important event quantities for the elastic J/ψ sample:

a) Centre-of-mass energy of the photon-proton system.

b) The transverse momentum of the J/ψ .

c) θ of the negative muon in the event.

d) ϕ of the negative muon in the event.

e) Momentum of the negative muon in the event.

f) Subtrigger distribution.

g) z-vertex distribution.

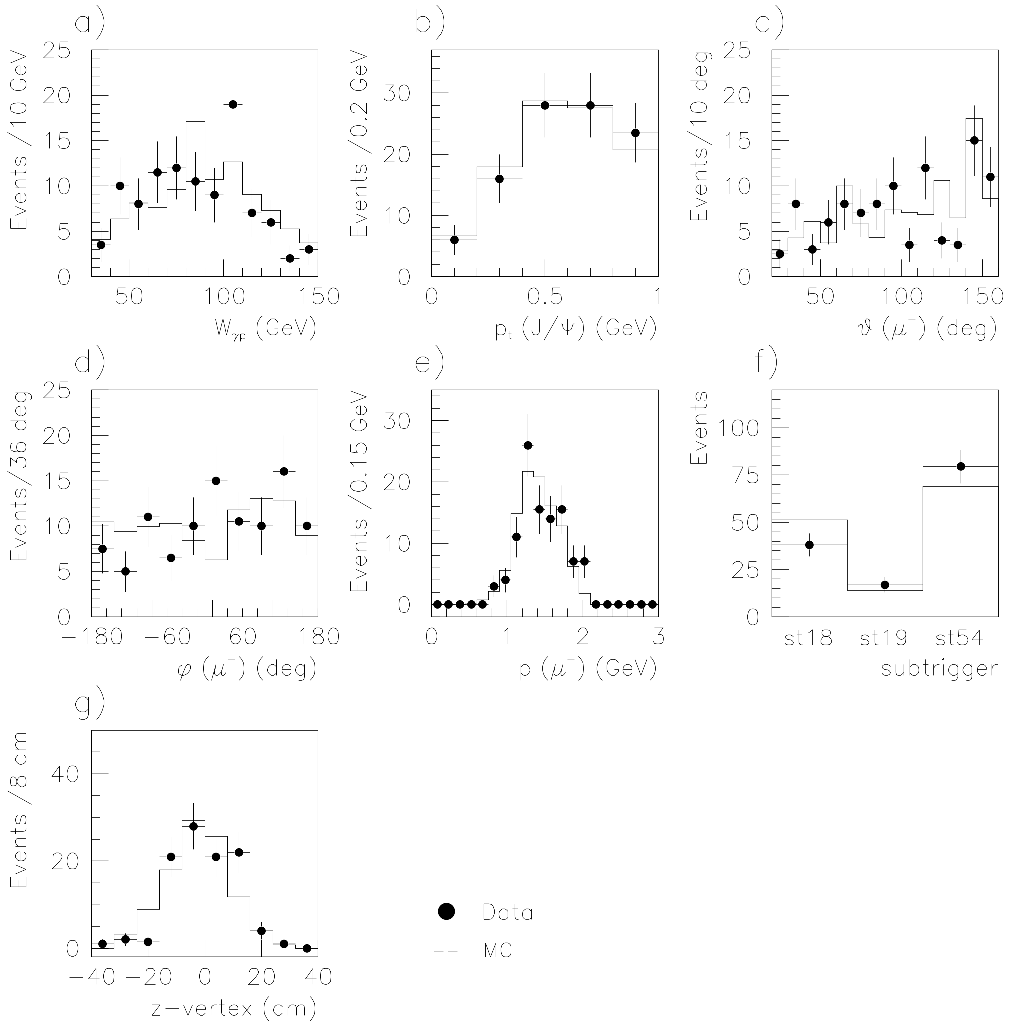

Figure 5.7: Control plots of the important event quantities for the proton-dissociative J/ψ sample:

a) Centre-of-mass energy of the photon-proton system.

b) The transverse momentum of the J/ψ .

c) θ of the negative muon in the event.

d) ϕ of the negative muon in the event.

e) Momentum of the negative muon in the event.

f) Subtrigger distribution.

g) z-vertex distribution.

it possible to misidentify these events as J/ψ decays. In the case of its direct decay to leptons, the invariant mass should be ~3.7 GeV and therefore would have been under-estimated by the reconstruction for it be included in the J/ψ sample. This contribution to the ψ' background should not specifically affect the J/ψ peak. However, the alternative scenario is that the ψ' decays to the J/ψ plus neutral or charged hadrons. Here, bad reconstruction of the event can mean that these extra, low momenta particles are not 'seen' and the decay of the J/ψ to a muon pair mimics that of direct J/ψ production. This decay specifically affects the J/ψ peak since the invariant mass of the decay muons from the indirectly produced J/ψ is, of course, the same as for the direct case.

Decay Channel	Branching Ratio(%)
$\psi' \longrightarrow J/\psi\ \mathrm{X} \longrightarrow \mu^+\mu^-\mathrm{X}$	0.77 ± 0.17
$\psi' \longrightarrow \mu^+\mu^-$	3.44 ± 0.17

Table 5.1: Relevant decay channels of the ψ' and their branching ratios. Values are taken from [34].

The contribution of ψ' production to the elastic and proton-dissociation samples, described in section 5.3, is estimated using generated J/ψ and ψ' events. The ψ' MC event files were normalised to those of the J/ψ using the ratio of their respective cross sections, measured to be 0.15 ± 0.04 by H1 [65], and the branching ratios of J/ψ and ψ' decays to muon pair final states. The likelihood of a ψ' event entering the data samples is then simply evaluated by applying the same selection cuts used to extract the elastic and proton-dissociative samples. The number of ψ' events, $N(\psi')_{el}$ and $N(\psi')_{pd}$, which contribute to the elastic and proton-dissociation samples respectively are listed in table 5.4.

5.5 Calculating Acceptances

The overall acceptances of the elastic and proton-dissociation samples are evaluated using MC events with the same kinematic range as the data so that $Q^2 < 1.2\,\mathrm{GeV}^2$; $z > 0.95$ and $30 < W_{\gamma p} < 150\,\mathrm{GeV}$ (see section 4.8.4). The acceptance values indicate the fraction of real events that will make it to the final data samples taking into account the efficiency of the H1 detector, the triggering and reconstruction and finally the selection cuts made in the analysis of the data. Therefore, it is essential that the MC model and detector simulation are reliable. Where small discrepancies between data and MC occur the MC can be re-weighted so that it matches the data more closely. The studies in chapter 4 were designed to locate possible sources of inaccuracy by comparing in data and MC the efficiencies of the trigger elements, the track reconstruction and the muon identification. The control plots shown in figures 4.10, 5.6 and 5.7 were similarly used to look for potential differences in distributions of the important event quantities. These studies found that in a few cases the MC needs to be tuned before it can be used to calculate acceptances for the cross section measurement. These can be summarised in the following list:

Corrections applied to the MC:

- The muon identification efficiency in the LAr is too high in MC, though the size of this discrepancy varies between 10-20% depending on the angle, θ, of the muons (see section 4.6).
- The efficiency of the DCRph_thig trigger element is too high in MC by 9.3%.
- The efficiency of the Mu_BEC trigger element is too low in MC by 14.7%.
- The z-vertex distribution needs to be re-weighted in order to match data.
- The t distributions need to be re-weighted to reflect more closely those of the elastic and proton-dissociation data samples.
- Noise has to be added to the simulation of the FMD response.

In addition the high voltage (HV) selection and trigger prescales, which are not simulated for the MC, need to be considered. This involves randomly applying a HV and prescale status to each generated event according to the conditions during data taking. This then takes into account the periods where essential sub-detectors were in-operational and includes variations over time of the prescale values. It is then possible to apply the data HV selection, described in section 4.2.2, to the MC, so that events are only selected where the relevant sub-detectors are working and in the readout. Likewise, this method allows a raw subtrigger which has been simulated by the MC to be checked to see whether it would have passed the same prescales applied to the data to become an actual subtrigger. The acceptance of these selections can be seen as part of the breakdown of the overall acceptances listed in tables 5.2 and 5.3.

Once the MC is known to model the data well in every respect the overall acceptances for the elastic and proton-dissociative samples can be calculated using the elastic and proton-dissociation versions of the MC respectively. Information on what effect the selection criteria are expected to have on the data sample can also be obtained by splitting the overall acceptance into categories. The fraction of the MC events which have two muons in the the angular region 20°$< \theta <$160° is denoted ε_{ang} and the proportion of these that then pass the HV selection is listed as ε_{hv}. Of those events left, the fraction that have a raw and then an actual subtrigger are denoted as ε_{raw} and ε_{actual} respectively, while the fraction passing the 2-track criteria is listed as ε_{2track}. A further category is used to illustrate the effect of the forward cuts on the data samples. In the elastic case ε_{fwd} is the fraction of two track events which also pass the forward cuts, whereas in the proton-dissociative case it represents the proportion that fail. The overall acceptances, ε_{el} and ε_{pd}, are obtained from the product of their constituent parts so that:

$$\varepsilon_{el}\,(\,\varepsilon_{pd}) = \varepsilon_{ang}\;\varepsilon_{hv}\;\varepsilon_{raw}\;\varepsilon_{actual}\;\varepsilon_{2track}\;\varepsilon_{fwd} \tag{5.2}$$

Parameter	$W_{\gamma p}$ bins (GeV)			
	30-60	60-90	90-120	120-150
ε_{ang}	0.365	0.680	0.568	0.326
ε_{hv}	0.696	0.711	0.695	0.709
ε_{raw}	0.439	0.512	0.594	0.578
ε_{actual}	0.786	0.801	0.770	0.804
ε_{2track}	0.542	0.513	0.601	0.587
ε_{fwd}	0.922	0.899	0.907	0.937
ε_{el}	0.044	0.092	0.098	0.059

Table 5.2: The contributions to the overall acceptance of the elastic sample calculated using the elastic version of the MC.

The contribution to the overall acceptance from ε_{raw} is seen to vary slightly with $W_{\gamma p}$ in tables 5.2 and 5.3. This is because it includes both the reconstruction and the triggering of the event. Due to the angular acceptance of the central tracker, tracks in the the low θ (low $W_{\gamma p}$) region are less likely to be reconstructed adequately than tracks at higher values of θ.

Parameter	$W_{\gamma p}$ bins (GeV)			
	30-60	60-90	90-120	120-150
ε_{ang}	0.336	0.667	0.580	0.3304
ε_{hv}	0.700	0.677	0.715	0.728
ε_{raw}	0.479	0.490	0.631	0.619
ε_{actual}	0.707	0.817	0.766	0.748
ε_{2track}	0.552	0.440	0.495	0.452
ε_{fwd}	0.789	0.817	0.693	0.767
ε_{pd}	0.035	0.064	0.067	0.038

Table 5.3: The contributions to the overall acceptance of the proton-dissociative sample calculated using the proton-dissociation version of the MC.

5.6 Estimating the Event Migration

As was explained in section 5.2, the forward cuts are not a conclusive test as to whether an event from the J/ψ sample is elastic or proton-dissociative. This is because they don't take into account the inefficiency of the sub-detectors in reconstructing the energy in the forward region or the lack of hermeticity at low angles due to the beam-pipe. To correct for this the inefficiency of the forward cuts is estimated using MC events. In the simultaneous equations below the ε variables represent acceptances determined from MC, where the superscripts mcel and mcpd specify either the elastic or the proton-dissociation version. The subscripts indicate whether the acceptance is for the elastic or proton-dissociation selection cuts. In this way it is possible to calculate N_{el}^{corr} and N_{pd}^{corr}, the corrected number of elastic and proton-dissociation events respectively.

$$\begin{aligned} N_{el} - N(\psi')_{el} &= N_{el}^{corr}\varepsilon_{el}^{mcel} + N_{pd}^{corr}\varepsilon_{el}^{mcpd} \\ N_{pd} - N(\psi')_{pd} &= N_{el}^{corr}\varepsilon_{pd}^{mcel} + N_{pd}^{corr}\varepsilon_{pd}^{mcpd} \end{aligned} \tag{5.3}$$

The remaining variables in equation 5.3 are N$_{el}$ and N$_{pd}$, the number of events in the elastic and proton-dissociation samples and $N(\psi')_{el}$ and $N(\psi')_{pd}$, the contributions to these samples from ψ' decays.

The values of the acceptances are listed in table 5.4 along with the resulting values of N_{el}^{corr} and N_{pd}^{corr} calculated from equation 5.3. The errors shown in the table are due to the statistical errors on the size of the elastic and proton-dissociation data samples. The quantities, N_{el}^{corr} and N_{pd}^{corr}, are each equivalent to N in equation 5.1 and, therefore, the ep cross section for the elastic and proton-dissociation processes can be calculated. These are listed in table 5.6.

Parameter	$W_{\gamma p}$ bins (GeV)			
	30-60	60-90	90-120	120-150
N_{el}	46 ± 7.1	64.1 ± 8.4	58.1 ± 7.9	30.4 ± 5.6
N_{pd}	22.3 ± 4.8	35.0 ± 5.9	32.7 ± 6.4	10.5 ± 0.7
$\mathrm{N}_{el}(\psi')$	1.5	2.6	1.2	1.4
$\mathrm{N}_{pd}(\psi')$	0.9	1.0	1.0	0.4
ε_{el}^{mcel}	0.0438	0.0916	0.0984	0.0590
ε_{pd}^{mcel}	0.0045	0.0100	0.0102	0.0040
ε_{el}^{mcpd}	0.0093	0.0146	0.0301	0.0118
ε_{pd}^{mcpd}	0.0327	0.0638	0.0671	0.0378
N_{el}^{corr}	912 ± 169	601 ± 95	451 ± 88	447 ± 96
N_{pd}^{corr}	496 ± 139	438 ± 93	404 ± 87	220 ± 21

Table 5.4: Table showing quantities relevant to the separation of the two track sample into the elastic and proton-dissociative processes. N_{el}^{corr} and N_{pd}^{corr} are the acceptance corrected numbers of elastic and proton-dissociation events once the inefficiency of the forward detectors has been taken into account. These values are equivalent to the quantity N in equation 5.1. The errors are due to the statistical uncertainty on the elastic and proton-dissociation data samples.

5.7 Systematic Errors

The systematic error on the cross section measurement largely emerges from the use of the MC to calculate the acceptances of the elastic and proton-dissociative samples. It has contributions from the MC efficiencies for the triggers, the track reconstruction, the muon identification, the forward cuts and the uncertainty on the MC model of J/ψ production. These are all evaluated separately and discussed in the following section. Other smaller sources of error come from the estimation of the ψ' contribution, the luminosity and branching ratio measurements. All the contributions to the systematic error on the elastic and proton-dissociation measurements are summarised in table 5.5.

Quantity	Systematic errors on ep cross sections(%)			
	30-60 GeV	60-90 GeV	90-120 GeV	120-150 GeV
	Trigger Elements.			
Topo_BR	4/3	4/3	2	1/0
Mu_Bar	0/1	0/1	0	0
Mu_FOEC	2	0	0	0
Mu_BEC	0	1	3/2	1
zVtx_Mu	0	0/1	1	1
zVtx_Cls	2	2	2	2
DCRph_tneg	3	3	1	1/0
DCRph_thig	0/1	0/1	1	2
Trigger total	7	5	4	3
	Muon identification in the calorimeter.			
20-60°	7	2/1	0	0
60-120°	4/3	6/7	4	0
120-130°	-	2/3	2/6	2
Calo id total	8	7/8	4/7	2
	Muon identification in the instrumented iron.			
20-140°	1	1/2	4/3	4
140-160°	-	2	5	10
Iron id total	1	2/3	6	11
	Other.			
Track reconstruction	3	3	3	3
MC model	6/8	3/4	7/9	6/10
MC statistics	4/7	3/6	6/8	5/7
Separation	9	9	9	9
ψ' contribution	3/2	3/2	2/5	4/5
Luminosity	1	1	1	1
Branching ratio	5	5	5	5
Overall total	17/18	16	17/20	18/20

Table 5.5: The contributions to the systematic error on the ep cross sections. Where there are two numbers listed per category, the first refers to the error on the elastic cross section and the second to that on the proton-dissociative cross section. The total is obtained by adding all the contributions in quadrature.

5.7.1 Efficiencies

The efficiency studies in chapter 4 allowed any significant variations between the MC and data to be tuned before calculating the acceptances of the data samples. The smaller differences that lie within the errors of each study are included now in the overall systematic uncertainty. The effects on the cross section measurement were evaluated separately for the uncertainty on each trigger element efficiency and the track efficiency error. This ensures that the resulting errors are independent and can be combined in quadrature. The error on the cross sections due to the trigger elements and the track reconstruction are 3-7% and 3% respectively. Likewise, the systematic error due to the muon identification is calculated by combining the separate errors due to each angular region in the calorimeter and instrumented iron, which gives a total uncertainty on the cross sections of 8-11%. The contributions making up this number are listed in table 5.5 along with the uncertainties due to the individual trigger elements.

5.7.2 Monte-Carlo Model and Statistics

Section 4.4 describes the MC model used to describe diffractive J/ψ production. The variable parameters, ϵ and k have been assigned values determined from experiment. The optimum values of b for the MC were found using a χ^2 fit to the data. Since the cross section measurement relies heavily on acceptances calculated from the MC it is necessary to assess the reliability of this MC model. This is achieved by varying each of the model parameters within their range of compatibility with the data sample and quantifying the change in the resulting cross sections. Each parameter is varied independently so that the resulting uncertainties can be added in quadrature.

The quantity ϵ, determines the dependence of the cross section on $W_{\gamma p}$. It takes a nominal value of 0.225 and was varied between ϵ=0.25 and ϵ=0.15, a range where the MC remains compatible with the data. The quantity, k, describes the relationship of the cross section to the proton remnant, in the case where it dissociates, where $\sigma \propto \frac{1}{M_Y^k}$. The nominal value was set by the experimental measurement of k=2.2 $\pm$ 0.2 [39] and so the uncertainty was obtained by varying its value within its errors. Lastly, the variable, b, which describes the relationship between the cross section and t ($\approx$ -p$_t(J/\psi)^2$), was varied by $\pm$ 1.2 around the nominal value of 5.7 for the elastic case and by $^{+0.5}_{-0.3}$ around the nominal value of 0.5 for the proton-dissociative case. The overall effect of varying the MC parameters is shown in table 5.5.

5.7.3 Elastic and Proton-Dissociation Separation

The largest individual contribution to the systematic error on the elastic and proton-dissociative cross sections is due to the separation of the two event types. Events where the proton dissociates are tagged using the three forward detectors. The inefficiency of the forward cuts causes small migrations between the elastic and proton-dissociative samples which are estimated using MC events. The uncertainty of this method was assumed not to be a function of energy so that a single value could be estimated over the four bins in $W_{\gamma p}$. Different combinations of two forward detectors were used to separate the data samples and the variation of the resulting values of the cross sections, calculated over the range $30 < W_{\gamma p} < 150$ GeV , was used to quantify the systematic error. The use of only the LAr and FMD detectors to tag the the proton remnant showed a change of 8% in the cross sections; the LAr and PRT a change of 7% and the PRT and FMD the small variation of 2%. A conservative error due to the separation of the two processes of 9% is thus applied.

5.7.4 ψ' Contribution, Luminosity and Branching Ratio

The ψ' contribution was calculated by normalising the ψ' MC to that of the J/ψ . This was achieved using the ratio of the ψ' and J/ψ cross sections and the branching ratios of both mesons to muon pairs. These are all experimentally determined and thus have errors associated with them and these are listed in section 5.4, table 4.1 and table 5.1. These result in errors on the cross sections of 2-5% and these are listed in table 5.5.

Finally, the measurement of the integrated luminosity and the branching ratio of the J/ψ to a muon pair contribute errors of 1% [66] and 5% [34] to the overall systematic error.

5.8 The Photon Flux

In order to compare the *ep* cross section defined in equation 5.1 with results from non-*ep* experiments it is necessary to convert to the γp cross section, $\sigma_{\gamma p}$. To do this an equivalent photon approximation [67] is used to calculate the flux of photons being emitted by the beam of positrons. Then the *ep* and γp cross sections are related by:

$$\sigma_{ep} = \int_{y_{min}}^{y_{max}} \int_{Q^2_{min}}^{Q^2_{max}} f_{\gamma/e}(y, Q^2)\sigma_{\gamma p}(y, Q^2) dy dQ^2 \tag{5.4}$$

where the photon flux is described by the function $f_{\gamma/e}$ and the ep cross section has been measured in the kinematic range $y_{min} < y < y_{max}$ and $Q^2_{min} < Q^2 < Q^2_{max}$. The minimum value of Q^2 available is $Q^2_{min} = m_e^2 \left(\frac{y^2}{1-y^2}\right)$ and the maximum value of 1.2 $\mathrm{GeV}^2$is set by the kinematic acceptance of the two track sample. The range in y is determined from the relation $W_{\gamma p} = sy - Q^2$ where $\sqrt{s}$ is the centre of mass energy of the positron-proton collision. In the photoproduction domain, where $Q^2 \approx 0$, it is appropriate to use the Weizsäcker-Williams approximation [68] [69] for $\mathrm{f}_{\gamma/e}$, considering only the transverse contribution to the γp cross section so that:

$$f_{\gamma/e} \approx f^T_{\gamma/e} = \frac{\alpha}{2\,\pi\,Q^2}\left(\frac{1+(1-y)^2}{y} - \frac{2\,m_e^2\,y}{Q^2}\right). \tag{5.5}$$

Here, α is the fine structure constant and m_e represents the mass of the electron. The contribution to the ep cross sections presented in this chapter from longitudinal photons is estimated to be less than 1%. The dependence of the γp cross section on the kinematical quantities y and Q^2 can be parameterised so that:

$$\sigma_{\gamma p}(y, Q^2) = \sigma_{\gamma p}(W_0, Q^2 = 0)\left(\frac{W}{W_0}\right)^{4\epsilon} \frac{1}{\left(1 + \frac{Q^2}{M^2_{J/\psi}}\right)^n} \tag{5.6}$$

where n has been measured as 2.1±0.3 by H1 [70] and $M_{J/\psi}$ is the mass of the resulting J/ψ meson. This makes it possible to compare the ep cross section measured across a region in $W_{\gamma p}$ with the equivalent γp value measured at a chosen value of W_0, using the simple relation:

$$\sigma_{\gamma p}(W_0, Q^2 = 0) = \frac{\sigma_{ep}}{\phi_{\gamma/e}} \tag{5.7}$$

where,

$$\phi_{\gamma/e} = \int_{ymin}^{ymax} \int_{Q^2min}^{Q^2max} f^T_{\gamma/e}(y, Q^2)\left(\frac{W}{W_0}\right)^{4\epsilon} \frac{1}{\left(1 + \frac{Q^2}{M^2_{J/\psi}}\right)^2} dy dQ^2. \tag{5.8}$$

The value of W_0 is chosen such that the uncertainty on $\sigma_{\gamma p}$ due to the variation of ϵ is minimised. The values of W_0 are quoted for each $W_{\gamma p}$ bin in table 5.6, along with the calculated flux factors and γp cross sections.

The errors present in the calculation of the flux factors are due to the uncertainty of the $W_{\gamma p}$ and Q^2 dependences assumed in equation 5.6. Therefore, to estimate the error on the flux factors due to the $W_{\gamma p}$ dependence ϵ was varied between 0.15 and 0.25 as in section 5.7.2. Likewise, n was varied between its experimental errors and the change in flux factors was quantified. Both alterations had little effect producing a combined error on $\phi_{\gamma/e}$ of less than 1%.

Parameter	$W_{\gamma p}$ bins (GeV)			
	30-60	60-90	90-120	120-150
$\sigma(ep \longrightarrow e\,J/\psi\,p)$ (nb)	$3.1 \pm 0.6 \pm 0.5$	$2.0 \pm 0.3 \pm 0.3$	$1.5 \pm 0.3 \pm 0.3$	$1.5 \pm 0.3 \pm 0.3$
$\sigma(ep \longrightarrow e\,J/\psi\,Y)$ (nb)	$1.7 \pm 0.5 \pm 0.3$	$1.5 \pm 0.3 \pm 0.2$	$1.4 \pm 0.3 \pm 0.2$	$0.8 \pm 0.1 \pm 0.2$
W_0 (GeV)	43.8	73.6	103.9	134.1
$\phi_{\gamma p}$	0.06913	0.03488	0.02161	0.01456
$\Delta\phi_{\gamma p}$ (%)	< 1	< 1	< 1	< 1
$\sigma(\gamma p \longrightarrow e\,J/\psi\,p)$ (nb)	$44.9 \pm 8.0 \pm 7.6$	$58.7 \pm 8.8 \pm 8.8$	$71.1 \pm 13.5 \pm 12.1$	$104.6 \pm 22.0 \pm 18.8$
$\sigma(\gamma p \longrightarrow e\,J/\psi\,Y)$ (nb)	$24.5 \pm 6.7 \pm 4.4$	$42.8 \pm 8.6 \pm 6.8$	$63.7 \pm 13.4 \pm 11.5$	$51.5 \pm 5.2 \pm 10.3$

Table 5.6: The results table showing the ep cross sections and the γp cross sections for the elastic and proton dissociative production of J/ψ mesons in photoproduction. W_0 is the corrected bin centre at which the photon flux, $\phi_{\gamma/e}$ is evaluated. The first error is the error due to the statistical uncertainty on the data samples and the second is the systematic contribution which is discussed and broken down in section 5.7.

Chapter 6

Results and Discussion

The models of elastic J/ψ production, reviewed in chapter 2, relate the cross section to the $W_{\gamma p}$ and t of the interaction. These relationships are explored in the following two sections using the cross section measurement presented in the last chapter. In the final section the angular distribution of the muons from the decay of the J/ψ is used to check that the polarisation of the J/ψ meson matches that expected from s-channel helicity conservation.

6.1 The Energy Dependence

The measurements of $\sigma(ep \longrightarrow eJ/\psi\, p)$ and $\sigma(ep \longrightarrow eJ/\psi\, \mathrm{Y})$, summarised in table 5.6, were calculated at increasing values of $W_{\gamma p}$. This energy dependence of the ep cross sections is shown in figure 6.1 for the elastic and proton-dissociative processes. However, to compare these cross section values with earlier measurements and theoretical predictions it is necessary to look at the converted γp cross sections which are also listed in table 5.6. The energy dependence of $\sigma_{\gamma p}$ for the elastic process is shown in figure 6.2, where other results from HERA and from lower energy experiments have been included. The lower energy points are from the experiments E401 [71], E516 [72] and E687 [73], located at Fermilab, which collided beams of real photons on various fixed targets. In these experiments J/ψ production occurred via the process $\gamma + N \rightarrow J/\psi + \mathrm{Y}$ where N represents a nucleon in a target atom. In the case of E401 a target of hydrogen or deuterium was used and photon energies of 60-300 GeV allowed four cross section measurements to be made over a range $11\,\mathrm{GeV} < W_{\gamma p} < 25\,\mathrm{GeV}$. The later experiment, E516, made a single measurement using a hydrogen target and an average photon energy of 105 GeV . This gave an elastic cross section of 11.1 nb^{-1} at $W_{\gamma p}$ =14 GeV and this point has been used to normalise the fits based on the soft pomeron model which are shown on the plot. The measurements by the E687 experiment were produced using a Beryllium target and a beam of photons ranging in energy from 100-375 GeV which translates to a range 15 GeV $<W_{\gamma p}<$27 GeV . Where necessary these low energy results have been updated with new values for the J/ψ branching ratio to leptons. The other high energy points from HERA show the results of independent analyses made by the H1 [39] and Zeus [74] collaborations using data taken in 1994.

As can be seen from figure 6.2, the experimental data shows an upwards trend with $W_{\gamma p}$ over the range 15 GeV $<W_{\gamma p}<$150 GeV . The soft pomeron model with the Donnachie-Landshoff parameterisation and $\alpha'_{I\!P}$=0, outlined in section 2.4.2, predicts the rise of the elastic cross section to be proportional to W$^{\delta}$, where δ=0.32. This function is shown by the dashed line in the plot and is seen not to describe the data. Using the same $\sigma \propto$W$^{\delta}$ parameterisation, a χ^2 fit to the four points from this analysis gives a value of δ=0.66±0.36, where the uncertainty of the fit takes into account both statistical and systematic effects. A combined fit to all the data points shown in figure 6.2 gives a value of δ=0.98±0.03.

The perturbative QCD calculations of elastic J/ψ production, performed by Ryskin [44], are also shown in figure 6.2. In this model the cross section depends quadratically on the gluon distribution, $xg(x,Q^2)$, where x is the fraction of the proton's momentum carried by the probed gluon and Q^2 is the scale at which the gluon density is probed. These quantities are given by:

$$x = \frac{Q^2 + M^2_{J/\psi} - t}{W^2_{\gamma p}}$$

$$q^2 = \frac{Q^2 + M^2_{J/\psi} - t}{4} \tag{6.1}$$

where, in the present case, Q^2 and t are negligible compared to M$^2_{J/\psi}$ so that Q^2≈2.4 GeV^2 and $x \sim 10^{-3}$. Assuming a gluon distribution of the form:

$$xg(x,Q^2) \propto x^{-\lambda}, \tag{6.2}$$

the cross section is then expected to behave as $\sigma \propto W^{4\lambda}_{\gamma p}$. The Ryskin parameter-

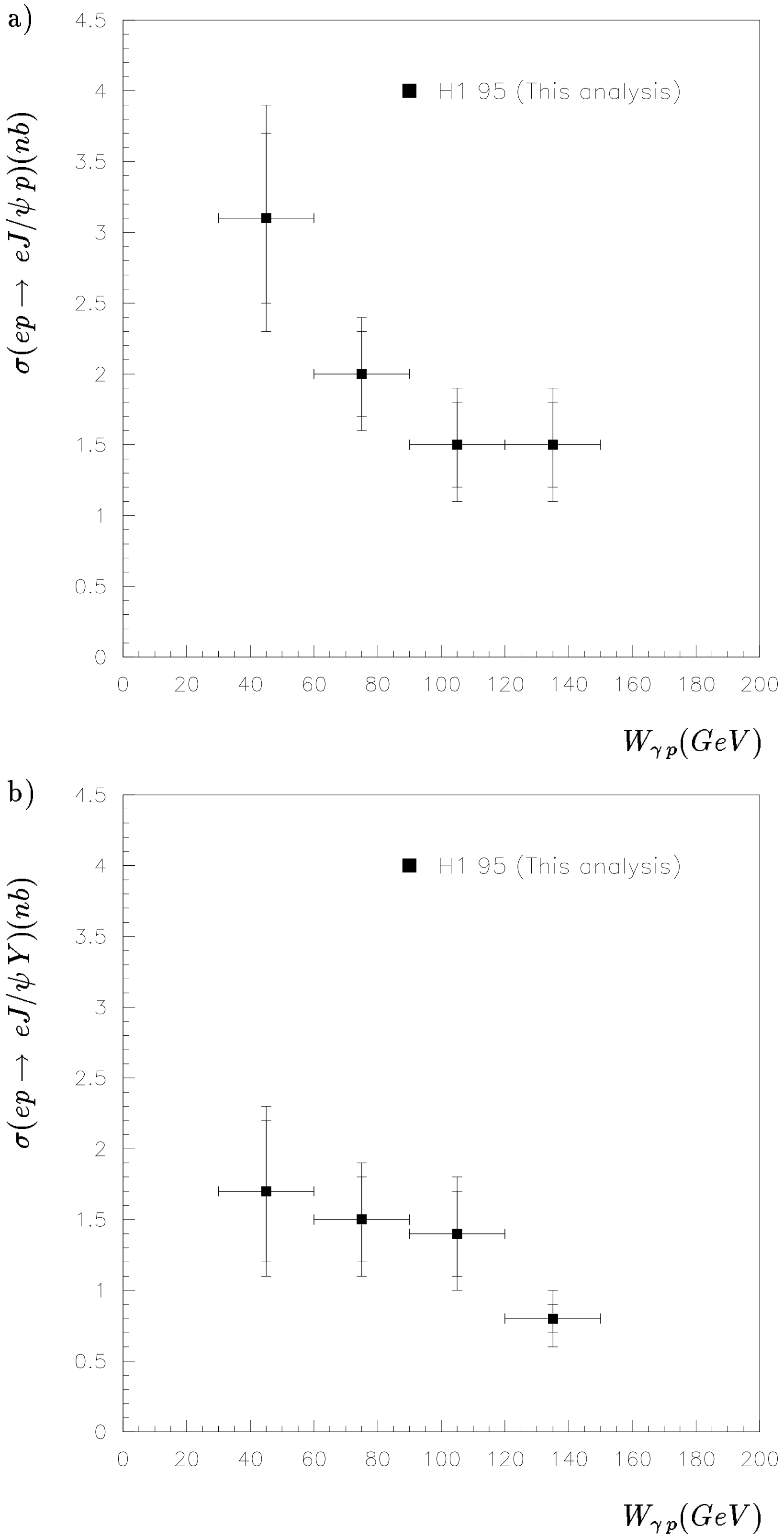

Figure 6.1: Total ep cross section for a) elastic J/ψ production and b) J/ψ production with proton-dissociation. The inner error bars show the statistical uncertainty and the outer ones the statistical and systematic contributions added in quadrature.

isations shown on the plot have been calculated using the two gluon distributions, MRSA$'$ [46] and GRV [45] which correspond to values of $\lambda \approx 0.2$ and $\lambda \approx 0.3$-0.4 respectively. The data points in figure 6.2, taken together over the whole energy range, appear to favour the shape of the MRSA$'$ distribution; however, the measurements obtained from this analysis, if taken in isolation, suggest a steeper energy dependence although not one that is compatible with the GRV distribution.

Figure 6.3 shows the energy dependence of the γp cross section for J/ψ production where the proton dissociates. A χ^2 fit to the four points from this analysis, using a function of the form $W_{\gamma p}^{\delta}$, gives a value of δ=0.64±0.46. The error includes both statistical and systematic uncertainties. This energy dependence is compatible to that of the elastic cross section. A combined fit using the results of both H1 analyses gives δ=0.81±0.17.

6.2 The t Dependence

Diffractive processes which occur at small values of t are expected to show an exponential t dependence. Further, models based on Regge theory predict shrinkage where the slope of the exponential dependence increases with energy. This phenomenon is expected to occur according to equation 2.17 where $\alpha'_{I\!P}$ takes a value of $0.25\,\mathrm{GeV}^{-2}$. In contrast the perturbative QCD model developed by Ryskin predicts little shrinkage. The quantity b is also interesting in that it can provide information about the size of the J/ψ meson. In equation 2.17 the constant b_0 can be related to the radii, R_P and $R_{J/\psi}$, of the proton and J/ψ such that:

$$b_0 = R_P^2 + R_{J/\psi}^2. \tag{6.3}$$

It is known that the proton, in hadronic interactions, has a squared radius of approximately $4\,\mathrm{GeV}^{-2}$.

In photoproduction, where the scattered positron is rarely tagged, it is not possible to directly measure t. Instead, it is approximated using the relationship $t=-p_t^2$ where p_t^2 represents the transverse momentum squared of the J/ψ . This approximation is only valid in the region $p_t^2 < 1\mathrm{GeV}^2$ where $Q^2 \approx 0$. The correlation between p_t^2 and t for the J/ψ data samples, where $Q^2 < 1.2\,\mathrm{GeV}^2$, is modelled by the DIFFVM MC generator and is illustrated in figure 6.4.

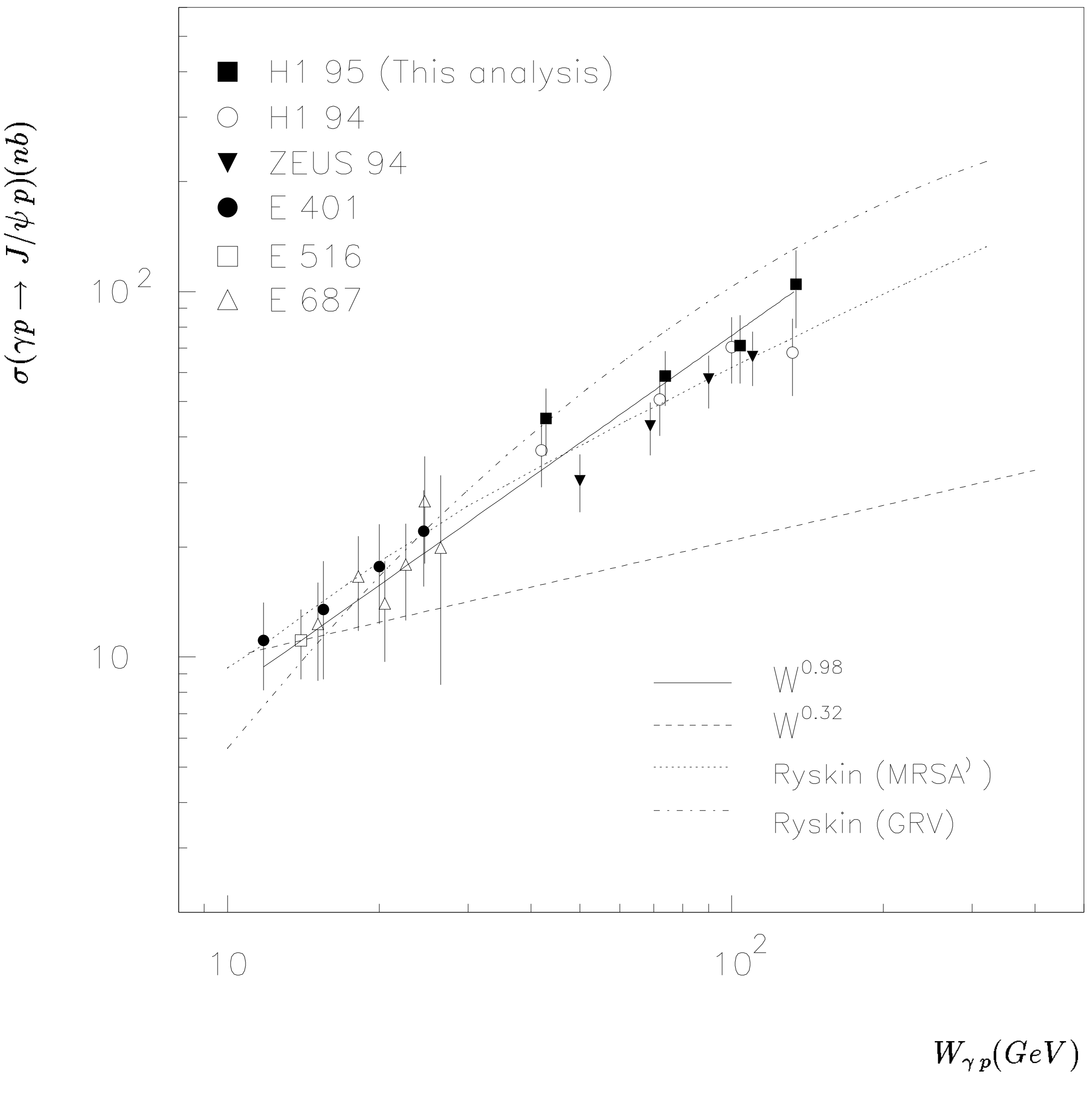

Figure 6.2: The γp cross section for the elastic production of J/ψ mesons. The lower energy points are quoted from the E401 [71], E516 [72] and E687 [73] experiments and the other HERA results are from independent analyses by H1 [39] and Zeus [74] made using data taken in 1994. The error bars on all the measurements represent statistical and systematic uncertainties added in quadrature. Theoretical predictions from the soft pomeron model and perturbative QCD are also shown and described in the text. A combined fit to all the data points with a function of the form $W_{\gamma p}^{\delta}$ gives a value of δ=0.98±0.03. This energy dependence is shown by the solid line.

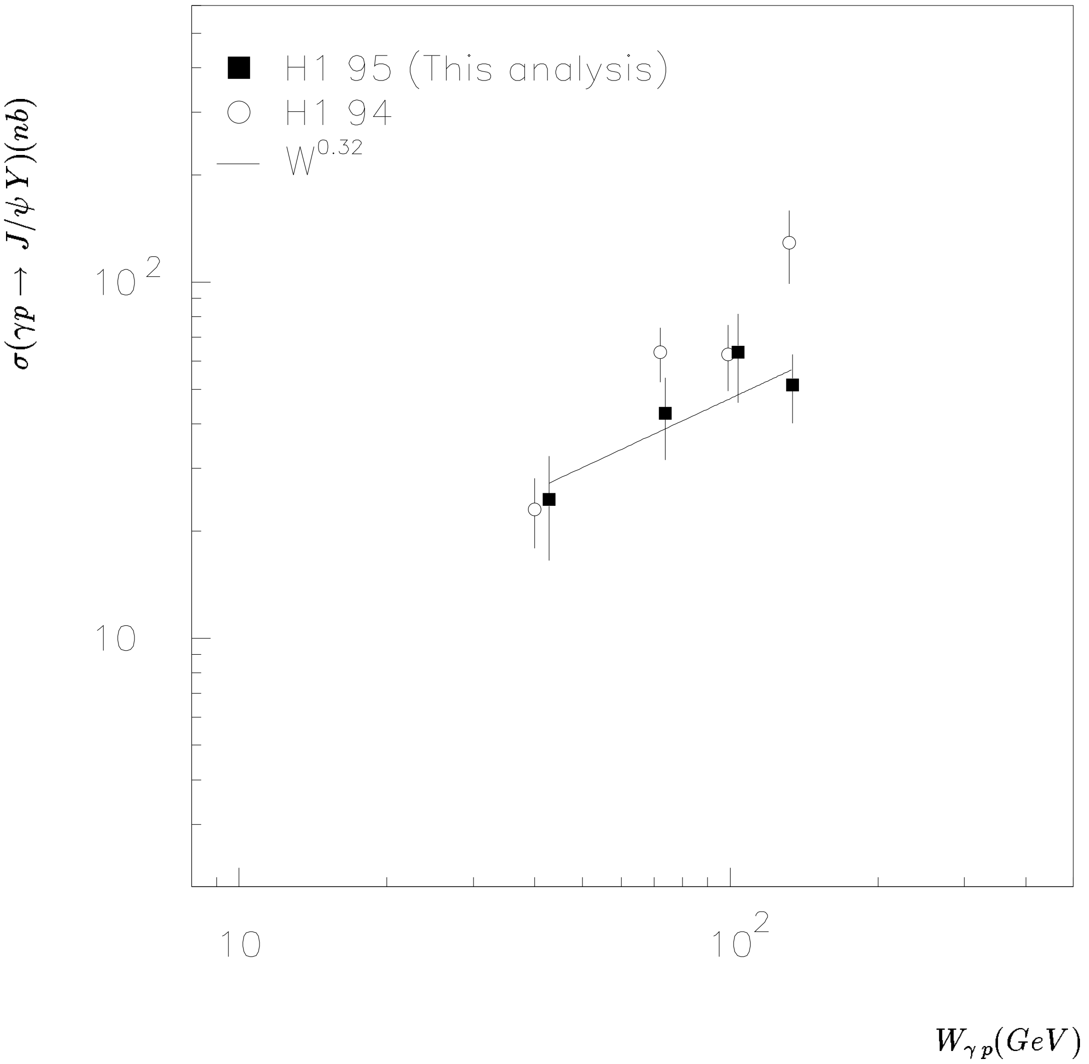

Figure 6.3: The γp cross section for the production of J/ψ mesons with proton-dissociation. The open circles show the results from an independent analysis made at H1 [39] using data taken in 1994. The errors bars on both sets of data represent statistical and systematic uncertainties added in quadrature. The solid line shows a fit to the four points from this analysis using a function of the form $W_{\gamma p}^{\delta}$ where δ=0.64±0.46.

The generated t dependences of both the elastic and proton-dissociative MC events were found not to reflect the p_t^2 distributions of the data taken in 1995. In correcting for this the exponential behaviour of the t-distributions was retained; however, the generated b values for the two processes were optimised using a χ^2 fit. This was achieved by fitting generated t-distributions to the elastic and proton-dissociative data samples where non-resonant and ψ' backgrounds had been removed. The sample of MC events was made up of 60% elastic and 40% proton-dissociative events in order to reflect the contributions to the data sample, as indicated by the final cross section measurements presented in chapter 5. The optimum slopes for the t-distributions are found to be $b = 5.7 \pm 0.9(stat) \pm 0.8(syst)\,\mathrm{GeV}^{-2}$ for the elastic process and $b = 0.5 \pm^{0.5}_{0.3}(stat) \pm 0.0(syst)\,\mathrm{GeV}^{-2}$ for the proton-dissociative process. Here the statistical error is given by $\chi^2 \pm 1$ and the systematic error is obtained by varying the number of bins in the fit. The fit is only reliable in the region where $p_t^2 < 1\mathrm{GeV}^2$ due to the limited data statistics outside, therefore all the acceptances and cross sections are measured inside this kinematic limit.

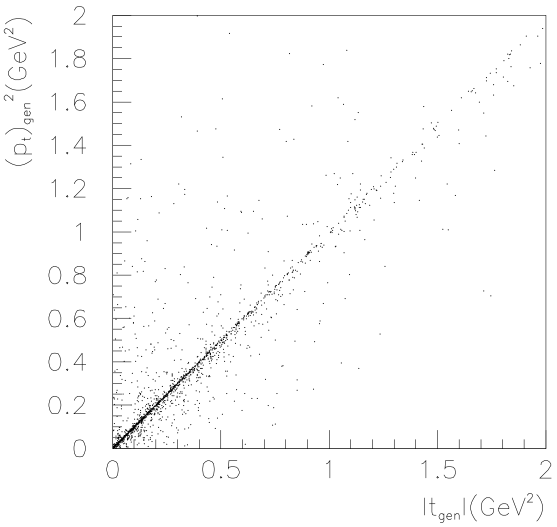

Figure 6.4: The correlation between the generated t and p_t^2 distributions as modelled by the DIFFVM MC generator.

The results presented in this section require that the J/ψ cross section is recalculated, this time in bins of p_t^2. The procedure followed is identical to that presented in the last chapter apart from the change of bin variable. Figure 6.5 shows the resulting distributions of $\frac{d\sigma_{ep}}{dp_t^2}$ for the elastic and proton-dissociative processes. In each case a small correction has been made bin-by-bin for the difference in the generated p_t^2 and its reconstructed quantity. The error bars on the data points indicate the statistical and systematic errors added in quadrature. Bin-centre corrections are found to be of the order of 5% and have, therefore, not been included. For the purposes of comparison, the DIFFVM MC prediction is indicated by the dotted line. The solid line shows the log-likelihood fits to the data using the function $Ae^{-bp_t^2}$ which give values of the slope parameters of b=5.8±1.0 GeV^{-2} for the elastic case and b=0.1±0.8 GeV^{-2} for the proton-dissociative process. The errors on these values reflect only the statistical uncertainty since the systematic contributions were found to be highly correlated and were therefore neglected during the fit procedure. Using a χ^2 fit as an alternative gives compatible values for b in each case.

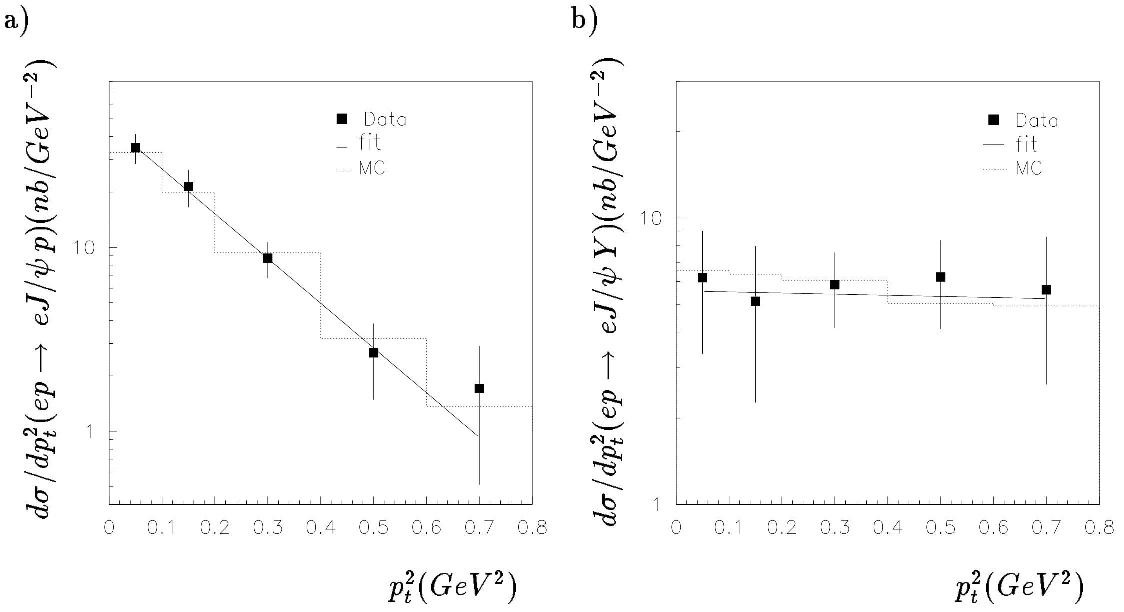

Figure 6.5: The differential cross section as a function of p_t^2 and integrated over the range 30<$W_{\gamma p}$ <150 GeV for a) elastic J/ψ production and b) J/ψ production with proton-dissociation. The dotted line shows the prediction from the DIFFVM MC and the solid line shows the fit to the data using an exponential function of the form $e^{-bp_t^2}$. Values of the slope parameter are found to be b=5.8±1.0 GeV^{-2} and b=0.1±0.8 GeV^{-2} for the elastic and proton-dissociative processes respectively.

The values of b extracted from figure 6.5 can be compared to previous results from HERA. In the case of the elastic process H1 and Zeus, using data taken in 1994, obtain the values b=4.0±0.3 GeV^{-2} [39] and b=4.3±0.7 GeV^{-2} [74] respectively. The quantity b from this analysis is larger than both of these results suggesting a steeper t dependence. However, the large error means that its compatibility with the H1 and Zeus values is reasonable. For the proton-dissociative case H1, again using data from 1994, states that b=1.6±0.2 GeV^{-2} [39]. The value obtained from this analysis is significantly smaller than this which reflects the very flat p_t^2 distribution observed in the data.

As well as understanding the p_t^2 and t dependences of the elastic and proton-dissociative samples, the b value can also yield information on the size of the J/ψ meson. The slope parameter, b, has been measured at HERA for the elastic production of the ρ^0, ω and ϕ mesons at $Q^2{\sim}0$ and over a similar energy range to that explored in this analysis. For the ρ^0 meson Zeus and H1 found that $b=9.8\pm1.4\,\mathrm{GeV}^{-2}$ [75] and $b=10.9\pm2.4\,\mathrm{GeV}^{-2}$ [76] respectively. The ω meson gives a value of $b=10.0\pm1.7\,\mathrm{GeV}^{-2}$ [77] and the ϕ meson gives a value of $b=7.3\pm1.3\,\mathrm{GeV}^{-2}$ [78]. The fact that the slope parameter of the J/ψ is smaller than these indicates that the radius of the J/ψ meson is smaller than those of the lighter mesons. If the mesons are regarded as a $q\bar{q}$ wave packet then the interpretation of this result is that the charm quarks are bound more tightly together in the J/ψ than in the mesons made up from the lighter quark flavours. At H1 the slope parameter has also been measured for elastic J/ψ production at $Q^2{>}8\,\mathrm{GeV}^2$ and is found to be $b=3.8\pm2.2\,\mathrm{GeV}^{-2}$ [79]. Although the errors on this measurement do not allow a strong statement it could suggest that the size of the J/ψ meson decreases as Q^2 increases in a similar way to the ρ meson [80].

To study the energy dependence of the slope parameter the elastic data sample is split into two regions of $W_{\gamma p}$ and the p_t^2 analysis repeated as before. Unfortunately, the limited statistics of the proton-dissociative sample does not allow similar treatment. The distributions of $\frac{d\sigma_{ep}}{dp_t^2}$ for the two energy ranges of the elastic sample are shown in figure 6.6 along with log-likelihood fits to the data using the function $Ae^{-bp_t^2}$. These fits give values of the slope-parameter over the two regions $30{<}W_{\gamma p}{<}90\,\mathrm{GeV}$ and $90{<}W_{\gamma p}{<}150\,\mathrm{GeV}$ as $b=4.9\pm0.8\,\mathrm{GeV}^{-2}$ and $b=6.5\pm1.0\,\mathrm{GeV}^{-2}$ respectively. The expected rise in b over the HERA energy range is predicted by Regge theory to be $0.6\,\mathrm{GeV}^{-2}$ which is smaller than the errors on the measured b-slopes making it impossible to make any conclusions about shrinkage with this size of data sample. Unfortunately, measurements of b from the lower energy experiments discussed in section 6.1 have not proved consistent with one another ranging from $b{\approx}3\,\mathrm{GeV}^{-2}$ to $b{\approx}5\,\mathrm{GeV}^{-2}$ [71] [72] [73].

The t dependence of the elastic and proton-dissociative cross sections can be reconstructed using the correlation between t and p_t^2 described by the MC. A small correction is made to the number of data events in each bin of p_t^2 to account for the expected difference between the p_t^2 and t distributions. The differential cross sections as a function of t are shown in figure 6.7 for both the elastic and proton-dissociative processes. The error bars show the statistical and systematic errors added in quadrature and the dotted line shows the DIFFVM MC prediction. By

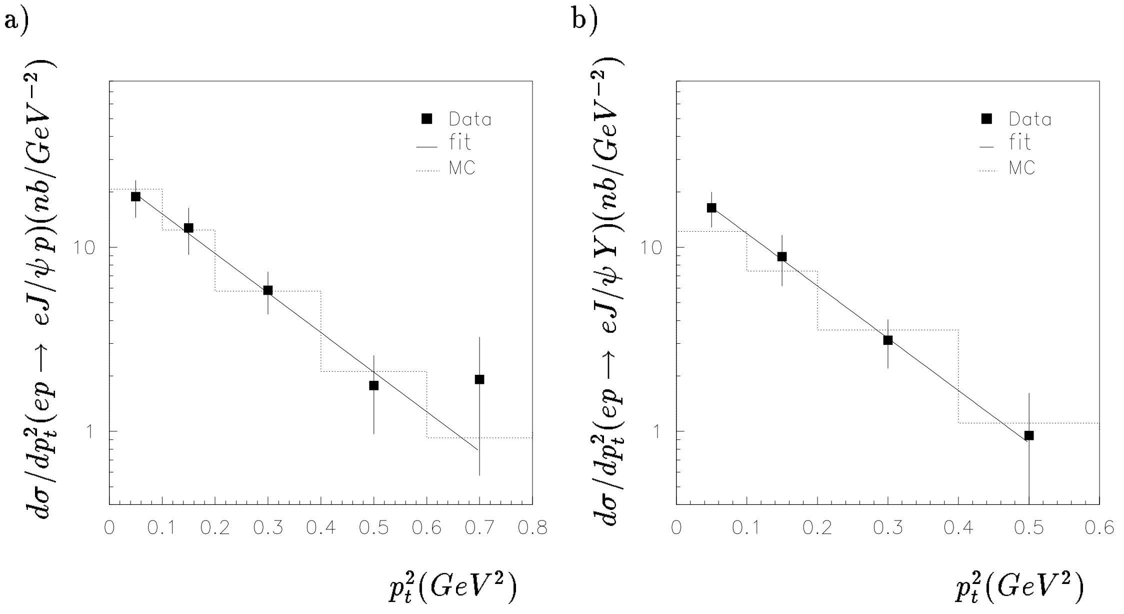

Figure 6.6: The differential cross sections for elastic J/ψ production integrated over a) $30<W_{\gamma p}<90$ GeV and b) $90<W_{\gamma p}<150$ GeV. The error bars represent the statistical and systematic uncertainties added in quadrature. The dotted line shows the prediction from the DIFFVM MC and the solid lines show the fits to the data using a function of the form $e^{-bp_t^2}$. Values of the slope parameter are found to be b=4.9±0.7 GeV^{-2} and b=6.5±1.0 GeV^{-2} for the lower and upper energy range respectively.

fitting an exponential function to the data of the form $Ae^{-b_t t}$ the slope parameters, b_t, are found to be b_t=5.6±0.9 GeV^{-2} for the elastic process and b_t=0±0.9 GeV^{-2} for the proton-dissociative process. These values are consistent with the optimum values of b found earlier in this section which were used to re-weight the generated t distributions in order to obtain better agreement with the t dependence shown by the data.

6.3 Angular Decay Distribution

Both the Regge based models of elastic J/ψ production and those exploiting perturbative QCD make the assumption of s-channel helicity conservation (SCHC) [29] [81]. In the region of $Q^2{\approx}0$ J/ψ mesons are produced predominantly by transversely polarised photons, consequently, if SCHC is seen to hold then the J/ψ will retain this transverse polarisation in its final state. The polarisation of the J/ψ meson is

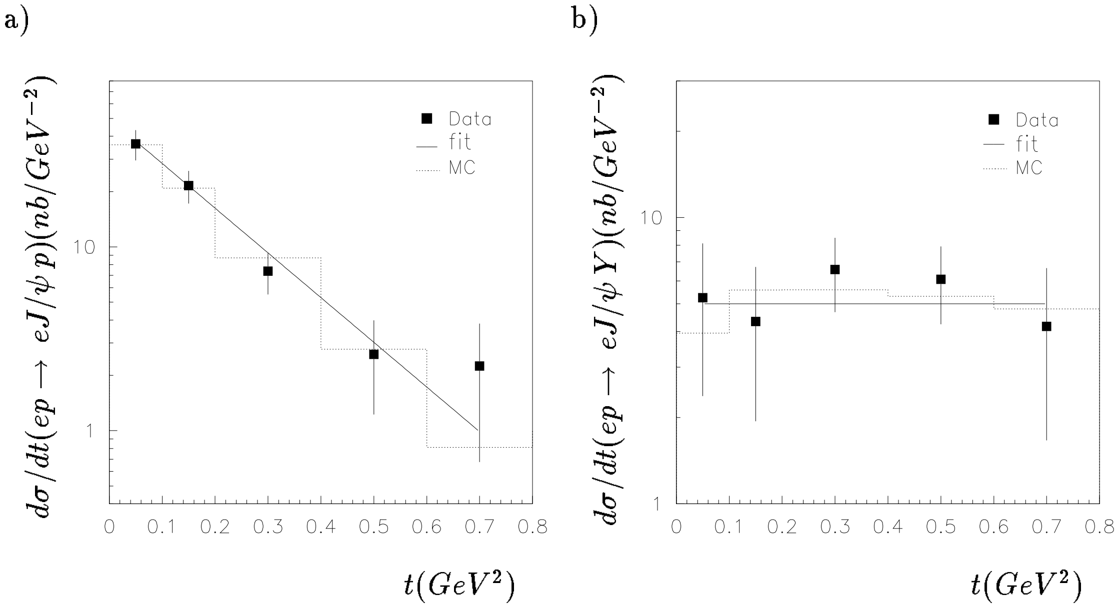

Figure 6.7: The differential cross sections as a function of t and integrated over the range $30 < W_{\gamma p} < 150$ GeV for a) elastic J/ψ production and b) J/ψ production with proton-dissociation. The error bars represent statistical and systematic errors added in quadrature. The dotted line indicates the DIFFVM MC prediction. The solid lines show log-likelihood fits to the data using a function of the form $e^{-b_t t}$ which give values of b_t of 5.6 ± 0.9 GeV^{-2} and 0 ± 0.9 GeV^{-2} for the elastic and proton-dissociative processes respectively.

accessible experimentally by studying the angular distributions of the muons from the decay of the J/ψ [82]. The characterisation of the helicity of the photon-J/ψ transition in photoproduction requires the definition of θ^* and ϕ^*, the polar and azimuthal angles of the positively charged μ in the helicity frame. This frame is where the J/ψ is at rest and the quantisation axis is taken to lie along the J/ψ direction in the γp centre-of-mass system. At low values of $|t|$ the photon and vector-meson become almost collinear, making the angle ϕ^* difficult to measure. Thus, for this analysis only the behaviour of the cross section as a function of θ^* is studied. In this case, according to SCHC, the expected angular distribution is:

$$\frac{d\sigma}{d\cos\theta^*} \propto (1-\rho)\sin^2\theta^* + \rho\left(\frac{1+\cos^2\theta^*}{2}\right) \tag{6.4}$$

where ρ represents the fraction of transversely polarised J/ψ mesons, which is predicted to be equal to 1.

To test this relationship the *ep* cross sections were recalculated in bins of $|cos\theta^*|$. In this instance, however, the elastic and proton-dissociative processes are not separated and the whole J/ψ sample is used in order to increase the statistical significance of the result. This method makes the reasonable assumption that the helicity structure of both processes is the same. In a further attempt to maximise the data statistics in each bin the modulus of the variable $cos\theta^*$ is used. Figure 6.8 shows the resulting *ep* cross section for diffractive J/ψ production as a function of $|cos\theta^*|$. The inner error bars on the data points represent the statistical uncertainty and the outer bars show the statistical and systematic contributions to the error added in quadrature. The solid line shows a χ^2 fit to the data using the function given in equation 6.4. This yields a value of ρ=1.0±0.1, where the error includes both statistical and systematic contributions. This result is consistent with SCHC within the experimental uncertainties and is in agreement with the value ρ=1.2±0.2 [39] obtained from the independent H1 analysis made using data taken in 1994.

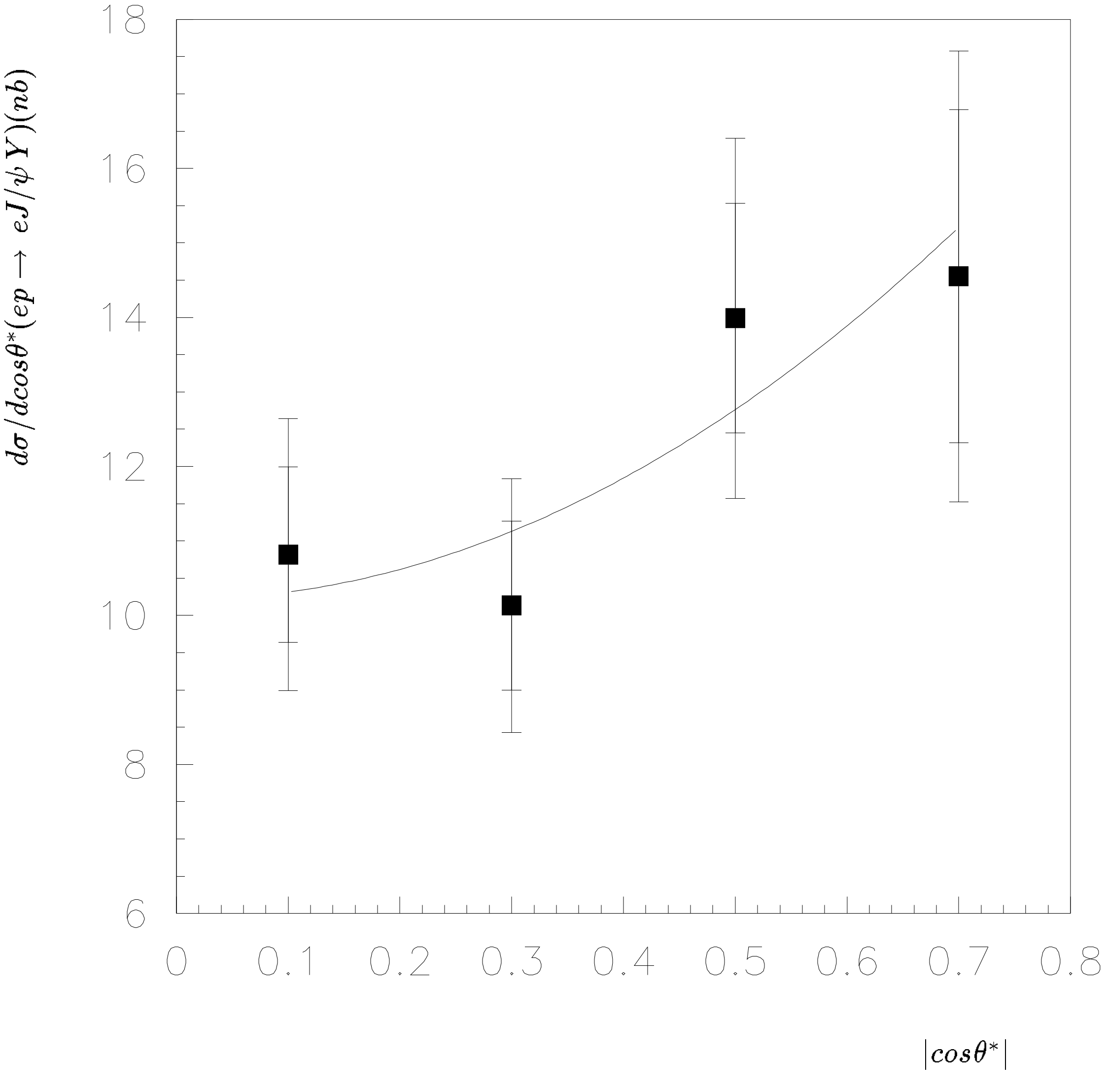

Figure 6.8: The differential cross section as a function of $cos\theta^*$ for diffractive J/ψ production integrated over the region $30 < W_{\gamma p} < 150$ GeV . The inner error bars show the statistical error and the outer ones represent the statistical and systematic errors added in quadrature. The solid line shows the χ^2 fit to the data using the function in equation 6.4 which yields a value of ρ=1.0±0.1.

Chapter 7

Summary

This thesis has presented a study of diffractive J/ψ photoproduction at HERA using the decay channel J/ψ $\longrightarrow$ $\mu^+\mu^-$. A measurement of the elastic γp cross section as a function of $W_{\gamma p}$ and in the kinematic range $30 < W_{\gamma p} < 150\,\mathrm{GeV}$; $Q^2 < 1.2\,\mathrm{GeV}^2$; $z > 0.95$ and $p_t^2 < 1\,\mathrm{GeV}^2$ is found to be:

$$\sigma(\gamma p \longrightarrow J/\psi p) = \begin{cases} 44.9 \pm 8.0 \pm 7.6\,\mathrm{n}b & at \quad W_{\gamma p} = 43.8\,GeV \\ 58.7 \pm 8.8 \pm 8.8\,\mathrm{n}b & at \quad W_{\gamma p} = 73.6\,GeV \\ 71.1 \pm 13.5 \pm 12.1\,\mathrm{n}b & at \quad W_{\gamma p} = 103.9\,GeV \\ 104.6 \pm 22.0 \pm 18.8\,\mathrm{n}b & at \quad W_{\gamma p} = 134.1\,GeV \end{cases}$$

Phenomenological models of elastic J/ψ production based on the Regge theory of soft hadronic interactions fail to describe the steep rise of this cross section with energy compared to measurements taken at lower centre-of-mass energies. Using the dependence $\sigma \propto W_{\gamma p}^{\delta}$ predicted by these models a combined fit to all the available data over the range $15 < W_{\gamma p} < 150\,\mathrm{GeV}$ yields a value of $\delta = 0.98 \pm 0.03$, approximately three times larger than the value predicted. The steep rise is better modelled by perturbative QCD calculations which are sensitive to the rise of the gluon density at low values of x. The MRSA$'$ parameterisation of the gluon distribution, found to model $F_2(x,Q^2)$ measurements at H1, is favoured by the data. Since the lighter vector mesons have been successfully modelled by soft models, it seems likely that due to the larger mass of the charm quark, diffractive J/ψ production takes place via a hard pomeron which can be described by perturbative QCD. The slope parameter for the elastic process was determined from the relationship $\frac{d\sigma_{ep}}{dp_t^2} \propto e^{-bp_t^2}$, integrated over the region $30 < W_{\gamma p} < 150\,\mathrm{GeV}$, and was found to be $b = 5.8 \pm 1.0\,\mathrm{GeV}^{-2}$. Comparing this value to measurements of the slope parameter for the lighter vector mesons, it suggests that the J/ψ meson has a smaller radius. No statement can be made about the energy dependence of b since the experimental errors are larger than the expected shrinkage of $0.6\,\mathrm{GeV}^{-2}$. To further understand the J/ψ production mechanisms, studies over wider ranges in $W_{\gamma p}$ are needed and the statistical uncertainties on the present measurements need to be reduced with increased luminosities and the study of alternative decay channels.

A measurement was also made of the γp cross section for J/ψ production with proton-dissociation in the same kinematic range. This is found to be:

$$\sigma(\gamma p \longrightarrow J/\psi Y) = \begin{cases} 24.5 \pm 6.7 \pm 4.4\,\mathrm{n}b & at \quad W_{\gamma p} = 43.8\,\mathrm{G}eV \\ 42.8 \pm 8.6 \pm 6.8\,\mathrm{n}b & at \quad W_{\gamma p} = 73.6\,\mathrm{G}eV \\ 63.7 \pm 13.4 \pm 11.5\,\mathrm{n}b & at \quad W_{\gamma p} = 103.9\,\mathrm{G}eV \\ 51.5 \pm 5.2 \pm 10.3\,\mathrm{n}b & at \quad W_{\gamma p} = 134.1\,\mathrm{G}eV \end{cases}$$

The energy dependence of the cross section was parameterised with the function $W_{\gamma p}^{\delta}$ and a fit to the data gave a value of δ=0.64±0.46. The slope parameter was measured to be b=0.1±0.8 GeV^{-2}, indicating a significantly flatter p_t^2 distribution than for the elastic process.

Finally, the decay angular distribution in the helicity frame of the J/ψ was determined for the combined elastic and proton-dissociative samples. It is found within errors to be consistent with that expected from s-channel helicity conservation, which is assumed by both the soft and hard models of J/ψ production.

References

[1] B. R. Martin and G. Shaw. *Particle Physics.* John Wiley and Sons, 1992.

[2] Donald H. Perkins. *Introduction to High Energy Physics.* Addison-Wesley, 1982.

[3] F. Halzen and A. D. Martin. *Quarks and Leptons.* Wiley, 1984.

[4] G. Wolf. *HERA physics.* DESY preprint 94–022 (1994).

[5] M. Gell-Mann. *A schematic model of baryons and mesons.* Phys. Rev. Lett. 8 (1964) 214–215.

[6] J. E. Augustin et al. *Discovery of a narrow resonance in e^+e^- annhilation.* Phys. Rev. Lett. 33 (1974) 1406–1408.

[7] J. J. Aubert et al. *Experimental observation of the heavy particle J.* Phys. Rev. Lett. 33 (1974) 1404–1406.

[8] G. S. Abrams et al. *The discovery of a second narrow resonance in e^+e^- annhilation.* Phys. Rev. Lett. 33 (1974) 1452–1455.

[9] S. W. Herb et al. *Observation of a dimuon resonance at 9.5 GeV in 400 GeVproton-nucleus collisions.* Phys. Rev. Lett. 39 (1977) 252–255.

[10] W. R. Innes et al. *Observation of structure in the upsilon region.* Phys. Rev. Lett. 39 (1977) 1240.

[11] CDF Collaboration. *Observation of the top quark production in $p\bar{p}$ collisions.* Phys. Rev. Lett. 74 (1995) 2626–2631.

[12] D0 Collaboration. *Observation of top quark.* Phys. Rev. Lett. 74 (1995) 2632–2637.

[13] C.G. Callan and D.G. Gross. *High energy electroproduction and the constitution of the electric current.* Phys. Rev. Lett. 22 (1969) 156–159.

[14] H1 Collaboration. *A measurement and QCD analysis of the proton structure function* $F_2(x, Q^2)$ *at HERA*, 1996. DESY 96-039.

[15] R. Feynman. *Very high energy collisions of hadrons.* Phys. Rev. Lett. 23 (1969) 1415–1417.

[16] J.D. Bjorken and E.A. Paschos. *Inelastic e-p and* γ*-p scattering and the structure of the nucleon.* Phys. Rev. 185 (1969) 1975–1982.

[17] M. Breidenbach et al. *Observed behaviour of highly inelastic electron-proton scattering.* Phys. Rev. Lett. 23 (1969) 935–939.

[18] Yu. L. Dokshitzer. *Calculation of structure functions of deep-inelastic scattering and* e^+e^- *annhilation by perturbation theory in quantum chromodynamics.* Sov. Phys. JETP 46 (1977) 641–653.

[19] V.N. Gribov and L.N. Lipatov. e^+e^- *pair annhilation and deep inelastic e-p scattering in perturbation theory.* Sov. J. Nucl. Phys. 15 (1972) 675–684.

[20] G. Altarelli and G. Parisi. *Asymptotic freedom in parton language.* Nucl. Phys. B (1977) 298–318.

[21] H1 Collaboration. *Inclusive parton cross sections in photoproduction and photon structure.* Nucl. Phys. B445 (1995) 195–215.

[22] H1 Collaboration. *Low q2 jet production at hera and virtual photon structure.* Phys. Lett B415 (1997) 418–434.

[23] S. J. Maxfield. *Some aspects of photoproduction at HERA.* J. Phys. G 22 (1996) 787–796.

[24] J. J. Sakurai. Ann. Phys. 11 (1960) 1.

[25] J.J Sakurai and D. Schildknecht. *General vector dominance and inelastic electron-proton scattering.* Phys. Lett. B40 (1972) 121–136.

[26] M. Greco. *Deep-inelastic processes.* Nucl. Phys. B63 (1973) 398–412.

[27] T. Regge. *Introduction to complex orbital momenta.* Nuovo Cim. 14 (1959) 951.

[28] H. Yukawa. *On the interaction of elementary particles.* Proc. Phys. Math. Soc. Japan 17 (1935) 48–57.

[29] P.D.B. Collins. *An Introduction to Regge Theory and High Energy Physics.* Cambridge University Press, 1977.

[30] P.D.B. Collins and A.D. Martin. *Hadron Interactions.* Adam Hilger Ltd., 1984.

[31] P. Burq et al. *Experimental results on pp forward elastic scattering and the possibility of universal shrinkage of the hadronic diffraction cone.* Phys. Lett. B 109 (1982) 124–128.

[32] A. Donnachie and P.V. Landshoff. *Elastic scattering and diffraction dissociation.* Nucl. Phys. B244 (1984) 322.

[33] H1 Collaboration. *Measurement of the total photon proton cross section and its decompositition at 200 GeV centre of mass energy.*, 1995. DESY 95-162.

[34] Particle Data Group (R. M. Barnett et al.). *Review of Particle Properties.* Phys. Rev. D54 1 (1996).

[35] W. Buchmüller and G. (Editors) Ingelman. *Physics at HERA: Proceedings of the workshop, hamburg,.*

[36] E.L. Berger and D. Jones. *Inelastic production of* J/ψ *and* v *by gluons.* Phys. Rev. D23 (1981) 1521–1530.

[37] M. Cacciari and M. Krämer. *Colour octet contributions to* J/ψ *photoproduction.* Phys. Rev. 76 (1996) 4128–4131.

[38] CDF collaboration. *Inclusive* J/ψ *,* $\psi(2s)$ *and b quark production in* $p\bar{p}$ *collision at* $s^{\frac{1}{2}}=1.8$ *Tev.* Phys. Rev. Lett. 69 (1992) 3704–3708.

[39] H1 Collaboration. *Elastic and inelastic photoproduction of* J/ψ *mesons at HERA*, 1996. DESY- 96-037.

[40] Krämer M., Zunft J., Steegborn J., and Zerwas P. M. *Inelastic* J/ψ *photoproduction.* Phys. Lett. B348 (1995) 657.

[41] M. Krämer. *QCD corrections to inelastic* J/ψ *photoproduction.* Nucl. Phys. B459 (1996) 3.

[42] A. Donnachie and P. V. Landshoff. *Exclusive vector meson production at HERA.* Phys. Lett. B348 (1995) 213–218.

[43] P. V. Landshoff. *The two pomerons.* Proceedings of the Summer School on Hadronic Aspects of Collider Physics, Locher, M. P. (Editor) Zuoz, Switzerland. hep-ph-9410250 (1994).

[44] M. G. Ryskin. *Diffractive* J/ψ *production as a probe of the gluon density.* Z. Phys. C76 (1997) 231–239.

[45] M. Glük, E. Reya, and A. Vogt. *Dynamical parton distributions of the proton and small x physics.* Z. Phys. C67 (1995) 433–448.

[46] A.D. Martin, R.G. Roberts, and W.J. Stirling. *Pinning down the glue in the proton.* Phys. Lett. B354 (1995) 155–162.

[47] HERMES Collaboration. *Technical design report*, 1993. DESY 93-015.

[48] M. Düren and K. Rith. *Polarized electron-nucleon scattering at HERA: the HERMES experiment.* In *Proceedings of the Workshop: Physics at HERA. Vol. 1*, Hamburg, 1991.

[49] H1 Collaboration. *The H1 detector at HERA*, 1996. DESY H1-96-01.

[50] Richard C. Fernow. *Introduction to Experimental Particle Physics.* Cambridge, 1986.

[51] H1 Collaboration. *Technical proposal to upgrade the backward scattering region of the H1 detector*, 1993. PRC 93/02.

[52] H1 Collaboration. *The H1 liquid argon calorimeter system.* Nuclear Instruments and Methods A336 (1993) 460–498.

[53] H1 Calorimeter Group. *Beam tests and calibration of the H1 liquid argon calorimeter with electrons.* Nuclear Instruments and Methods A350 (1994) 57–72.

[54] H1 Calorimeter Group. *Results from pion calibration runs for the H1 liquid argon calorimeter and comparisons with simulations.* Nuclear Instruments and Methods A336 (1993) 499–509.

[55] H1 Spacal Group. *Performance of the hadronic and electromagnetic lead/scintillating-fibre calorimeter for the H1 detector*, 1995. DESY 95-165.

[56] H1 Spacal Group. *Hadronic response and e/π separation with the H1 lead/fibre calorimeter*, 1995. DESY 95-250.

[57] H. Cronstrom et al. *The forward muon spectrometer.* Nuclear Instruments and Methods A340 (1994) 304–308.

[58] H1 Collaboration. *Luminosity measurement in the H1 experiment at HERA.* In *International Conference on High Energy Physics*, Warsaw, 1996.

[59] F. Sefkow et al. *Experience with the first level trigger of H1*, 1994. H1- 11/94-407.

[60] U. Almaldi (Editor). *Detection and study of the charged current event.* In *Proceedings of the Study of an ep Facility for Europe*, pages 391–394, Hamburg, 1979.

[61] Benno List. *Diploma thesis: Diffraktive J/ψ -Produktion in Elektron-Proton-Stroessen am Speicherring HERA*, 1993.

[62] Guido Schmidt. *Doctoral thesis: Untersuchung der Diffractiven Photoproduktion von J/ψ -mesonen im H1-Detekor bei DESY*, 1996.

[63] Ed. W. Buchmüller and G. Ingelman. *Lpair - a generator for lepton pair production.* In *Physics for HERA*, volume 3, pages 1478–1482, Hamburg, 1991.

[64] Paul Newman. *Doctoral thesis: A study of the dynamics of diffractive photoproduction at HERA*, 1996.

[65] Victoria Louise Hudgson. *Doctoral thesis: Measurement of the cross section for the quasi-elastic photoproduction of $\psi'(2s)$ at HERA*, 1997.

[66] N.Gogitidze and S.Levonian. *An offline luminosity determination for the 1995 e^+p data.*, 1996. H1- 02/96-471.

[67] Budnev V.M. et al. *The two photon particle production mechanism. Physical problems. Applications. Equivalent photon approximation.* Phys. Rep. C15 (1974) 181–282.

[68] C. Weizsäcker. Z. Phys. 88 (1934) 612.

[69] E. Williams. *Nature of the high energy particles of penetrating radiation and status of ionisation and radiation formulae.* Phys. Rev. 45 (1934) 729.

[70] H1 Collaboration. *Elastic production of J/ψ mesons in photoproduction and at high Q^2 at HERA.* In *HEP97*, Jerusalem, 1991.

[71] E401 Collaboration. Binkley et al. *J/ψ production from 60-300 GeV/c.* Phys. Rev. Lett. 48/2 (1982) 73–76.

[72] FTPS Collaboration. Denby, B.H. et al. *Inelastic and elastic production of J/ψ (3097).* Phys. Rev. Lett. 52/10 (1984) 795–798.

[73] E687 Collaboration. Frabetti, P.L. et al. *A measurement of the elastic J/ψ photoproduction cross section at Fermilab E687.* Phys. Lett. B316 (1993) 197–206.

[74] Zeus Collaboration. *Measurement of elastic J/ψ production at HERA.* Z. Phys. C75 (1997) 215–228.

[75] Zeus Collaboration. *Measurement of elastic ρ^0 photoproduction at HERA.* Z. Phys. C69 (1995) 39–54.

[76] H1 Collaboration. *Elastic photoproduction of ρ mesons at HERA.* Nucl. Phys. B463 (1996) 3.

[77] Zeus Collaboration. *Measurement of elastic ω photoproduction at HERA.* Z. Phys. C73 (1996) 73–84.

[78] Zeus Collaboration. *Measurement of elastic ϕ-photoproduction at HERA.* Phys. Lett. B377 (1996) 259–272.

[79] H1 Collaboration. *Elastic electroproduction of ρ and J/ψ mesons at large Q^2 at HERA.* Nucl. Phys. B468 (1996) 3.

[80] Zeus Collaboration. *Exclusive ρ^0 production in deep-inelastic electron-proton scattering a HERA.* Phys. Lett. B356 (1995) 601.

[81] B. Humbert and A.C.D. Wright. Phys. Lett. D15 (1977) 2503.

[82] Schilling et al. Nucl. Phys. B15 (1970) 381.

Acknowledgments

It is a generally known fact in the world of H.E.P. that six months of writing a thesis leaves you with the intellectual and emotional capacity of a turnip. With the remaining ten minutes of brain activity before I sink into oblivion I would like to thank the poor people who have borne the brunt of my frustration and ignorance over the past three years.

First off I would like to thank the staff of the Manchester H.E.P. group. In particular, credit is due to Mike Ibbottson and John Allison for their periods of supervision over the past three years; Fred Loebinger for always being kind and reassuring and John Banks, Andy M^{c}Nab and Stuart Wild for their maintainance of the computers. Continuing the academic theme, I would like to go some way towards expressing my gratitude to Chris Hilton in Hamburg, who is without doubt exceptionally clever and who has always been a willing font of advice and information. Most importantly, however, he has invested time and patience in me despite there being none of the reflected glory so sought after by others at DESY. I would also like to thank the other members of the UK J/ψ team: Lee West, Kirstee Hewitt and Paul Sutton. Ben Waugh also deserves a special mention for his helpful computing tips, though he'll probably feel a little foolish when I tell him that my terminal was just an empty box with a bad tempered alien inside. Thankyou also for reading this thesis through so thoroughly for me. Lastly, Tim Nicholls saved me several years of learning about postscript files by giving me use of figure 3.4.

Also instrumental in the production of this thesis are the people who shared my periods of self-doubt along the way, which can not have been an easy task! In this category of people I include my family which is both warm and wise and which I appreciate far beyond the ties of blood. Thanks also to Hugh Tallini who has given me support and a whole lot of good times to take my mind off things despite having to write his own thesis. He once told me that he'd never go out with a physicist, but it seems he couldn't help himself and I am very glad! I am happy too that I have Rachel Palmer as a friend; I consider her phonecalls and trips to Hamburg while I was there to be supreme acts of mercy which definitely helped me maintain a kind of perspective in the sometimes hellish world of DESY.

The best bit of DESY was of course the food, but a close second comes the Brits

abroad club who have left me with some brilliant memories. These people served as both colleagues and friends and satisfied both tasks admirably. There's the occupants of the Manchester office; Paul Bate, Brian Cox, Chris Hilton and Ben Waugh, who were suitably irreverent about physics and DESY politics to make me feel quite at home. Despite the traditions of animosity between the two institutions I would also like to thank Stuart Cox, Mike M^{c}Andrew, Dave Milstead and Mark Smith for their "support" in the form of Vodka. Thanks also to Julian Phillips for his riveting discussions about mother-boards and Andy Mehta and his gang at Bleichstrasse for lots of brilliant parties. Over in the wooden hut thanks to Lee West and Paul Sutton for their respective gossipy and drunken contributions to my social life. Finally, a special mention goes to the DESY women - Jane Bromley, Kirstee Hewitt, Vicki Hudgson, Sarah Nicholls and Rachel West - for some great evenings eating, drinking and chatting - a tradition someone should keep up!

A great story to tell my grandchildren, but a nightmare at the time was the balcony saga. I would like to thank Susan Ketels for believing that we weren't the 'hooligans' described by the rapacious Herr and Frau Offen. She dealt with the situation with great diplomacy, however I still consider that it would have been better to roll the comatosed Dr. (!) Paul Sutton off the edge and claim damages!

Coming back to Manchester after two years away was a little scarey, however Lee Curtis, David Eatough, Nick Malden, Nick Savaas, Beth Vorkurka, Andy Walkden and Jim Wetherall have helped to make the physics department a tad more enticing. More importantly though, I have been extremely fortunate to end up living with the most stylish and popular crowd in Chorlton. Not only have they provided me with a much needed social life but have welcomed me to their bosom and showed me that there is life after being a student! So thanks to Louise Fretwell, Richard Gardner, Beverly Kitchen, Dave Purcell, Dave Ring and Robert Shields.

With all the thank-yous out of the way I can now turn to the future...but first I am going home to sleep for a long time! **May 1998**